

Electronic Theses and Dissertations, 2004-2019

2009

Gabor Domain Optical Coherence Microscopy

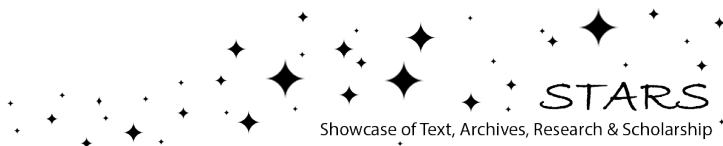
Supraja Murali
University of Central Florida

 Part of the [Electromagnetics and Photonics Commons](#), and the [Optics Commons](#)
Find similar works at: <https://stars.library.ucf.edu/etd>
University of Central Florida Libraries <http://library.ucf.edu>

This Doctoral Dissertation (Open Access) is brought to you for free and open access by STARS. It has been accepted for inclusion in Electronic Theses and Dissertations, 2004-2019 by an authorized administrator of STARS. For more information, please contact STARS@ucf.edu.

STARS Citation

Murali, Supraja, "Gabor Domain Optical Coherence Microscopy" (2009). *Electronic Theses and Dissertations, 2004-2019*. 3976.
<https://stars.library.ucf.edu/etd/3976>



GABOR DOMAIN OPTICAL COHERENCE MICROSCOPY

by

SUPRAJA MURALI

B.E. (Honors) Birla Institute of Technology and Science, 2003

M.S. University of Central Florida, 2005

A dissertation submitted in partial fulfillment of the requirements
for the degree of Doctor of Philosophy
in CREOL, the College of Optics and Photonics
at the University of Central Florida
Orlando, Florida

Summer Term

2009

Major Professor: Jannick P. Rolland

©2009 Supraja Murali

ABSTRACT

Time domain Optical Coherence Tomography (TD-OCT), first reported in 1991, makes use of the low temporal coherence properties of a NIR broadband laser to create depth sectioning of up to 2mm under the surface using optical interferometry and point to point scanning. Prior and ongoing work in OCT in the research community has concentrated on improving axial resolution through the development of broadband sources and speed of image acquisition through new techniques such as Spectral domain OCT (SD-OCT). In SD-OCT, an entire depth scan is acquired at once with a low numerical aperture (NA) objective lens focused at a fixed point within the sample. In this imaging geometry, a longer depth of focus is achieved at the expense of lateral resolution, which is typically limited to 10 to 20 μm . Optical Coherence Microscopy (OCM), introduced in 1994, combined the advantages of high axial resolution obtained in OCT with high lateral resolution obtained by increasing the NA of the microscope placed in the sample arm. However, OCM presented trade-offs caused by the inverse quadratic relationship between the NA and the DOF of the optics used.

For applications requiring high lateral resolution, such as cancer diagnostics, several solutions have been proposed including the periodic manual re-focusing of the objective lens in the time domain as well as the spectral domain C-mode configuration in order to overcome the loss in lateral resolution outside the DOF. In this research, we report for the first time, high speed, sub-cellular imaging (lateral resolution of 2 μm) in OCM using a Gabor domain image processing algorithm with a custom designed and fabricated dynamic focus microscope interfaced to a Ti:Sa femtosecond laser centered at 800 nm within an SD-OCM configuration. It is envisioned that this

technology will provide a non-invasive replacement for the current practice of multiple biopsies for skin cancer diagnosis.

The research reported here presents three important advances to this technology all of which have been demonstrated in full functional hardware conceived and built during the course of this research. First, it has been demonstrated that the coherence gate created by the femtosecond laser can be coupled into a scanning optical microscope using optical design methods to include liquid lens technology that enables scanning below the surface of skin with no moving parts and at high resolution throughout a $2\times 2\times 2$ mm imaging cube. Second, the integration the variable-focus liquid lens technology within a fixed-optics microscope custom optical design helped increase the working NA by an order of magnitude over the limitation imposed by the liquid lens alone. Thus, this design has enabled homogenous axial and lateral resolution at the micron-level (i.e., $2\ \mu\text{m}$) while imaging in the spectral domain, and still maintaining *in vivo* speeds. The latest images in biological specimens clearly demonstrate sub-cellular resolution in all dimensions throughout the imaging volume. Third, this new modality for data collection has been integrated with an automated Gabor domain image registration and fusion algorithm to provide full resolution images across the data cube in real-time. We refer to this overall OCM method as Gabor domain OCM (GD-OCM).

These advantages place GD-OCM in a unique position with respect to the diagnosis of cancer, because when fully developed, it promises to enable fast and accurate screening for early symptoms that could lead to prevention. The next step for this technology is to apply it directly, in a clinical environment. This step is underway and is expected to be reported by the next generation of researchers within this group.

ACKNOWLEDGEMENTS

I would first of all like to thank my advisor, Dr. Jannick P. Rolland who has been a good teacher and a guide and who was the person that encouraged me to do the PhD. This work would have been impossible without her guidance and ability to circumvent challenges, which are very often encountered in research, with her innovative thinking skills.

I would also like to take this opportunity to thank Dr. Shin-Tson Wu and Dr. James Harvey for serving on my committee and for always being ready to help right from when I did my Masters degree. I would specially like to express my gratitude to Dr. Kevin Thompson for the stimulating discussions and help during the design process. My thanks also go to Dr. Miguel A. Alonso for discussion about some of the mathematical derivations for FD-OCM.

I would like to gratefully acknowledge the Florida Photonics Center for Excellence (FPCE), the US Army Medical and Material Command, and the I2lab Foundation at the University of Central Florida for funding this research. I would like to express my thanks and appreciation to General Optics (Asia) Ltd. for their easy accessibility, excellent fabrication support, and prompt delivery of our research prototype. I would also like to acknowledge Optical Research Associates for the courtesy student license of CODEV™.

You don't get to choose the people you work with and I have been fortunate enough to have had a wonderful set of colleagues at ODAlab. I would like to thank every one of them for making work a pleasant place to come to. I would specially like to acknowledge my OCT team members – Kye-Sung Lee and Panomsak Meemon – who have always been there to lend a hand, sometimes literally, as hand models for all my imaging experiments! I would also like to thank

Ilhan Kaya for his help with the 3D image rendering. I must also mention the terrific support staff at CREOL who efficiently took care of the administrative procedures, travel, purchasing etc. helping me focus on my research.

It has been 6 years of great memories and every stage towards completing my PhD would be impossible without my large network of friends throughout the US. They've been there during my ups and downs and have been an invaluable support group. I would like to especially mention all my friends in Orlando who've made my stay here feel like home – Thank You. My thanks to all my friends in US and India for the good times we've shared. Specially, I would like to thank my girlfriends Shruthi and Pallavi, and also Aravindhnan, who have known me for over 10 years and always been there for me. Most importantly, I would like to sincerely thank one of my best friends, Pradeep who has been there as a constant source of support every step of the way. Our refreshing and thought-provoking conversations and discussions about any subject, be it science or otherwise, have made the last 6 years a very memorable ride.

I never felt far away from home because of my wonderful extended family in the US – I would like to acknowledge my cousins and sisters-in-law, Ramkumar, Vidya, Revathy, Karthik, Sivakumar and Subha. Right from cooking tips to my first credit card, they've helped me settle down in this country and were my home away from home during my PhD. Lastly, I would like to thank my parents Murali and Lakshmi and my sister Divya who are my source of motivation, and encouragement in everything I do. They provide a strong backbone and are always behind my every successful project.

TABLE OF CONTENTS

LIST OF FIGURES	ix
LIST OF TABLES	xii
CHAPTER 1- INTRODUCTION.....	1
1.1 Types of Skin Cancer.....	2
1.2 Skin Cancer Morphology.....	6
1.3 Current Non-invasive Clinical Skin Imaging Techniques	14
1.4 Optical Coherence Tomography and Skin Imaging.....	24
CHAPTER 2- OPTICAL COHERENCE MICROSCOPY	26
2.1 Time-Domain Principle of OCM	26
2.2 Spectral Domain Optical Coherence Tomography	33
2.2.1 Fourier domain OCT (FD-OCT)	34
2.2.2 Swept source OCT (SS-OCT)	39
2.3 Dynamic Focusing – Related Work	40
2.4 Motivation.....	45
2.5 Research Summary	46
2.6 Dissertation Outline	48
CHAPTER 3- GABOR DOMAIN OCM IMAGING.....	50
3.1 Gabor Domain Optical Coherence Microscopy.....	50
3.1.1 Mathematical framework of GD-OCM	52
3.1.2 GD-OCM imaging.....	55
3.2 Optical Design of a Dynamic Focusing Probe for GD-OCM.....	58
3.2.1 Aberration analysis of a plane parallel plate	59
3.2.2 Liquid crystal lens based microscope objective	70
3.2.3 Liquid lens based microscope objective.....	76
CHAPTER 4- DESIGN TOLERANCING, FABRICATION AND TESTING.....	93
4.1 Optical Tolerancing	93
4.2 Fabrication and Calibration.....	97
4.3 Testing and Experimental Analysis	101
4.3.1 Experimental set-up.....	102
4.3.2 Measurement of lateral resolution in air.....	103
4.3.3 Depth of focus assessment in air	106
4.3.4 Evaluation of resolution and depth of focus in scattering media	107
4.4 Biological Tissue Imaging Results	109
4.4.1 2D imaging using the dynamic focusing microscope.....	110
4.4.2 3D imaging using the dynamic focusing microscope.....	114

CHAPTER 5- SUMMARY AND CONCLUSIONS.....	117
REFERENCES	122

LIST OF FIGURES

Figure 1.1: Skin structure: (a) Illustration, (b) Stained histology image.....	3
Figure 2.1: TD-OCT interferometer schematic.....	27
Figure 2.2: Trade-off parameters in OCM.....	30
Figure 2.3: Diagram illustrating depth encoding in the interference signal detected in SD-OCT	34
Figure 2.4: Schematic for Fourier domain OCT	35
Figure 2.5: FD-OCM layout used in this research	38
Figure 2.6: Mirror image property in (a) the axial intensity signal profile (b) 2D B-scan of an onion	39
Figure 2.7: Schematic for Swept Source OCT.....	40
Figure 2.8: Different schemes that incorporate dynamic focusing (a) Schmitt <i>et al.</i> 1997, (b) Drexler <i>et al.</i> 1999, (c) Qi <i>et al.</i> 2004, (d) Divetia <i>et al.</i> 2005, (e) Wiesauer <i>et al.</i> 2005, and (f) Michelson Diagnostics 2008.....	41
Figure 3.1: Scanning schemes: (a) Conventional OCT scan; (b) GD-OCM scanning	51
Figure 3.2: (a) Simulated spectra acquired; (b) Its Fourier transform obtained in classical FD-OCM (c) Illustration of the spectral interferogram convolved with a Gabor function, enabling (d) A zone of the reconstructed image to be extracted. The final image sums all automatically registered zones to create a depth focused fused image.	54
Figure 3.3: GD-OCM experimental layout with dynamic focusing in the sample arm	55
Figure 3.4: Automatic fusing algorithm for GD-OCM.....	57
Figure 3.5: Power spectral density for system performance analysis	58
Figure 3.6: Seidel aberrations incurred from a plane parallel plate in the path of a converging beam.....	60
Figure 3.7: RMS Wavefront error at the exit pupil in waves at 1 μm computed in theory from the Seidel values as a function of NA with increasing thickness of the plane parallel plate	62
Figure 3.8: Wave aberrations in waves RMS at 1 μm as a function of NA with increasing thickness of the plane parallel plate. Data were computed at the paraxial focus using a marginal ray angle corresponding to the maximum FOV.	63
Figure 3.9: Strehl ratio vs. NA with increasing thickness of the plane parallel plate.	65
Figure 3.10: PSF and Strehl ratio generated in CODEVTM at various NA (increasing from top to bottom) and thicknesses (increasing from left to right).....	66
Figure 3.11: Preliminary design MTF at 100 cycles/mm corresponding to 5 μm resolution.	71
Figure 3.12: Working of a gradient index lens	72
Figure 3.13: Liquid crystal based microscope objective – lens layout when focused at the surface of the sample (0 mm depth)	75
Figure 3.14: MTF of the liquid crystal based dynamic focusing microscope objective obtained at (a) 0 mm focus; (b) 1 mm focus; (c) 2 mm focus.....	75

Figure 3.15: Electro-wetting based liquid lens. (a) Focus mechanism; (b) Power of the liquid lens as a function of the voltage applied:	77
Figure 3.16: (a) Lister microscope 0.65NA with (b) MTF > 20% at 450lp/mm ; (c) NA 0.25 NIR Lister with (d) MTF >20% at 250 lp/mm.....	79
Figure 3.17: Final design of liquid lens based dynamic focusing immersion microscope. (a) Optical layout; (b) Image plane position vs. voltage applied; (c) Change in liquid lens curvature across three focal positions through the working depth range.....	82
Figure 3.18: Optical layout and third and fifth order aberration contribution (units in waves @ 809 nm) for each surface of the dynamic focusing microscope with focus location fixed at the center (i.e.1 mm depth) of the sample	85
Figure 3.19: Third and fifth order aberrations of the dynamic focus microscope (units in waves @ 809 nm) at focal depths of (a) 0 mm, (b) 1 mm and (c) 2 mm inside the sample	86
Figure 3.20: Field curves of the dynamic focus microscope at focal positions of (a) 0 mm; (b) 1 mm; (c) 2 mm inside a medium of refractive approaching that of skin	87
Figure 3.21: (Left) MTF curves and (Right) PSF on-axis are shown at the three focal positions namely 0 mm, 1 mm and 2 mm inside a medium of refractive approaching that of skin.....	89
Figure 3.22: (Contd. next page) Ray aberration curves across the FOV at the focus depths of (a) 0 mm; (b) 1 mm; (c) 2 mm inside a medium of refractive approaching that of skin	90
Figure 4.1: Optical design layout and doublet naming convention in the tables that follow.....	96
Figure 4.2: Mechanical design layout – top view and section view.	98
Figure 4.3: Wavefront aberration map of the fabricated optics on axis with and without the liquid lens included in the system tested in a Zygo interferometer at 632.8 nm –Performance demonstrates diffraction limit given that RMS wavefront error < 0.07 waves.....	100
Figure 4.4: (a) Experimental set-up: PC – Polarization controller; Col – Collimator, DC – Dispersion compensator; M- Mirror, DF-OCM –Dynamic focus OCM and (b-c) MTF calculation method.	102
Figure 4.5: MTF curves measured at 2 mm, 1 mm and 0.1 mm focus positions in a (a) horizontal configuration; (b) vertical configuration.....	105
Figure 4.6: MTF measured at the center of the focus range, i.e.1 mm focal depth in air: (a) Contrast % obtained at various points of defocus (b) MTF measured at $\pm 30 \mu\text{m}$ defocus still maintains over 20% contrast at 250 lp/mm corresponding to 2 μm resolution.....	106
Figure 4.7: MTF curves measured at 0.1 mm, 1 mm focus positions with the dynamic focusing OCM microscope placed in a vertical configuration	108
Figure 4.8: MTF curves measured at 0.1 mm, 1 mm focus positions with the dynamic focusing OCM microscope in a vertical configuration.....	109
Figure 4.9: Cross-sectional image of <i>Xenopus Laevis</i> acquired (a) with fixed focus at 400 μm below the sample surface; (b) with dynamic focusing every 100 μm for 10 zones; (c) with fixed focus at 350 μm below the sample surface; (d) with dynamic focusing every 100 μm for 5 zones	110
Figure 4.10: Cross-sectional image of <i>Xenopus Laevis</i> acquired (a) with fixed focus at 400 μm below the sample surface; (b) with dynamic focusing every 100 μm for 10 zones	112

Figure 4.11: <i>In vivo</i> depth cross-sections with a 2 mm lateral extent, imaged in 8 zones in the region of (a) the finger nail fold and (b) the finger tip of the palm. Images acquired along the red line shown on the right.....	113
Figure 4.12: <i>Ex vivo</i> skin depth cross-section with a 2 mm lateral extent, imaged in 5 zones in the region of the finger joint. Image acquired along the red line shown on the left.	114
Figure 4.13: Perspective views of a 400 μm^3 image volume acquired <i>ex vivo</i> in an African frog tadpole with 2 mm lateral extent and 2 depth zones in preliminary tests.	115
Figure. 4.14: Scanning mechanism for a 500 μm^3 image volume in GD-OCM.	116

LIST OF TABLES

Table 1: Skin anatomy- epidermal and dermal layers.....	5
Table 2 : Glossary of terms used in literature to describe cellular attribute of melanoma (Reproduced from Scope <i>et. al</i> , 2007)	7
Table 3 (Contd. next page): Classification of <i>in vivo</i> melanoma diagnostic techniques based on resolution	11
Table 4: Introduction and state-of-the-art for predominant OCT/OCM technologies	32
Table 5: The Seidel coefficients and wave aberration coefficient conversions for the primary third order aberrations induced by a plane parallel plate.	61
Table 6: Comparison of spherical aberration on-axis computed from theory and software. In CODEV™ an analysis of the fringe Zernike polynomials was used to compute the zero to peak W_{040}	64
Table 7: Strehl ratio, wavefront error (both P-V and RMS in waves at 1 μm), and the PSF FWHM and FW at $1/e^2$ of maximum intensity simulated in CODEV™ on-axis for different NA and plate thickness.....	69
Table 8: First order parameters of the liquid crystal lens based microscope when focused at 0 mm, 1 mm and 2 mm from the surface of the sample (all units in mm)	74
Table 9: Microscope design specifications	81
Table 10: First order parameters of the liquid lens based microscope (all units are in mm)	83
Table 11: RMS wavefront error and Strehl ratio at the composite best focus image plane located at $-0.46 \mu\text{m}$ from the paraxial image plane.	88
Table 12: Fabrication tolerances and cost category for General Optics (Asia) Ltd.	94
Table 13: Performance summary after tolerance analysis	96
Table 14: Fabrication data and initial design specified tolerances	96
Table 15: Final assigned shop tolerances for prototype fabrication.....	97
Table 16: Surface by surface errors of each doublet measured after fabrication	101
Table 17: Summary of criteria for DOF.....	107

CHAPTER 1- INTRODUCTION

Cancer is a major public health problem in the United States and other developed countries. According to the American Cancer Society (ACS), currently one in four deaths in the United States is due to cancer (Jemal 2008). One in five Americans will get skin cancer in the course of a lifetime. More than one million cases of basal and squamous cell carcinoma are diagnosed in this country each year. The deadliest form of skin cancer, melanoma, was diagnosed in 58,940 Americans in 2007. An estimated 10,850 deaths occurred in 2007 (8110 from melanoma and 2740 from non-melanoma). By 2010, melanoma is projected to rise to one in fifty Americans. It is estimated that more than 85% of all cancers originate in the epithelium (Gurjar 2001), the topmost layer of skin. Most non-melanoma cancer cases can be cured if detected in their early stages. Melanoma spreads more rapidly to different areas of the body; however it is still curable if detected in its earliest stages. Cancer in general is the leading cause of deaths worldwide with 7.6 million deaths reported by the World Health Organization (WHO) in 2004. Statistics from WHO show that 70% of the cancer cases have occurred in low and middle income countries, and the toll is projected to rise by 50% by 2030. Smoking, alcohol use, obesity, urban air pollution and UV content are some of the major risk factors for cancer, and more than 30% of the cases can be prevented by avoiding these risk factors (Danaei 2005). Early detection of cancerous cells in the skin helps reduce the cost of health care within the US and worldwide.

Excisional biopsy is the proven standard method for cancer detection. However, many biopsies are done on a hit or miss basis because only small pieces of tissue are excised at random and dissected to check for cancerous cells. In addition they can be subjective and lead to discordance

among dermatologists as to the diagnosis of a neoplasm (Lodha 2008). Moreover, excisional biopsy imposes problems like the risk of cancer cell spreading, infection, and hemorrhage. A non-invasive procedure will increase patient compliance for screening for skin lesions since it eliminates the need for numerous evaluations and painful biopsies, thus allowing diagnosis of skin cancer in its early stages when there are better chances of battling the disease. There has been a long history of extensive research in the quest for a low-cost, non-invasive, reliable skin imaging modality. In the following sections, we will summarize the properties of skin and point out the distinct differences between normal and cancerous skin cells. This will be followed by a brief introduction to the most relevant technologies and instrumentation, optical or otherwise, currently in use or under investigation for non-invasive skin imaging, and their advantages and drawbacks are presented.

1.1 Types of Skin Cancer

Skin is a highly complex, inhomogeneous, and highly scattering tissue. In a majority of cases, skin cancer occurs in skin that has been exposed to sunlight, such as the skin on the face, neck, hands, and arms. Skin cancer can be found and treated effectively when several of its early symptoms are correctly diagnosed. Some of them include the change in appearance or size or color of a mole or spot, a new growth, scaliness, bleeding, spread of pigmentation beyond its border, itchiness, pain, change in sensation etc. It is generally believed that most cancers are monoclonal in origin (Kumar 2005) i.e., they arise from a single cell that can give rise to a focus of neoplastic or abnormal cells that are considered pre-cancer. These cells are confined to the epithelium and are pre-cursors to malignant cancer, and could either grow radially into the tissue

and invade other organs of the body or naturally regress (benign), the latter being largely the case.

Skin cancer develops in the two top layers of the skin, namely the epidermis and dermis (see Fig.1.1). The epidermis is the topmost layer of the skin. It is mostly made of flat cells called squamous cells. The deeper part of the epidermis consists of round cells called basal cells. Pigmentation cells called melanocytes are located in the lowest part of the epidermis. The epidermis consists of several sub-layers as shown in Table 1, and constitutes an overall thickness of approximately 75 μm . The dermis is the second layer of the skin located under the epidermis. It contains blood vessels, lymph vessels, and glands (e.g. sweat glands, sebaceous glands etc.).

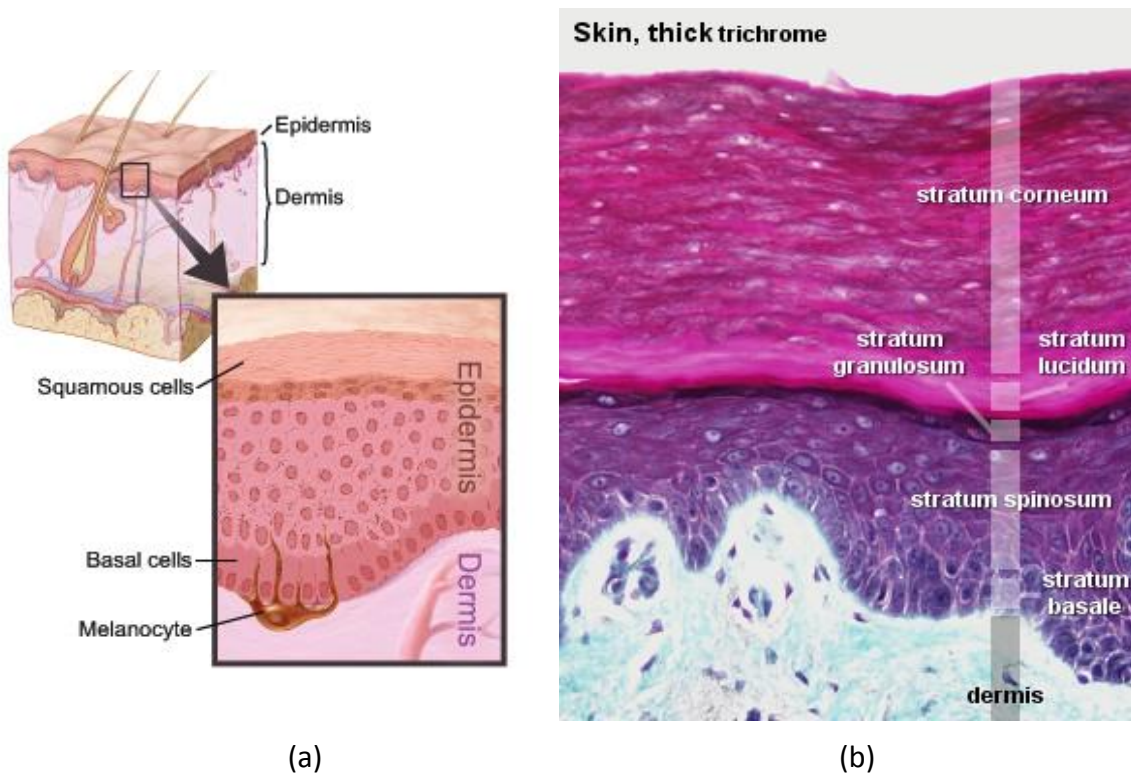


Figure 1.1: Skin structure: (a) Illustration, (b) Stained histology image

The dermis is composed of two major sub-layers (also shown in Table 1) and constitutes an overall thickness of 1-4 mm, depending on the location on the body. For example, the stratum corneum, epidermal and dermal thickness are of minimum thickness near the eye region, facial and genital areas, comparatively thicker in the extremities such as the back, legs and shoulder areas, and thickest in the palm of the hand and sole of the foot (Hoffmann 1994; Olsen 1995; Gniadecka 1998; Ya-Xian 1999; Nouveau-Richard 2004; Sandby-moller 2004). The thickness also varies with gender, age, and skin type, however, the difference of skin thickness between individuals is not significant when compared with the difference between body sites (Lasagni 1995; Sandby-moller 2004).

85% of all cancers originate in the epidermis (Gurjar 2001). Skin cancer, specifically, also originates in the epidermal layers and is classified into three types based on the specific sub-layer cells that it grows from. Basal cell carcinoma (BCC) starts in the basal cell layer of the epidermis (small, round cells in the base of epithelium) usually in the form of small, shiny bumps or nodules mainly on sun-exposed areas of the skin such as the face, head, neck, arms and hands. BCC, also referred to as non-melanoma skin cancer, accounts for 80% of all skin cancers (Gallagher 1990; Marks 1995). According to the American Association of Dermatology (AAD) (McGovern 2008), 95% of BCC cases are cured when treated. While BCC itself grows slowly and causes only local damage to varying degrees, rarely spreading to other areas of the body it still places patients at high risk for developing other cancers. Squamous cell carcinoma, also referred to as non-melanoma skin cancer, is the second most common type of skin cancer among Caucasians affecting about 200,000 people per year. It develops from the squamous cell layer (flat cells that form the surface of the skin) of the epidermis. Although more destructive than BCC, according to the AAD, the cure rate is 95% when properly diagnosed and treated.

Table 1: Skin anatomy- epidermal and dermal layers

Layer	Sublayer	Thickness	Cells	Cell Size	Notes
Epidermis		~75 μm^6			
	Stratum Corneum	8-14 μm^7	Corneocytes ⁵ (flattened) ³	Varies ⁵	Dead, No nucleus, organelles ¹
	Stratum Lucidum	Not found in thin skin	Keratinocytes ³ (flattened)	~1-2 μm^3	Dead, Contains eleidin, precursor to keratin; thick skin only ²
	Stratum Granulosum	6-15 μm^7	Squamous Cells	25-35 μm^7	Alive, larger nuclei than spinous ⁷
	Stratum Spinosum	~40-50 μm^*	Keratinocytes	15-25 μm^7	Alive, Dark nuclei ² , smaller nuclei than granular cells ⁷
	Stratum Basale	7-12 μm^{7**}	Keratinocytes	7-12 μm^7	Alive
			Melaninocytes	~7 μm^2	Alive
Dermis		1-4 mm^4			
	Papillary Dermis	~1.5 mm^4	many types		Made of loose areolar connective tissue ²
	Reticular Dermis	~1.75 mm^4	many types		Adipose tissue, oil and sweat glands ²
* No measurement was found, approximated by subtracting other layer measurements from total thickness.					
** The stratum basale is only one cell layer thick (7), so its cell size is its layer thickness.					
(Elias 2008) ¹ , (Alcamo 2004) ² , (Junqueira 2005) ³ , (McCance 2006) ⁴ , (Wilhelm 1997) ⁵ , (Gambichler 2006) ⁶ , (Huzaira 2001) ⁷ .					

Melanoma, the least common and the most virulent of skin cancers, develops from the melanocytes or the pigment cells in the lowermost region of the epidermis and is responsible for 75% of the deaths (Jemal 2008) caused by skin cancer. This tumor is malignant, non-local and spreads quickly through the lymph or vascular system by metastasizing different sites on the body. Melanoma is best treated when diagnosed early.

1.2 Skin Cancer Morphology

A *neoplasm* or tumor is defined as “an abnormal mass of tissue, the growth of which exceeds and is uncoordinated with that of the normal tissue and persists in the same excessive manner after the cessation of the stimuli that evoked the change”(Willis 1952). A fundamental trait of all neoplasms is the termination of responsiveness to normal growth controls. The tumor progression for malignant melanoma is a multistep process that leads to 6 fundamental changes in cell-inhibitory signals (Hanahan 2000), 1. Self-sufficiency in growth signals, 2. Insensitivity to growth-inhibitory signals, 3. Evasion of *apoptosis* (programmed cell death) (Evan 2001), 4. Limitless replicative potential, 5. Sustained *angiogenesis* (i.e., blood vessel formation) (Carmeliet 2000), 6. Ability to invade and metastasize (i.e., spreading) (Poste 1980; Steeg 2006). This property of metastases and invasiveness is the clearest indicator for a malignant neoplasm. One of the most characteristic abnormalities of malignancy is *anaplasia* or lack of differentiation. Anaplastic cells are rapidly growing and show marked *pleomorphism* i.e., variation in size and shape. Their nuclei have abnormal morphology, i.e., they are extremely hyperchromatic (dark staining) and are large, bizarre, and inconsistent in size and shape. Such loss in uniformity of individual cells leads to a loss in both architectural orientation and specialized functional activity (Kumar 2005). In addition to these cytological abnormalities, the orientation of the anaplastic

cells becomes more randomly organized having random orientations. This knowledge of anatomy allows us to infer that imaging technology developed will need to ultimately need to resolve cell structure and/or probe information about the organization of the cells using methods such as polarization-sensitive imaging (Strasswimmer 2004). Table 2 summarizes some of the most typical cellular attributes of melanoma widely used for characterizing non-invasive diagnosis in research literature (Scope 2007).

Table 2 : Glossary of terms used in literature to describe cellular attribute of melanoma (Reproduced from Scope *et. al*, 2007)

<p>Cellular atypia</p>	<p>Presence of cells whose appearance (nuclei, cytoplasm, or both) is different from the patient’s normal counterparts. This word does not specify whether these abnormalities are inflammatory, reactive, or neoplastic.</p> <p>Cellular atypia can be graded as:</p> <p>Mild—there are cells in which nuclei or cytoplasm or both are mildly different from their normal counterparts.</p> <p>Marked—there are cells in which nuclei or cytoplasm or both are very different from their normal counterparts. Marked atypia is considered when cells are large (50 µm), display unusual contour (eg, triangular, star-shaped) or have large and eccentric nuclei.</p> <p>The observer should comment on the density of atypical cells. We currently recommend use of the terms “sporadic” (few atypical cells) or “numerous” (many atypical cells).</p>
<p>Cellular monomorphism</p>	<p>Groups of cells with similar cellular and nuclear size and shape</p>
<p>Cellular pleomorphism</p>	<p>Varying morphology (cell size, shape, refractivity) of cells in the lesion; variability can range from mild to marked.</p>
<p>Cell refractivity (synonymous with refractility/brightness).</p>	<p>Different cell types have different expected index of refraction. Cells with a higher index of refraction appear brighter on a reflective confocal microscope. In addition, refractivity may vary in the same cell type, probably due to changes in metabolic activity (eg, increased melanin production by melanocytes) and skin type.</p> <p>Cell refractivity should be noted in the following instances:</p>

	<p>High—when cells appear markedly brighter than their normal counterparts</p> <p>Low—when cells appear darker than their normal counterparts</p> <p>Heterogeneous—when cells in the image show variable brightness, some cells being brighter and others darker or equal in brightness compared to their normal counterparts.</p>
Cell shape	<p>Outer cell outline (silhouette) as visualized under a reflective confocal microscope, with no attention to internal structures.</p> <p>Terms used to describe cell shapes include round, oval, spindle (elongated cell with sharp/tapered ends), elongated (more general term if not oval or spindle), stellate (star-shaped cell due to emanating dendritic processes), and triangular.</p>
Cell size	<p>Cell size or dimension (longest diameter) can be referred to as “smaller” or “larger” compared to the patient’s normal counterparts or can be measured as an absolute number.</p> <p>The expected size for keratinocytes is:</p> <p>Corneal layer: 10-30 μm</p> <p>Granular layer: 25-35 μm</p> <p>Spinous layer: 15-25 μm</p> <p>Basal layer: 07-12 μm</p> <p>The expected size of normal melanocytes with a reflective confocal microscope has not been reported. It is estimated to be similar to that of basal keratinocytes.</p>
Dendrite	<p>Elongated branching structure extending from the cell body; they are usually present in melanocytes and Langerhans cells.</p>
Length	<p>Dendrite length may be appreciated by comparison with normal counterparts and by expected length of the dendrites in a given cell.</p>
Thickness	<p>Dendrite thickness may be appreciated by comparison with normal counterparts and by the expected thickness of the dendrites in a given cell.</p>
Dermal cells	<p>Nucleated isolated round to oval refractive cells with a dark nucleus, located in the papillary dermis, Plump-bright irregularly shaped bright cells, with ill-defined borders, and no visible nucleus, probably corresponding to melanophages.</p>



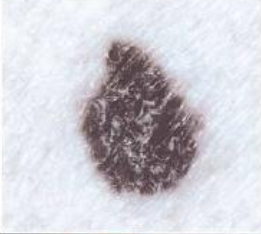


In order to describe the growth and extent of cancer, staging is generally used and the cancer stages are labeled I through IV based on tumor size, thickness, and extent of spread. The lowest number corresponds to the earliest stage (least critical) of cancer. Based on Breslow index (Breslow 1987) measurements, melanoma can be classified into four stages during its development from its early to final phases based on its depth of occurrence in the skin (Sahin 1997; McMasters 1999; Vereecken 2005). In Stage I, cancerous lesions occur at less than 1mm depth of skin tissue. During Stage II, skin cancer invades the reticular dermis and is present at depths greater than 1mm. At Stage III, the cancer invades subcutaneous tissue and spreads to local lymph nodes. Maximum spreading to remote sites involving distant metastasis occurs in Stage IV (most common in liver, lung, and brain cancer).

While several imaging schemes are used and investigated for the diagnosis of cutaneous malignant melanoma *in vitro* and *in vivo*, the numerical values of resolution and depth available are not compared with reference to their relevance to diagnosis in terms of what tangible information can be obtained and significant conclusions drawn based on the data extracted from the images from different technologies. Recently, Moncrieff *et al* have suggested a simple classification system that aims to validate different imaging methods based on their lateral resolution and probing depth, particularly with reference to their significance for the detection and diagnosis of cutaneous malignant melanoma (Moncrieff 2002). In their classification, a pigmented skin lesion has been categorized into the primary, secondary, tertiary and quaternary structures based on the level of lateral resolution required to identify them; The primary structure of the pigmented skin lesion requires the highest resolution and consists of the chromophore i.e., the melanin or haemoglobin or the melanosome as a whole, while the quaternary structure is that which is readily identified by the naked eye via its properties of symmetry, border color,

diameter and elevation or the 'ABCDE' system in short (Fitzpatrick 1988). Standard histology requires the storage, excision, fixing, sectioning, staining and visual examination of the biological tissue sample under a microscope. Such a meticulous sample preparation process can be demanding in terms of both time and labor and more importantly could cause artifacts that arise from the freezing, sectioning and processing of the sample (Zonios 1998). Therefore, there has been a drive in the last few decades to develop a non-invasive imaging system that is fast, accurate and reliable and could be used widely as a clinical screening tool in hospitals and clinics. Table 3 summarizes the parameters discussed above for several prominent non-invasive skin imaging techniques being used today (Marghoob 2003).

Table 3 (Contd. next page): Classification of *in vivo* melanoma diagnostic techniques based on resolution




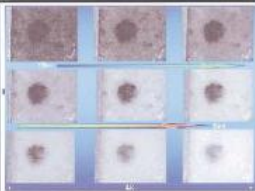
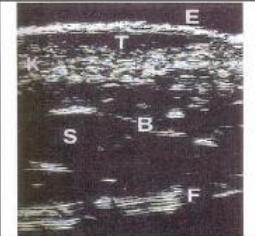

Reproduced from Marghoob *et al.* (2003)

Resolution	Imaging Device	View of Lesion	Depth of imaging (skin layer)	View of skin	Time Dimension (Possibility to monitor changes sequentially)
Quaternary: Clinical Lesion -Visible to the naked eye	Magnifying Lens		Surface	H	Yes
	Wood's Lamp		Surface	H	Yes
	Individual Lesion Photography		Surface	H	Yes
	Total Cutaneous Photography		Surface	H	Yes
Radiological lesion - Macroscopic detail only	Magnetic Resonance Imaging		Subcutaneous	V	Unknown

3(a): Quaternary resolution*

H, Horizontal; V, vertical.

*Tables 3(a), 3(b), and 3(c) are organized according to the resolvable structure of a lesion (melanoma), whereas the text is organized according to clinical utility of the imaging devices

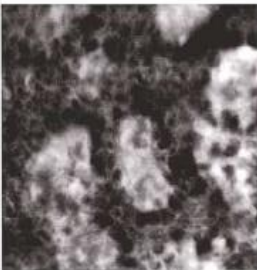

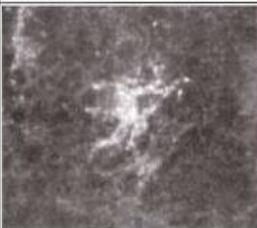
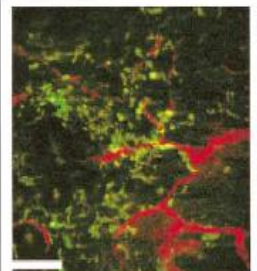
Resolution	Imaging Device	View of Lesion	Depth of imaging (skin layer)	View of skin	Time Dimension (Possibility to monitor changes sequentially)
Tertiary: Cellular aggregates - Nevo-melanocytic nests - Collagen - Blood vessels	Dermoscopy		Papillary Dermis	H	Yes
	Computer Assisted Diagnosis		Papillary Dermis	H	Unknown
	Siascope		Papillary Dermis	H	Unknown
	MelaFind		Reticular Dermis/ Subcutaneous	H	Unknown
	High frequency Ultrasound*		Epidermis (>50MHz) Reticular Dermis (<20MHz)	V	Unknown
	Optical Coherence Tomography**		Papillary dermis Reticular dermis (decreased resolution)	V	Unknown

3(b): Tertiary resolution**

H, Horizontal; V, vertical.

*Resolution of 50-100 MHz ultrasound can be classified as tertiary, with improved resolution of structures at the depth of the epidermis. Lower frequency 20 MHz ultrasound is more suitably classified under Quaternary.

**Optical coherence tomography can routinely resolve tertiary structure; however, it is reported that improved systems have the ability to resolve cellular detail (secondary).

Resolution	Imaging Device	View of Lesion	Depth of imaging (skin layer)	View of skin	Time Dimension (Possibility to monitor changes sequentially)
Secondary: Cellular resolution - Melanocytes - Keratinocytes	Fluorescence CSLM		Papillary dermis	H	Unknown
	Reflectance CSLM		Papillary dermis	H	Possible
Primary: Subcellular structures - Melanosome - Melanin - Nucleoli Indirect - Fluorescent labeling of proteins or membrane receptors	Reflectance CSLM***		Papillary dermis	H	Possible
	Fluorescence CSLM		Papillary dermis	H	Unknown

3(c): Primary and Secondary resolution***

CSLM, Confocal scanning laser microscopy.

***CSLM permits resolution at a cellular level (secondary) with a limited degree of primary resolution.

Therefore, based on the analysis of skin structure and histopathology data on skin cancer morphology, we can establish that the maximum probing depth required for the early diagnosis of Melanoma to be at approximately 1-1.5 mm maximum below the skin surface. Additionally, the resolution classification criteria in Table 3 confirm that at least tertiary resolution or better is an important requirement for effective detection of subcutaneous melanoma.

1.3 Current Non-invasive Clinical Skin Imaging Techniques

There has been a rising incidence of skin cancer in the last two decades, and the best treatment is still the early detection and excision of the primary tumor. The traditional approach to skin cancer diagnosis has emphasized histopathology examination or visible inspection of the suspected skin lesion with and without biopsy. The most common practice in such visual examination is still the ABCD rule that uses morphological features of the cancer to differentiate benign and malignant cases. However, this method provides only 65-80% sensitivity (Kopf 1975; Koh 1989) since it does not account for very small lesions (< 5 mm). There is also a high false positive rate because on a macroscopic level, several benign tumors tend to mimic malignant melanoma, thus leading to a large number of unnecessary and scarring excisions (Ruocco 1999). Other diagnostic aids have come up over the years to aid the dermatologists in detecting cancer such as ultraviolet photography (Asawanonda 1999) and polarized photography (Anderson 1991). UV light is strongly absorbed by the melanin pigment and can be used to accentuate epidermal lesions containing melanin. Such information from UV photography can help enhance the detection of some melanomas (Marshall 1976; Murray 1988). Polarized photography uses polarizing filters to separate light reflected from the stratum corneum, which is parallel to the incident light polarization, from the unpolarized light

backscattered from the epidermis due to multiple scattering (Anderson 1991; Muccini 1995). Hence the degree of polarization of the diffuse reflection can help characterize the medium of propagation and selectively identify surface and sub-surface dermatologic conditions that are specific to a particular disease (Schmitt 1992; Jacques 2002). Polarized photography could thus be used to provide image contrast and enable identification of margins of superficial lesions. Such conventional approaches for cancer detection do not reach the deeper layers of tissue such as the upper dermis where early stages of melanoma are most likely to occur. Neither do they account for the transition of melanoma from the horizontal to the vertical growth phase (Erhard 1997), an important factor that could be missed when the diameter of the lesion is small. Extensive research has been conducted in the past few decades toward developing non-invasive sub-surface skin imaging modalities for melanoma diagnosis (Wang 1995; Ruocco 1999; Kollias 2002; Aspres 2003; Marghoob 2003). Some of these imaging modalities like OCT, for example, show excellent potential for moving from the bench to the clinic as a detection tool for skin cancer (Mogensen 2007).

Cytodiagnosis or Tzanck smear

Cutaneous cytodiagnosis, also known as Tzanck smear, is a simple, minimally invasive procedure that is both time and cost efficient as compared with biopsy. It is a very old technique introduced by Tzanck and finds applicability with certain types of skin tumors that exhibit diminished neoplastic cell cohesion that can therefore be exfoliated (Barr 1984; Ruocco 1999; Vega-Memije 2000). It is not painful, does not require an anesthetic and does not leave any scars and is therefore far friendlier to the patient. Predominantly used to test for BCC, the Tzanck

smear is reliable and can dictate the necessity for surgery without the need for further biopsy (Derrick 1994; Oram 1997; Powell 2000).

Dermoscopy

Dermoscopy is the incident light examination of the skin surface under magnification and permits distinction of morphological features that are not visible to the naked eye thus providing better criteria for the identification of disease-specific morphology including the differentiation between melanocytic and non-melanocytic naevi (Argenziano 1999; Menzies 2003). It is also known as epiluminescence microscopy, dermatoscopy, incident light microscopy etc. but the term ‘dermoscopy’ introduced by Friedman *et al.* has the most international consensus. Dermoscopy is a well recognized clinical tool currently used by one fourth of dermatologists in the United States (Tripp 2002).

Dermoscopy can serve as an effective diagnostic tool in the hands of experienced dermatologists, where it has been reported to improve diagnostic accuracy by 5% to 30%. However, there is a sharp learning curve associated with the accurate identification of distinct morphological patterns that could indicate a malignant lesion, and it has been shown that in fact, diagnostic accuracy can decrease in the hands of a novice (Binder 1995; Binder 1997). Since melanoma can be completely cured when removed early, a critical issue in the treatment of skin cancer is to remove malignant tumors during their early stages of development (Soyer 1987), while at the same time minimizing the excision of benign lesions. It has been shown that dermoscopy does not provide 100% sensitivity in terms of diagnostic accuracy. On the other hand, when used as an aid to clinical management in order to determine if a particular lesion warrants biopsy, 100% of melanomas and BCC’s were correctly classified (Argenziano 2002).

Confocal scanning microscopy

Confocal scanning microscopy is a real-time *in vivo* imaging technique with high lateral (0.5-1 μm) and axial resolution (2-5 μm) that can image skin up to a depth of about 350 μm , which covers the epidermis and the upper layer of the dermis (Rajadhyaksha 1999). Conventional confocal microscopes require fluorescent dyes in order to achieve sufficient contrast but recent developments, for instance, commercially available instrument the 'Vivoscope 1000' from Lucid Inc., Rochester NY can achieve contrast entirely through the reflected light. Operating wavelengths lie in the range of 800-1064 nm, which has been found to provide the best resolution and depth of imaging in human skin (Rajadhyaksha 1995; Rajadhyaksha 1999). The first *in vivo* confocal microscopy images of human skin were obtained up to a depth of 150 μm beneath the skin surface using a mercury lamp and a Nipkow disk for scanning in 1993 (Corcuff 1993). Several skin conditions have thereafter been studied using confocal microscopy, including amelanotic melanomas (Busam 2001). Confocal laser scanning microscopy has been found to be capable of identifying *in vivo* distinct patterns and cytological features of benign and malignant skin lesions (Langley 2001). Two-photon fluorescence microscopy, introduced by Denk and Webb approximately two decades ago, merges fluorescence spectroscopic methods within the confocal imaging set-up and has found many applications in biophotonics research (Denk 1990; Masters 1998; So 2000). More recently, multiphoton fluorescence microscopy has taken its place as the prevalent non-invasive fluorescence microscopic method for biological samples (Zipfel 2003; Chung 2005). Confocal microscopy is currently limited by a small field of view, typically $250 \times 250 \mu\text{m}$ (Huzaira 2001), and limited penetration that impedes macroscopic visualization of tumor margins for a direct clinical comparison.

Spectroscopy

Tissue spectroscopy has been investigated extensively in research for cancer diagnosis since it provides quantitative information about the tissue properties and helps eliminate errors from subjective interpretations, therefore can serve as a valuable supplement to histology. Skin tissue in particular, has been at the root of the investigation of spectroscopic imaging (Marchesini 1991; Sterenborg 1994; Marchesini 1995; Tomatis 1995; Richards-Kortum 1996; Zeng 1996; Bigio 1997), with an emphasis on *in vivo* diagnosis in recent years (Wagnieres 1998; Ramanujam 2000; Klaessens 2008; Tseng 2008; Zhao 2008).

Diffuse reflectance spectroscopy (DRS) is one of the simplest oldest spectroscopic methods (Edwards 1939) that studies the diffuse reflectance of light from the tissue surface after it undergoes multiple elastic scattering and absorption. DRS has been found to be able to distinguish between benign and malignant melanoma with a sensitivity of 90.3% and a specificity of 77.4% (Marchesini 1992). The spectral characteristics of this reflected and backscattered light provide valuable information about tissue morphological structure and biochemical composition (Mourant 1995). The optical properties of skin determined using DRS in terms of hemoglobin and melanin content and its optical scattering properties have been studied, analyzed and quantified by several researchers (Farrell 1992; Marbach 1995; Zonios 2001). Generally, wavelengths used are within the optical window of 600-1300 nm that allow the greatest penetration depth and maximum reflectance for skin (Parrish 1981). Penetration depths of up to 1 mm can be achieved in the near infrared region (Kollias 2002). Identification of precancerous lesions have been reported in several organs (Mourant 1995; Zonios 1999; Bigio 2000; Nordstrom 2001; Mirabal 2002; Breslin 2004), including skin (Wang 1995; Zeng 1996;

Sudha 2004). However, single scattering events are masked in the diffuse reflectance background that contains a much stronger signal. This leads to loss of useful information about epithelial tissue morphology such as the nucleus size, *pleomorphism*, *hyperchromasia* etc. (Perelman 1998; Jacques 2000).

Light scattering spectroscopy (LSS) captures the portion of the backscattered light that undergoes single scattering from the epithelial cells and thereby preserves its polarization by filtering the unpolarized component during detection (Backman 1999). LSS has also been used to image and differentiate between the different layers of human skin (Demos 1997). Recently, Gurjar *et al.* have developed a pre-clinical modality using LSS that enable *in vivo* spectral mapping of large epithelial areas with an accuracy of better than 0.1 μm , smaller than the wavelength of light at 0.5 μm . LSS can thus measure nuclear size and dynamics thus demonstrating feasibility for LSS as a biomedical tool detect and study the progression of cancer (Gurjar 2001).

When emitted light after excitation of the cell molecules is spectrally analyzed for tissue properties, it is called fluorescence spectroscopy. Critical research efforts have been directed toward using tissue fluorescence spectroscopy, be it endogenous or exogenous fluorescence behavior (Zeng 1995a; Kollias 1998; Svanberg 1998; Wennberg 1999) to enable differentiation between cancer and pre-cancer pathology (Richards-Kortum 1996) and detect malignant tissue (Richards-Kortum 1991; Wagnieres 1998; Brancalion 2001; Broer 2004). *In vivo* auto-fluorescence of skin has been found to be dominant for excitation spectra of just below 300 nm to about 400 nm and emission and reflection spectra are collected at about 300-500 nm (Zeng 1995b; Kollias 1998). Penetration of the excitation source has been found to be limited to the

epidermis and upper dermis and does not reach the deeper vessels of the dermis (Brancaleon 2001).

Several studies have reported the potential of vibrational spectroscopy, infrared absorption, and Raman scattering to characterize biological tissues and further enhance specificity of spectroscopic diagnosis. Vibrational infrared spectroscopy has been investigated extensively in the last decade and has been found to reveal information about the state and health of tissue (Diem 2004). The first attempt at investigating vibrational spectroscopy for disease detection showed significant promise and was reported in the early nineties by Wong *et al.* (Wong 1991). Higher spatial resolution for more accurate identification of spectral indicators of disease was later achieved by integrating microscopic methods into spectroscopy (Diem 1999). Since vibrational spectroscopy allows for the non-invasive investigation of biological tissue properties on a molecular basis it was examined extensively for several biomedical applications, (Workman Jr 1999; Petrich 2006).

Two different spectroscopic methods are used to interpret molecular vibrations, namely, mid-infrared spectroscopy and Raman spectroscopy (Schrader 1995; Mirabella 1998; Gremlich 2001). The penetration depth of mid-infrared radiation is only up to a few micrometers and has therefore been extensively used to study only the outermost dead layer of skin namely, the stratum corneum, usually to measure skin hydration (Mendelsohn 2003). The implementation of the Fourier transform method in mid-infrared spectroscopy considerably enhanced the imaging sensitivity (Perkins 1986). Crupi *et al.* reported the feasibility to distinguish between normal and malignant cells for two types of skin cancer, namely, epithelioma and basalioma, using FT-IR spectroscopy (Crupi 2001). Very recently, Moss *et al.* used a high brilliance synchrotron light

source (Moss 2005), demonstrated to be safe and non-toxic to living cells (Holman 2003) in order to achieve high spatial resolution of the order of single cells (2.5-10 μm) with a high signal to noise ratio using infrared spectroscopy of living cells.

In 1995, Raman spectra were found to be able to distinguish between benign and malignant breast tissue (Frank 1995). Following that, Edwards *et al.* studied the feasibility of skin spectral diagnosis using FT-Raman spectroscopy (Edwards 1995). Soon after, Gniadecka *et al.* reported the ability to distinguish BBC from normal healthy skin and later between benign and malignant for different skin diseases including squamous cell carcinoma using NIR-FT Raman spectra (Gniadecka 1997a; Gniadecka 1997b) and proved that NIR-FT-Raman spectroscopy may be an important *in vivo* tool for early skin cancer diagnosis. A specificity and sensitivity of 98% respectively have been demonstrated for Raman spectroscopy using the neural network analysis for the BCC cases and 85% and 99% respectively, for the malignant melanoma cases (Gniadecka 2004). The Raman spectrum of a thumb published in 1998 by Fendel *et al.* showed that *in vivo* measurements are possible without fluorescence and detectable destruction (Fendel 1998). One of the early problems of Raman imaging was that it suffered from very low signal to noise ratio because of overlap with endogenous fluorescence, where a sensitivity and specificity of 79% and 88% respectively, was reported for detecting dysplasia (Georgakoudi 2001). Raman spectroscopy at near infrared wavelengths, first suggested by Schrader (Schrader 1999), significantly improved image contrast. In addition, NIR Raman spectroscopy provided better penetration depth, an important advantage compared to mid-infrared imaging. Another problem with Raman spectroscopy in the early stages was low spatial resolution and this was solved using different kinds of microscopy from standard (Turrell 1996) to near-field (Smith 1995) to confocal microscopy in the imaging set-up (Brenan 1996; Caspers 2003). The latter set-up

however, again limited penetration depth. Recently Raman spectroscopy has also been increasingly investigated for the *in vivo* examination of skin and skin lesions (Fendel 1998; Stone 2004). In 2005, Tfayli *et al.* showed that melanin vibrations from FTIR microspectroscopy are useful to discriminate naevi from melanomas (Tfayli 2005).

Terahertz pulse imaging

Terahertz pulse imaging (TPI) is a recent coherent optical imaging modality using electromagnetic radiation in the 30 μm to 3 mm wavelength regime that has begun to be explored with the advancement in technology for high frequency sources and detectors in the last decade. Typical operating frequencies lie in the range of 0.1 THz to 10 THz (or correspondingly, a wavelength range of 3mm to 30 μm) that excite vibrational modes of molecules leading to spectroscopic data, and therefore good contrast (Arnone 1999; Cole 2001; Woodward 2001; Woodward 2002a). Additionally, the coherence property allows it to obtain both phase and amplitude. The THz radiation used being low power (1mW) and non-ionizing, it is thought to be non-hazardous to skin (Woodward 2002a). Early studies of biological tissue *in vitro* have shown potential to discriminate between tissue types (Cole 2001), and between BCC and normal skin tissue (Woodward 2001). In 2002, BCC was reported to show a positive contrast relative to normal skin tissue using TPI. TPI has therefore demonstrated feasibility as an optical imaging modality for the study of skin disorders, including cancer (Woodward 2002b).

MR microscopy

Several early studies have been conducted for MRI imaging of the skin, however the spatial resolution achieved in MRI (1 mm) has been insufficient for imaging the epidermis (Hyde 1987;

Querleux 1988; Wood 1988; Schwaighofer 1989; Zemtsov 1989). Kim *et al.* demonstrated the ability to differentiate normal and malignant skin *in vitro*. Thereafter, specific microscopic devices have been developed to image skin layers *in vivo* (Bittoun 1990). Researchers have attempted to combine spectroscopy to MRI in order to help improve accuracy of detection leading to Magnetic Resonance Spectroscopic Imaging (MRSI) (Parivar 1996). Currently MRI imaging for skin is mainly used only as a research tool (Richard 1993; Querleux 1994; El Gammal 1996; El Gammal 1999).

Ultrasonography

Ultrasonography was first introduced in 1979, when it was used to measure skin thickness (Alexander 1979). While typically it operates in the 20-25 Mhz range, for dermatological applications frequencies between 40-100 MHz are required to provide sufficient axial (17-30 μm) and lateral (33-94 μm) resolution. (Turnbull 1995; El Gammal 1999). While higher resolution in order to visualize the epidermis can be achieved at 500 MHz ultrasonic frequencies, this will damage living tissue and is not applicable *in vivo* (Barr 1991). High frequency ultrasound is capable of visualizing tumor dimensions *in vivo* (Lassau 1997) but its inability to differentiate between benign and malignant skin lesions (Fornage 1993; Hoffmann 1999) makes its role limited, with the risk of false diagnosis.

SIAscopy and multispectral analysis

Spectrophotometric Intracutaneous Analysis (SIAscopy) is a real-time imaging technique for imaging pigmented skin lesions and a possible contender as a tool to aid the dermatologist in cancer diagnosis (Cotton 1998; Moncrieff 2002). This is a computerized technique using

multispectral imaging that attempts to eliminate the subjectiveness in clinical diagnosis of melanoma. The basic principle involves measuring and evaluating reflected radiation from skin following exposure to light in the visible (400-700 nm) and NIR (700-1000 nm) and uses computer algorithms to assess skin content such as melanin, vasculature, and collagen. Multispectral analysis has previously been investigated as an extension to digital dermoscopy for distinguishing pigmented skin lesions including melanoma (Marchesini 1992; Wallace 2000; Elbaum 2001). More recently, a multispectral imaging system for melanoma detection has been reported by Tomatis *et al.* (Tomatis 2005). A high number of false positive reports that result from the lack of sufficient selection criteria is the current limitation of this method. With further research and analysis, this technique could present great potential as a diagnostic aid (Farina 2000).

1.4 Optical Coherence Tomography and Skin Imaging

Optical Coherence Tomography/Microscopy (OCT/OCM) is an emerging technology with good potential application in dermatology. OCT is based on low temporal coherence interferometry that has demonstrated the capability to image microscopic structures in biological tissues at sub 10 μm resolution and at depths beyond the scope of conventional endoscopy and confocal microscopy. When fully exploited, the technology has the potential to dramatically change the way medical practitioners examine, study, and understand the human body. Dermatology is an important application domain of OCT; however, some of the issues such as imaging speed and resolution are still being resolved by researchers before it can proceed to a clinical setting. As the technology matures, it may be possible to perform optical biopsies using OCT imaging alone, therefore completely eliminating all risk factors involved with excisional biopsy.

OCT imaging was pioneered by Fujimoto *et al* in 1991 (Huang 1991) and is only a few decades old. OCT imaging can be performed over approximately the same distance as a biopsy at high resolution. The real-time aspect of OCT makes the most attractive applications for OCT those where conventional biopsies cannot be performed or are ineffective. Its roots lie in early work on white light interferometry that led to the development of optical coherence-domain reflectometry (OCDR), a one dimensional optical ranging technique. It was originally developed for finding faults in fiber optic cables (Takada 1987; Youngquist 1987) and network components. Thereafter, it was used in other non-medical applications such as industrial metrology, thickness measurement in thin films, non-destructive evaluation of paint etc. (Flournoy 1972; Li 1995; Xu 1999). Its potential for medical applications was soon recognized and researchers began to investigate its ability to probe biological tissue structures (Brezinski 1996; Brezinski 1999).

While probing depths exceeding 2 cm have been demonstrated at high resolution in transparent tissues such as in ophthalmology, in highly scattering media such as the skin, images are typically obtained as deep as 1-2 mm (Hee 1995; Schmitt 1995; Brezinski 1996; Boppart 1998; Brezinski 1999; Gladkova 2000; Welzel 2001; Bordenave 2002). OCT has already been successfully implemented as a clinical product for ophthalmic diagnosis (Carl Zeiss Meditec, Dublin, CA; Optovue, Fremont, CA.). Ultra-high resolution techniques have been reported for imaging in biological tissue (Drexler 1999; Drexler 2004), thus enabling the technology for the assessment of tissue and cell morphology *in situ*. However, *in vivo* invariant high resolution, both transverse as well as axial, is a key issue that is being investigated in dermatology (Schmitt 1995; Gladkova 2000; Welzel 2001). While OCT has the potential to be used for a variety of medical applications, pre-cancer and cancer represents one of the most pressing and promising application areas (Korde 2007).

CHAPTER 2- OPTICAL COHERENCE MICROSCOPY

Optical Coherence Microscopy (OCM) uses low-coherence interferometry to extract 3D structural information of biological tissue samples not only at high axial resolution but also at high lateral resolution through the integration of high NA optics. Microscopy in living biological tissue can be compared to confocal imaging in a turbid media, i.e., the reflectivity decreases exponentially with depth, and rejection of multiple scattering is not an intrinsic phenomenon. The addition of coherence gating to confocal microscopy through interferometry significantly diminishes the collection of multiply scattered light. Optical coherence microscopy therefore combines the advantages of high lateral resolution confocal microscopy with the coherence gating of low coherence interferometry that leads to high axial or depth resolution, while at the same time facilitates imaging deeper (up to 1mm in depth) in highly scattering media.

2.1 Time-Domain Principle of OCM

The basic instrumentation for OCM consists of a Michelson interferometer operated in the time domain (TD-OCT). Light is coupled into the sample and reference arms of the interferometer using a beamsplitter. The axial profile (A-scan) is obtained by scanning the reference mirror and the focal plane inside the sample synchronously in depth. A 2D depth cross-section is obtained by scanning laterally (B-scan), thus obtaining a series of axial reflectivity data. The interference signal obtained from the backscattered and reflected light from the sample and reference mirror is collected at the detector and is processed to derive the path length information, i.e., the structure of the sample. An interference signal is registered only when the mismatch between the reference and sample arm path lengths is within the coherence length of the source.

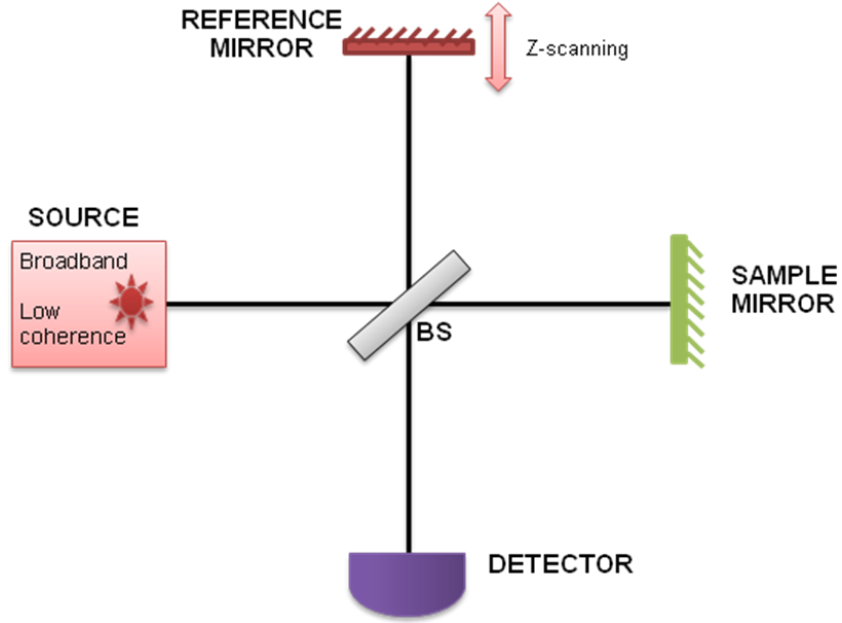


Figure 2.1: TD-OCT interferometer schematic

In order to explain the basic theory behind TD-OCM, the let us consider the simple TD-OCT schematic shown in Fig.2.1 and start with a monochromatic light source. Let us assume 100% reflectivity for the reference and sample mirrors. Suppose the reference and sample arms have a path length of l_R and l_S respectively with respect to the beam splitter. The electric field at the detector in this case is given by the sum of the electric fields generated in the reference and sample arm defined independently in Eq.2.1 as

$$E_R = A_R \cdot \exp[-j(\beta_R l_R - \omega t)] \text{ and,}$$

$$E_S = A_S \cdot \exp[-j(\beta_S l_S - \omega t)] , \tag{2.1}$$

where, E_R and E_S represent the electric fields, A_R and A_S the amplitudes, β_R and β_S the propagation constants, and l_R and l_S the round-trip ‘optical’ path lengths in the reference and sample arms respectively. The intensity at the detector I_D would then be given by

$$\begin{aligned} I_D &\propto |E_R + E_S|^2 \\ &= |A_R|^2 + |A_S|^2 + 2 \operatorname{Re}\{E_R E_S^*\}, \end{aligned} \quad 2.2$$

where, the interference is contained in the reference-sample interference term $E_R E_S^*$.

$$\begin{aligned} \operatorname{Re}\{E_R E_S^*\} &= A_R A_S \cos(\beta_R l_R - \beta_S l_S) \\ &= A_R A_S \cos\left(\frac{2\pi}{\lambda} \cdot l_D\right), \end{aligned} \quad 2.3$$

where, the propagation constants β_R and β_S equal $\frac{2\pi}{\lambda}$ for free space propagation assuming zero absorption, and $l_D = l_S - l_R$ is the optical path length mismatch between the reference and sample arms.

In the case of OCM where a low coherence broadband source spectrum is used, the electric fields in the reference and sample arms are a function of the source frequency ω as given in Eq.2.4.

$$\begin{aligned} E_R(\omega) &= A_R(\omega) \cdot \exp[-j(\beta_R(\omega)l_R - \omega t)] \text{ and,} \\ E_S(\omega) &= A_S(\omega) \cdot \exp[-j(\beta_S(\omega)l_S - \omega t)]. \end{aligned} \quad 2.4$$

In this particular case, we assume a 50-50 split of the source intensity at the beamsplitter and equal reflectivities of the sample and reference mirrors and therefore, we can define

$A_R(\omega) = A_S(\omega) = E_0(\omega)$. The reference-sample interference term can now be extended by integrating it over the bandwidth frequencies of the source. Therefore, the intensity at the detector is now proportional to

$$\begin{aligned} I_D(\omega) &\propto \text{Re}\left\{\int_{BW} E_R(\omega)E_S^*(\omega) \cdot d\omega\right\}, \\ &\propto \text{Re}\left\{\int_{BW} S(\omega)\exp[-j\Delta\phi(\omega)] \cdot d\omega\right\} \end{aligned} \quad 2.5$$

where, $S(\omega) = |E_0(\omega)|^2$ and $\Delta\phi(\omega) = \beta_S(\omega)l_S - \beta_R(\omega)l_R$ expresses the phase difference across the spectral frequencies. When achromatic mirrors are used in the reference and sample arms and if there is no dispersion within the system, $S(\omega)$ essentially represents the equivalent of the source spectrum and $\phi(\omega)$ is the phase difference between the sample and reference arms at each wavelength.

If we assume a Gaussian source spectrum $S(\omega)$, the axial resolution of the system can be estimated to be the FWHM of the axial point spread function at the detector and is equal to half the coherence length of the source spectrum. For a Gaussian beam propagation in a free space interferometer, i.e. dispersion free, the FWHM axial resolution is inversely related to the bandwidth of the source and is given by

$$\Delta z_{FWHM} = \frac{l_c}{2} = \frac{2 \ln 2}{\pi} \left(\frac{\lambda_0^2}{\Delta\lambda} \right), \quad 2.6$$

where, λ_0 represents the central wavelength of the spectrum and $\Delta\lambda$ is the spectral bandwidth (Bouma 2002). Thus the axial resolution of the OCT system is determined by the broadband low coherence source used. This spectral dependence provides a fundamental advantage to OCM and

OCT compared to conventional and confocal microscopy in that the axial resolution is decoupled from lateral resolution (Kino 1990). The development of high speed, large bandwidth sources is therefore an area of active research, and axial resolutions of the order of $1\ \mu\text{m}$ have been achieved (Povazay 2002; Xue 2008).

In addition to the coherence gating property that provides depth resolution in OCT, there also exists a property of the microscope that characterizes the lateral response of the imaging purely as a function of the optics used in the sample arm. As a result, in early advances in Time Domain OCT (TD-OCT), scientists took the natural step of increasing the numerical aperture (NA) of the optics in the sample arm in an attempt to improve lateral resolution (defined in Eq. 2.7), creating Time Domain Optical Coherence Microscopy (TD-OCM)(Izatt 1994).

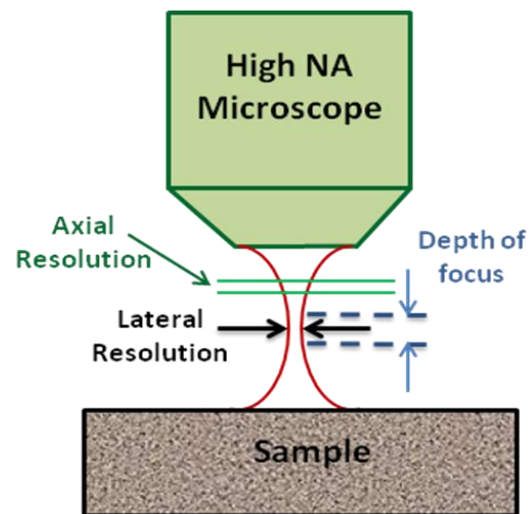


Figure 2.2: Trade-off parameters in OCM

$$\Delta x = \frac{1.22\lambda_0}{2NA} \quad . \quad 2.7$$

However, the high NA microscope eliminated the ability to gather useful data over long depths (of a few mm) because although the lateral resolution was now improved at the focus of the beam, it deteriorated quickly outside the depth of focus (DOF) region (tens of microns).

The depth of focus (DOF) has been defined by authors in several ways. In OCT in general, it is defined to be related to the confocal parameter of the Gaussian beam, or twice the Rayleigh range. The Rayleigh range corresponds to the propagation distance over which the beam waist diameter increases by a factor of $\sqrt{2}$ and is defined in Eq.2.8.

$$DOF = \pm 2 \cdot \frac{\bar{\lambda}}{\pi\theta_s^2} \quad 2.8$$

where, $\bar{\lambda}$ represents the mean wavelength of the imaging source, and θ_s represents half of the angular spread of the beam. In microscopy, the DOF may be defined by the Rayleigh quarter-wave defocus criterion, and can be expressed in terms of the wavelength and NA of the optics as shown in Eq.2.9.

$$DOF = \pm \frac{\bar{\lambda}}{2 \cdot NA^2} \quad 2.9$$

It is well established that regardless of the criteria used, DOF has an inverse quadratic dependence on NA and linear dependence on the mean wavelength. This fundamental trade-off between lateral resolution and depth of focus has led to different solutions and schemes for recovering lateral resolution through the depth range in the time domain, involving both moving

Table 4: Introduction and state-of-the-art for predominant OCT/OCM technologies

Technology Introduction date ↓	Central wavelength (nm)	Spectrum width (nm)	Axial Res. (μm)	Lateral Res. (mm)	Depth of field (mm)	Speed (#A- scans/s)	State of Art ↓
TD-OCT (Huang 1991)	SLD 1310nm	49	~15	Est.~25	2	4,000	(Rollins 1998)
TD-OCM (Izatt 1994)	Ti:Al ₂ O ₃ laser 800nm	100	3	2	Est.~0.1	(en face image)	(Aguirre 2003)
FD-OCT (Fercher 1995)	Ti:Sa laser 800nm	144	Not yet available	Not yet available	Not yet available	312,000	(Povazay 2009)
SS-OCT (Chinn 1997)	Fourier mode lock 1313 nm	74	12.7	Est.~20	~1	370000	(Eigenwillig 2009)
DF TD-OCM (Schmitt 1997)	SLD 820nm	77	3.8	3	0.43	~190	(Lexer 1999)
C-mode OCM (Drexler 1999)	Swept source 1300nm	88	12.6	4.5	0.6	16,000	(Huber 2005)
GD-OCM (Rolland 2008)	Ti:Sa laser 820nm	120	2.5	3.5	2	12,000	(Rolland 2009)
Super Continuum TD-OCT (Povazay 2002)	Super continuum Ti:Sa 540nm	250	0.64	4	Not specified	Not specified	(Xue 2008)

and non-moving parts as will be discussed in the literature review later in this Chapter. Fig. 2.2 shows a schematic of the different contributing parameters in OCM. Table 4 summarizes the state-of-the-art systems in various OCT/OCM domains with respect to the most significant parameters that offset overall performance, namely, axial resolution, lateral resolution, depth of field and scanning speed.

A primary limitation to focus-tracking in the time-domain is the system imaging speed, which is limited by having to continually track the sample arm focus in the reference arm. Imaging speed

is a crucial requirement for *in vivo* imaging, especially when the technique is extended to 3D image acquisition. High speed 3D imaging is relevant to OCM in order to enable this technology for potential clinical applications such as cancer detection and diagnosis. This shortcoming in TD-OCM led to the development of Spectral Domain OCT (SD-OCT) that enabled high speed image acquisition.

2.2 Spectral Domain Optical Coherence Tomography

A different configuration of OCT called Spectral domain OCT (SD-OCT), which works based on Fourier Domain principles has gained prominence in recent years. SD-OCT can be considered to be a form of spectral radar and was originally proposed by Häusler in 1996 (Häusler 1998). SD-OCT also uses the same low coherence broadband source in a Michelson interferometer set-up in order to obtain axial intensity profiles (A-scans) of a scattering sample. However, it does not require depth or z-axis scanning of the reference mirror in order to determine the path length within the sample. The need for depth scanning in SD-OCT is eliminated because the depth or pathlength information is encoded within the recorded intensity spectrum as demonstrated in Fig. 2.3. While in TD-OCT and TD-OCM, the backscattered signal across the depth is measured sequentially, in SD-OCT, the depth information is encoded in the recorded spectrum of the interference signal in the detector arm. Therefore, SD-OCT offers the important advantage of faster A-scans that present a step forward for *in vivo* imaging. Within the field of SD-OCT, two basic SD-OCT technologies have emerged, referred to as Fourier Domain OCT (FD-OCT) and Swept Source OCT (SS-OCT).

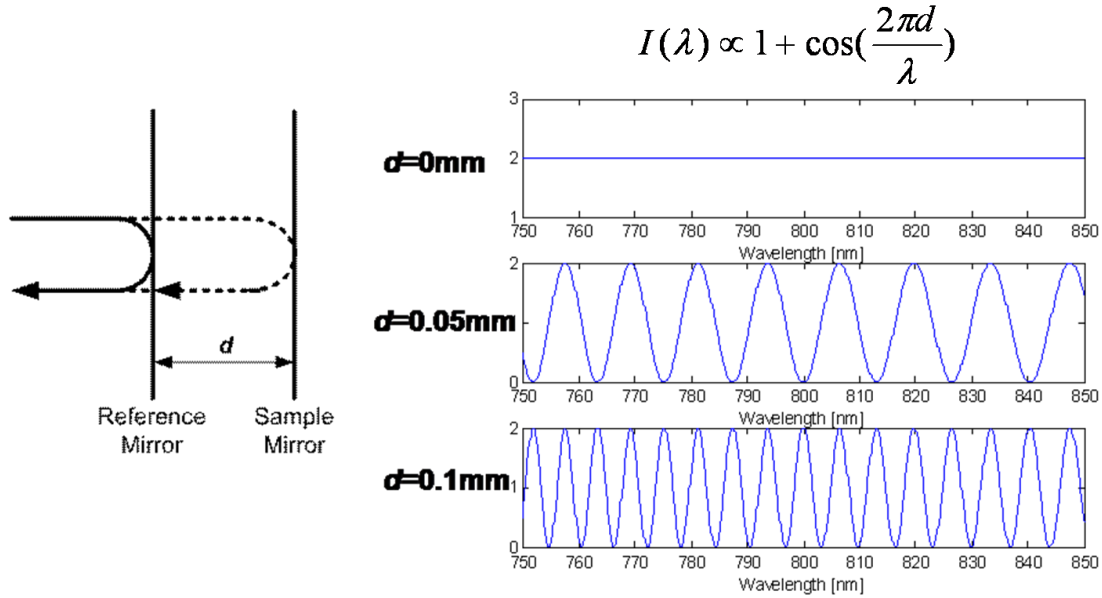


Figure 2.3: Diagram illustrating depth encoding in the interference signal detected in SD-OCT

2.2.1 Fourier domain OCT (FD-OCT)

A typical FD-OCT set-up is shown in Fig.2.4. It consists of a broadband low coherence source in the sample arm. The reference mirror is fixed and is not required to be translated for depth scanning. In a fiber optics based interferometer, the reference arm also has a dispersion compensation system since the fiber optics, the sample, and other dispersive components may contribute significantly to dispersion resulting in degradation of the axial resolution. The interference signal between the sample and reference light is spectrally decomposed in the detector arm using a diffraction grating, and recorded on CCD or CMOS array detectors. The inverse Fourier transform of the signal on the detector yields the depth reflectivity profile of the sample.

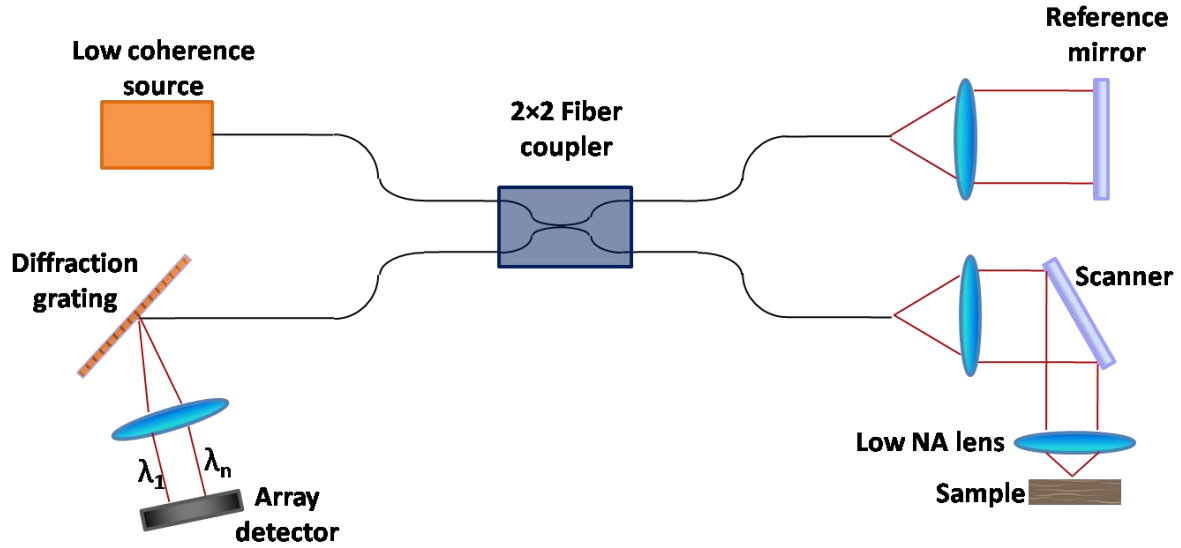


Figure 2.4: Schematic for Fourier domain OCT

Mathematical principle of FD-OCT/OCM

The signal at the detector is a sum of the reflections from different depths of the sample. In the rest of the chapter, the hat symbol denotes a quantity in the frequency domain. We assume a 50% light intensity split at the beam splitter that is then propagated into the reference and sample arms. Suppose $\hat{E}_R(k)$ and $\hat{E}_S(k)$ are the backscattered signals from the sample and reference arms as a function of spatial frequency $k = \frac{2\pi}{\lambda}$ in free space as outlined in Eq. 2.10.

$$\hat{E}_R(k) = \frac{\hat{E}_0(k)}{\sqrt{2}} r_R \exp(ikl_R - \omega t) \text{ and,}$$

$$\hat{E}_S(k) = \frac{\hat{E}_0(k)}{\sqrt{2}} \int_{-\infty}^{+\infty} r_s(l_s) \exp(ikl_s - \omega t) dl_s, \quad 2.10$$

where, $\hat{E}_0(k)$ is the source spectral amplitude function, l_R and l_S represent the round-trip optical pathlengths in the reference and sample arms respectively, and r_R and $r_s(l_s)$ represent the reflectivity of the fixed reference mirror and the various layers of the sample respectively. The signal at the detector $\hat{I}_D(k)$ can be expressed as

$$\begin{aligned}\hat{I}_D(k) &= \left| \hat{E}_R(k) + \hat{E}_S(k) \right|^2 = \frac{\hat{S}(k)}{2} \cdot \left| r_R e^{ikl_R} + \int r_S(l_S) e^{ikl_S} dl_S \right|^2 \\ &= \frac{\hat{S}(k)}{2} \cdot \left(|r_R|^2 + 2r_R \int r_S(l_S) \cos(k(l_S - l_R)) dl_S + \left| \int r_S(l_S) e^{ikl_S} dl_S \right|^2 \right)\end{aligned}\tag{2.11}$$

where, $\hat{S}(k) = \left| \hat{E}_0(k) \right|^2$ is the source spectral intensity. It can be seen that the detected signal is a sum of three terms. The first term is the constant DC offset which is a background noise that arises from the reference arm independent of sample scanning. Typically, this DC noise is removed during the experiment by subtraction of the pre-recorded background noise from blocking the sample beam (Lindner 2002). Another method for DC removal is to perform an average of all A-scans within a B-scan of the sample. This isolates the residual DC component that can be subtracted from each A-scan (Wang 2006). The second term is a sum of cosines that encodes the amplitude at a sample depth l_S as a function of the spatial frequency k . The term $r_S(l_S)$ can be decoded by the application of a Fourier transform to the interference cosine signal. The third term is an autocorrelation that arises from interference within the sample arm. This AC noise is much weaker than the interference signal. It is typically located close to the DC noise for a thin sample and can be isolated experimentally by introducing an offset distance between the

object and reference planes in the interferometer. Assuming that the 1st and the 3rd ‘noise’ terms are removed, the detected ‘interference’ signal can now be simplified to

$$\hat{I}_{\text{int}}(k) = \hat{S}(k) \cdot r_R \int r_S(l_S) \cos(k(l_S - l_R)) dl_S. \quad 2.12$$

In order to recover the sample reflectivity as a function of depth or distance, let’s define the optical path difference $l_D = l_S - l_R \Rightarrow dl_D = dl_S$. It must be noted that l_D therefore includes the effect of refractive index in the sample and reference arms. Using the relation

$\cos(kx) = \frac{e^{ikx} + e^{-ikx}}{2}$, the interference signal can be re-written as

$$\begin{aligned} \hat{I}_{\text{int}}(k) &= \frac{\hat{S}(k)}{2} \cdot r_R \int r_S(l_D + l_R) [e^{ik(l_D)} + e^{-ik(l_D)}] dl_D. \\ &= \frac{\hat{S}(k)}{2} \cdot r_R \left(\int r_S(l_D + l_R) e^{ikl_D} dl_D + \int r_S(l_D + l_R) e^{i(-k)l_D} dl_D \right) \end{aligned} \quad 2.13$$

The inverse Fourier transform of $\hat{I}_{\text{int}}(k)$ can be obtained resulting in the sample reflectivity in the spatial domain as a function of optical path difference, thus characterizing the structure of the sample.

$$I_{\text{int}}(l_D) = \mathfrak{F}^{-1} \{ \hat{I}_{\text{int}}(k) \} = \frac{r_R}{2} \cdot \mathfrak{F}^{-1} \{ \hat{S}(k) \} * [r_S(l_R + l_D) + r_S(l_R - l_D)] \quad 2.14$$

$I_{\text{int}}(l_D)$, detailed in Eq.2.14, represents the signal in the spatial domain and outlines the structural information across the depth of the sample recovered from the OCT interference signal. However, since a Fourier transform was applied to revert to the spatial domain, the inherent

property of the Fourier transform gives rise to a mirror image or a ghost image of the reflectivity equally spaced in distance on the negative side of the reference or DC signal location.

This mirror image formation is demonstrated using one such spectrometer-based fiber optic FD-OCT system developed in our laboratory shown in Fig. 2.5 (Lee 2008a). To achieve high axial resolution in the system, we integrated a high power, broadband femtosecond Ti:Sa laser source centered at 800 nm with a spectral width 120 nm (FWHM), corresponding to $\sim 2.4 \mu\text{m}$ axial resolution in air (Femtolasers Inc.) into the system. A spectrometer (HR 4000; Ocean Optics Inc.) images an optical bandwidth of 200 nm onto a 3648 CCD pixel line array with a spectral resolution of 0.054 nm per pixel corresponding to an axial measurement range of ~ 2 mm. A custom designed 80/20 fiber coupler was used to support the broad bandwidth of the light source.

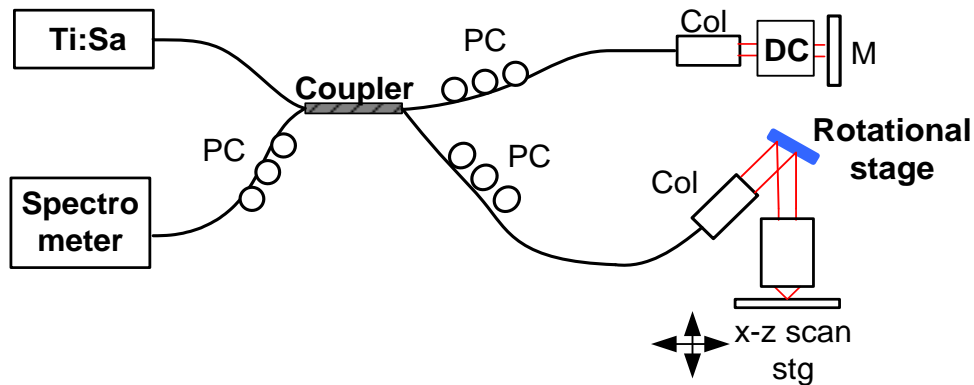


Figure 2.5: FD-OCM layout used in this research

In the imaging path, an 80% intensity beam from the fiber coupler is collimated to a 2 mm diameter beam (full width at $1/e^2$), and focused by a microscope objective integrated into the sample arm of the OCT system. The 20% intensity beam is used as a reference and passes through a Fourier domain optical delay line (FD ODL) located in the reference arm to control the

overall dispersion in the system (Lee 2005). A polarization controller (Thorlabs, Model FPC030) was used to maximize the signal modulation contrast. An onion sample was imaged using a low numerical aperture (NA 0.08) objective in the sample arm. As can be seen in Fig. 2.6, the surface of the onion has a path difference of 0.5 mm from the reference mirror. The sample reflectivity signal and consequently the 2D depth cross-sectional image form mirror images on either side of the zero path difference point.

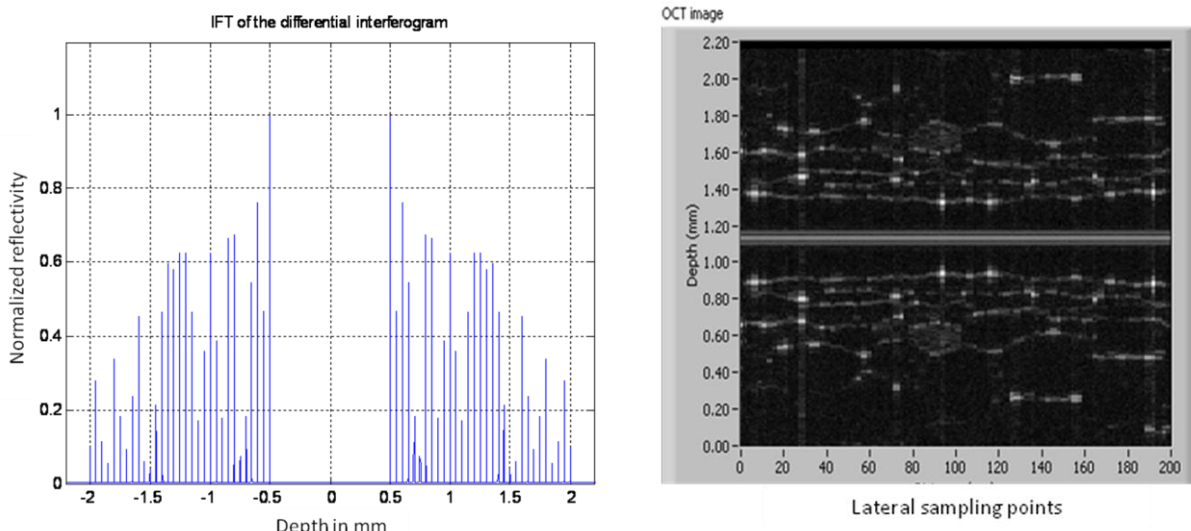


Figure 2.6: Mirror image property in (a) the axial intensity signal profile (b) 2D B-scan of an onion

2.2.2 Swept source OCT (SS-OCT)

FD-OCT has attracted much attention due to the significantly improved sensitivity and imaging speed in comparison to TD OCT because of the elimination of the depth scan. However, the main drawback is that the use of a detector array renders the OCT system expensive. At the same time, the system was still limited in speed to some extent because of the CCD readout rates. This issue led to the development of a different spectral domain system, namely, swept-source based

OCT (SS-OCT) that employs a wavelength tuning source instead of a pulsed broadband source (Fercher 1995). Therefore, the interference spectrum can now be recorded sequentially in time using a single photodiode as shown in Fig. 2.7. In addition, SS-OCT may be more suitable for systems using wavelengths over 1100 nm because the spectrometer based FD-OCT systems require an InGaAs CCD camera for detection in this spectral region—an expensive alternative. Thus SS-OCT provides the advantage of a cost-effective detection system. The development of high speed broadband swept sources continues to be an active area of research (Huber 2006; Jeon 2008).

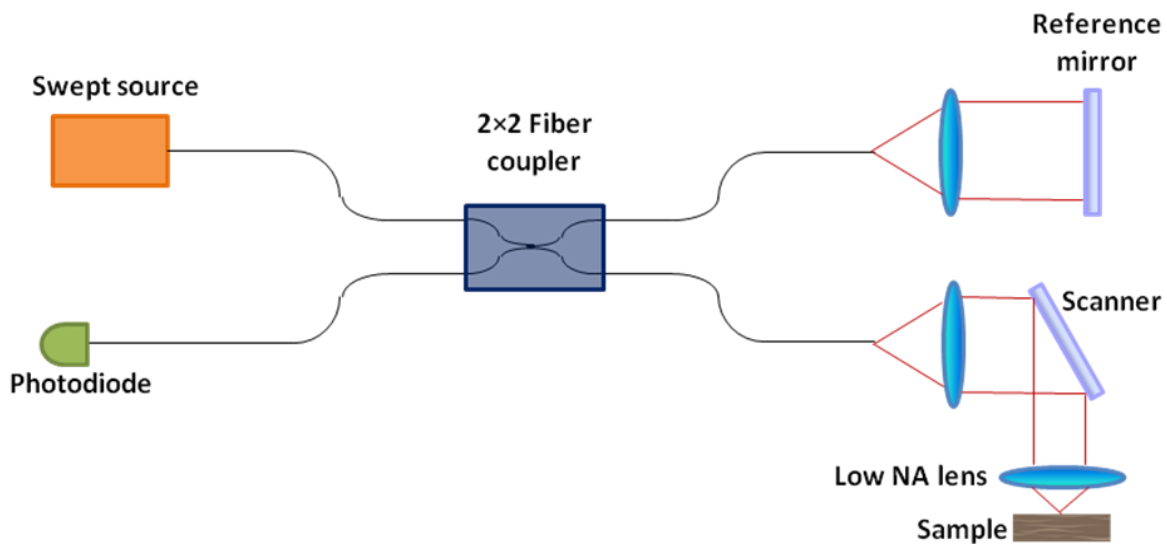


Figure 2.7: Schematic for Swept Source OCT

2.3 Dynamic Focusing – Related Work

Besides axial resolution, two parameters that are critical to OCT imaging are transverse or lateral resolution, and depth of field. The transverse resolution is measured from the size of the focused image spot in the case of incoherent illumination. It is dependent on the mean wavelength of the

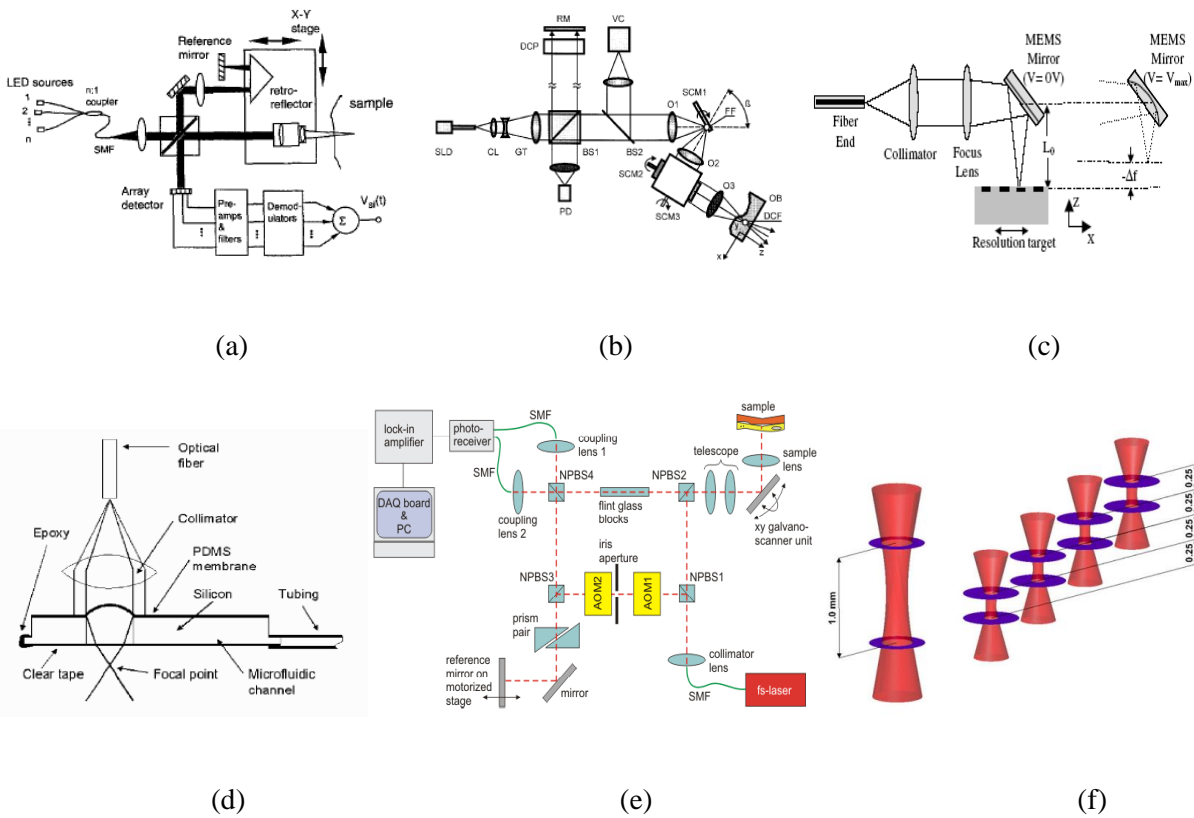


Figure 2.8: Different schemes that incorporate dynamic focusing (a) Schmitt *et al.* 1997, (b) Drexler *et al.* 1999, (c) Qi *et al.* 2004, (d) Divetia *et al.* 2005, (e) Wiesauer *et al.* 2005, and (f) Michelson Diagnostics 2008

source spectrum and the NA of the microscope used in the sample arm, as defined earlier in Eq. 2.7. The axial resolution of the system, on the other hand is limited by the coherence length of the source as defined earlier in Eq. 2.6.

The generalization of the axial resolution in the case of a non-Gaussian spectrum has also been investigated by Akcay *et al.* (Akcay 2002). It can be surmised from Eqs. 2.6 and 2.7 that axial resolution is independent of transverse resolution. This property allows for high axial resolution

while imaging structures that do not permit high lateral resolution since they are not accessible using high numerical aperture (NA) beams. If high NA beams are used by introducing focusing optics in the sample arm, high lateral resolution is enabled in OCM (Izatt 1994).

The critical need for dynamic focusing in OCM has been recognized in order to allow OCM to effectively improve on imaging resolution (Schmitt 1997). Dynamic focusing has been previously investigated and implemented using several schemes for OCM. Schmitt *et al* first described a system that dynamically focused inside the sample by the use of a common translation stage for both the imaging objective and a retro-reflector used in the reference arm, thereby mechanically moving both the reference and sample arm in synchronicity. Lexer *et al.* suggested the use of an optical setup where the sample is moved for each depth scan while the arms of the interferometer remain constant. In this method, an oscillating beam focus formed through reflection from an oscillating mirror was axially magnified M times by lenses before illuminating the sample. At each discrete point of the oscillation, the optical path difference resulting from the oscillating beam focus first formed caused a corresponding dynamic shift in the beam focusing in the sample (Lexer 1999). More recently, B. Qi *et al.* proposed a high-speed dynamic focus control system based on a micro-electromechanical (MEMS) mirror that is deformable. The MEMS mirror shifts the focus position of the sample beam to match with the coherence gate position for each lateral scan (Qi 2004). With this design, dynamic focusing is achieved at high speeds since it does not involve bulk optics. An alternate method was proposed by A. Divetia *et al.* where dynamic focusing was demonstrated experimentally using a liquid-filled polymer lens whose curvature is controlled by variation of the hydraulic pressure in the lens. The latter system required no moving parts. Authors demonstrated a resolution of 10 μm

across a 1.4 mm wide resolution target in air at the shortest focal length of the lens of 3 mm. While it was shown that the lens can vary its focal length up to a value of 16 mm, no quantification of resolution across depth was provided (Divetia 2005). Wiesauer *et al.* proposed dynamic focusing in a TD-OCM set-up where they employed two motorized translation stages, one for the reference arm and the other in the sample arm (Wiesauer 2005). A telescopic system is integrated in the sample arm and the second lens of the telescope is used as a zoom lens, mounted on the translation stage to control focal length. This set-up was built for retinal imaging and with an axial resolution of 4.5 μm and a lateral resolution of 4.4 μm . Recently, a solution using multi-beam OCT was proposed by Michelson Diagnostics Ltd. where five beams are generated using a cuboid prism tilted at a slight angle (Holmes 2008). The first four are used to obtain interference signals and the fifth is used as a reference channel. The beams being focused at 4 different depths because of the tilt angle, give rise to 4 image cross-sections that are slightly displaced with different focused zones of lateral resolution 5.5 μm . The registration and fusion of the in-focus sections has not been discussed.

Drexler *et al.* investigated a related technique to dynamic focusing called zone focusing (Drexler 1999). In this technique, individual layers in depth were imaged, each depth with a new focusing of the beam in that layer. An image fusion technique was then used in which tomograms from different layers were fused to form a 3D data set. This technique, similar to C-mode scanning used in ultrasound imaging, can be considered an alternate form of dynamic focusing, particularly applicable in Fourier Domain OCT (FD-OCT). Three dimensional C-mode OCT imaging was proposed by Huber *et al.* using a high speed, frequency swept 1300 nm source (Huber 2005). Multiple three dimensional data sets were obtained at various focal depths and

fused to overcome the limitations of depth of field imposed by small focus spot sizes needed for high lateral resolution.

Another approach to the problem would be to use non-classical optical elements that would extend the depth of field. One such imaging scheme used an axicon lens first proposed by Ding *et al.* for application in OCT because of the long depth of focus achieved through Bessel beam formation (Ding 2002). Imaging in biological tissue with a lateral resolution of 1.5 μm and a depth of focus of 200 μm were reported. Lee *et al.* demonstrated an axicon-based OCT that offered a larger depth of focus of 2 mm and demonstrated the first 2D images in biological tissue (Lee 2008b). The potential drawback to this technique however, is that it has lower contrast images and therefore may not be well-suited to highly scattering media. Xie *et al.* implemented a GRIN lens rod based probe, also designed for endoscopy that achieved 2.8 mm imaging depth (Xie 2006). However this design still involved moving parts. Another approach proposed by George *et al.* overcame the classical limitations to resolution using a logarithmic lens whose transmission function is derived based on the non-paraxial form of the diffraction integral (George 2003). Experimental results show that the logarithmic lens provides 10 times larger depth of field than an ideal lens of comparable F-number.

In parallel to hardware solutions, there have been alternate attempts to recover the loss in lateral resolution in SD-OCM through rigorous mathematical methods. Ralston *et al.* developed an algorithm called the Interferometric Synthetic Aperture Microscopy (ISAM) to recover invariant 3D resolution across an imaging volume by assuming a linear relationship (first Born approximation for scattering) between the sample susceptibility and the measured OCM signal through a transfer function K (Ralston 2006; Ralston 2007). The transfer function K is modeled

to account for system aberrations, scalar light propagation through the sample, and scattering. ISAM reconstructions of unprocessed interferometric data of breast tissue and their comparison to histology demonstrate potential diagnostic value. Models for other imaging geometries such as rotational (for catheter) and array (for full field) are also being developed (Marks 2006; Marks 2007).

2.4 Motivation

OCT has come into focus in the last two decades because it presents a promising non-invasive solution for the early detection of cancer. In addition, OCT can serve to guide conventional biopsy by more precisely identifying areas to be excised based on images of the epithelial layers thereby reducing the number of biopsies and making earlier and more accurate diagnosis possible. In particular, its application in skin cancer detection is the topic of intense research as skin cancer represents one of the largest causes of death, right next to heart disease. Skin is a highly complex, inhomogeneous, and highly scattering tissue. OCT skin imaging has been found to provide a penetration depth of 2 mm in skin tissue (that includes the epidermis and a part of the dermis), which is amply sufficient for detection of skin cancer cells as has been reviewed in Chapter 1. Research has shown that typical OCT patterns can be distinguished for different sub-surface skin structures and pathological processes. The current challenge posed on OCT imaging is the development of a clinically viable device that provides both high resolution images as well as fast image acquisition rates for a 3D volume of biological sample. In this dissertation, we present the design, analysis, fabrication and testing of one such device, that enables *in vivo* imaging speed at high lateral ($2\ \mu\text{m}$) and axial resolution ($<2\ \mu\text{m}$) through a $2\ \text{mm}^3$ sample volume.

2.5 Research Summary

The purpose of this research is to enable high invariant resolution in an OCM imaging set-up, both axially and laterally in a three dimensional volume of highly scattering tissue such as skin. High axial resolution is achieved through the coherence property of the source, and high lateral resolution is achieved through higher NA than in conventional OCT ($NA \geq 0.1$) combined with dynamic focusing. The challenge lies in the design of the microscope objective with a dynamic focusing element. We present the design and performance of microscopes with two different dynamic focusing elements – the liquid crystal lens and the liquid lens.

The liquid crystal dynamic focusing element was modeled as a special case of the Wood lens i.e., with a radial index gradient, and a variable base index. The immersion microscope objective was designed for a NA of 0.28 and a 10X magnification. Results show that the microscope objective achieves a resolution of $2 \mu\text{m}$ (i.e. maximum frequency is 240 cycles/mm) based on a theoretical prediction of MTF with above 20% at all fields and depths across a 2 mm^3 imaging volume. Preliminary tolerancing analysis of the system indicates a maximum 10% drop in MTF across zoom positions for precision grade tolerances. Results also reveal a less than $2.5 \mu\text{m}$ distortion in all three zoom positions (Murali 2006; Murali 2007a). However, this microscope design did not advance into the prototype design stage because of speed limitations (3 seconds/scan) imposed by the relatively large (3 mm) dimensions of the liquid crystal lens.

A faster technology, namely the liquid lens, was then investigated as an option to evolve into a dynamic focusing microscope prototype by integrating the liquid lens into a custom microscope in a precise, optimized way such that the loss in resolution caused by defocus and the loss of resolution caused by variation in spherical aberration with skin depth as a result of having a

focused beam traveling through a medium with index not equal to 1.0 (Westphal 2002) can in fact be completely compensated for by optical design techniques that leverage the change in conjugate with focal position. The liquid lens operates based on the principle of electro-wetting. Application of voltage favors the wettability of the surface by the conducting liquid and deforms the liquid interface (Berge 2000). Lens diameters of 3 to 4 mm are currently available at Varioptic Inc. with a focal range of 5 cm to infinity, ideal for our requirements. Philips Corporation is also developing liquid lenses (Physorg 2004). Hence, this technology is affordable and is becoming readily available commercially, which is an important necessity to propel a prototype into production for clinical applications.

An early design analysis was first demonstrated by Murali *et al.* to demonstrate feasibility of such a liquid lens based system (Murali 2007b). The voltage controlled liquid lens was built into the design providing real-time focusing, and scanning at the rate of 100 ms/A-scan. The dynamic-focusing microscope operates in immersion in a gel such as glycerol of refractive index 1.45 that approaches the average homogenous refractive index of skin (Diffey 1983; Van Gemert 1989). The final prototype design was later developed to enable optical imaging of approximately a 2 mm³ 3D sample of skin tissue at a predicted invariant resolution of 2 μm laterally and 2.4 μm axially throughout the sample (Murali 2009b). The high lateral resolution is obtained through the custom-design immersion microscope design. The high axial resolution is imposed by the spectrum of a state-of-the-art femtosecond broadband laser source (750 nm-850 nm). Experimental measurements for performance metrics of lateral resolution and depth of focus indicate that the fabricated microscope meets design specifications achieving a resolution of 2 μm.

The microscope was integrated into a Gabor Domain OCM set-up for automatic volume data acquisition, fusion and rendering in biological tissue (Rolland 2008). In the Gabor Domain scheme, an algorithm was used to extract only the in-focus portion of the acquired image, by multiplying the image with a sliding window centered at the focal plane of the microscope and whose width was defined corresponding to the depth of focus. Combining this technique with dynamic focusing allows the extraction of the slices of the cross section image around each focus position, which are then fused to form a quasi-invariant resolution image (Rolland 2009). Sub-cellular imaging is demonstrated in an African frog tadpole (*Xenopus Laevis*) and the different layers are clearly identified in human skin *in vivo* thus presenting further validation of high resolution GD-OCM in scattering media enabled by the dynamic focusing microscope (Murali 2009a).

2.6 Dissertation Outline

The rest of the dissertation is organized as follows:

In Chapter 3, the progression of SD-OCT into a variation of the system suited to dynamic focus imaging, namely Gabor Domain OCM (GD-OCM) is presented. We will then describe the two different design considerations that were explored involving the liquid crystal and liquid lens technology respectively. For each of these design problems, the first-order layout, design analysis, optimization and performance, challenges, advantages and drawbacks are presented.

Chapter 4 first outlines the fabrication process and testing of the liquid lens based microscope. The experimental validation of the predicted MTF function using the edge detection method or line spread function is presented. Resolution measurements when the microscope is

immersed in scattering medium are summarized as well. Finally, imaging at sub-cellular resolution in biological specimens is demonstrated.

In Chapter 5, the primary conclusions derived from this research and its major results and applications will be reviewed. The contribution of this dissertation to OCM research is summarized.

CHAPTER 3- GABOR DOMAIN OCM IMAGING

The technological impasse created in OCM because of the trade-offs between the lateral resolution and depth of focus has paved the way for the development of Gabor Domain OCM (GD-OCM) in our laboratory (Rolland 2008). GD-OCM provides an innovation in optical instrumentation together with a mathematical framework to automatically form 3D image data sets from the high resolution images obtained using the state-of-the-art dynamic focusing microscope developed in this research.

3.1 Gabor Domain Optical Coherence Microscopy

Invariant high resolution imaging of early changes in skin pathology in the epidermis and upper dermis is an important diagnostic step in dermatology. Gabor-Domain is a novel image acquisition and processing scheme that uses dynamic focusing OCM within a spectral domain system. In FD-OCT, conventional sequential axial scanning is used to obtain a 3D dataset with a low NA microscope (i.e., $NA < 0.1$) focused at the center of the sample as shown in Fig. 3.1(a). In the GD-OCM scheme, several 3D datasets are obtained using sequential axial scanning, each dataset having a different focal zone or C-zone as shown in Fig. 3.1(b). The use of a high NA objective lens in the spectral domain leads to clearly distinguish between in-focus and out-of-focus regions of the 3D volume. Imaging techniques similar to C-Mode scanning in ultrasound imaging have been previously proposed to recover the out-of-focus portion of the volume (Sherar 1987; Hill 2004). In the C-mode scanning acoustic microscope (C-SAM), ultrasound

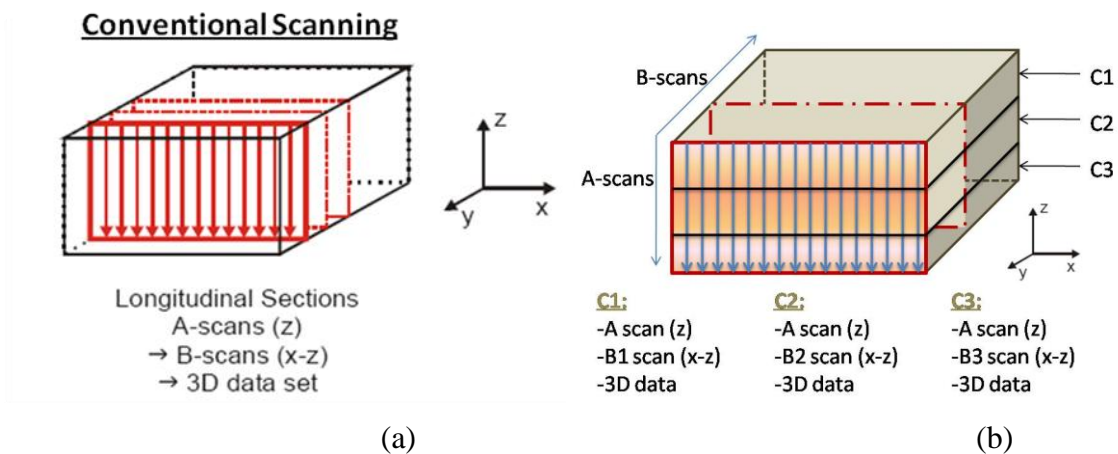


Figure 3.1: Scanning schemes: (a) Conventional OCT scan; (b) GD-OCM scanning

pulses emitted by the transducer were gated in time by physical motion the transducer along the depth axis, so that the resulting images were limited to a particular depth of interest. The C-mode technique was thereafter applied in OCM using manual re-focusing of the objective lens used and all the C-scans were later combined to form the complete depth cross-section (Drexler 1999; Huber 2005). The fusing method however, has not been detailed. In GD-OCM, the focus point of the microscope is changed automatically in depth for every volume and multiple 3D volumes or 2D depth cross-sections are acquired. Thereafter, the in-focus C-zones are identified, sliced and fused without human intervention to achieve faster reconstruction of a uniformly high resolution (lateral and axial) cubic volume of the sample. This imaging scheme is demonstrated in Fig. 3.1(c). Therefore, in a GD-OCM system, two steps are involved: 1) An acquisition scheme using dynamic focusing enabled by an addressable 3D high resolution scanning microscope with no moving parts at *in vivo* speeds, 2) Automatic data fusion of in-focus zones to render volume images of the sample with uniform resolution across depth and fields of view.

3.1.1 Mathematical framework of GD-OCM

GD-OCM uses the dynamic focus OCM microscope in an FD-OCM setup, and employs a newly developed automated algorithm that facilitates the determination and fusing of the in-focus sections or C-zones right after each volume acquisition without human intervention. Consider a typical spectral domain OCM configuration. The spectral intensity as detected by the spectrometer can be modeled as detailed earlier in Eq. 2.13 (Wang 2007). For simplicity, we extract only the 2nd interference term (assuming the other terms can be removed either in software or hardware as discussed earlier), and then remove the mirror/ghost image $r_S(l_R - l_D)$ from Eq. 2.13 and Eq. 2.14. The spectral interference signal can now be expressed by $\hat{I}_{\text{int}}^+(k)$ and $I_{\text{int}}^+(l_D)$ representing the positive side of the detected intensity signal in the spectral and spatial domain respectively, after mirror image removal.

$$\hat{I}_{\text{int}}^+(k) = r_R \cdot \frac{\hat{S}(k)}{2} \int_{-\infty}^{\infty} r_S(l_R + l_D) \exp(ikl_D) dl_D, \text{ and} \quad 3.1$$

$$I_{\text{int}}^+(l_D) = \frac{1}{2} \cdot r_R \cdot \mathfrak{F}^{-1}\{\hat{S}(k)\} * r_S(l_R + l_D),$$

where, $r_S(l_R + l_D)$ represents the sample reflectivity profile as a function of the optical path length difference l_D , and l_R is the constant reference pathlength that simply shifts both the real and mirror signals. It can be surmised from Eq. 3.1 that the sample reflectivity profile along depth can be recovered from the inverse Fourier transform (IFT) of the measured spectral interference signal – a fundamental principle of Fourier Domain OCT (FD-OCT).

Let us now consider the Gabor transform (Barrett 2004), which is simply a sliding window Fourier transform or a local Fourier transform defined by

$$\hat{F}(k; z_0) = \int_{-\infty}^{\infty} g(z - z_0) f(z) \exp(ikz) dz \quad 3.2$$

where, $g(z - z_0)$ is a sliding window function with an arbitrary shape usually chosen to be concentrated around $z = z_0$. The function $g(z - z_0)$ has a finite width, and is always narrower than the function $f(z)$. Therefore, $\hat{F}(k; z_0)$ represents the local frequency components of the function $f(z)$ within the width of the sliding window $g(z - z_0)$. In the spatial domain, the Gabor transform isolates the selected depth section within the sample. Applying Eq. 3.2 to Eq. 3.1, and setting $z_0 = l_G$, the Gabor transform of the interference signal $I_{\text{int}}^+(l_D)$ can now be written as $\hat{I}_G(k; l_G)$.

$$\hat{I}_G(k; l_G) = \int I_{\text{int}}^+(l_D) \cdot g(l_D - l_G) \cdot \exp(ikl_D) dl_D, \quad 3.3$$

where, $l_G = 2n_s l_w$ is a constant that determines the optical shift of the center of the window in the spatial domain, n_s being the refractive index of the sample and l_w the physical shift of the window.

Using the convolution property of the Fourier transform $\mathfrak{F}(f \cdot g) \leftrightarrow \mathfrak{F}(f) * \mathfrak{F}(g)$, $\hat{I}_G(k; l_G)$

$\hat{I}_G(k; l_G)$ can now be expressed as

$$\hat{I}_G(k; l_G) = \mathfrak{F}\{I_{\text{int}}^+(l_D)\} * \mathfrak{F}\{g(l_D - l_G)\} \quad 3.4$$

Using the translation property of the Fourier transform $\mathfrak{F}\{f(t - a)\} \leftrightarrow \hat{F}(\omega) \cdot e^{ia\omega}$, we can arrive the

following expression for $\hat{I}_G(k; l_G)$.

$$\hat{I}_G(k; l_G) = \hat{I}_{\text{int}}^+(k) * [\mathfrak{F}\{g(l_D)\} \cdot \exp(ikl_G)] \quad 3.5$$

If we define a function $\hat{G}(k; l_G) = \mathfrak{F}\{g(l_D)\} \cdot \exp(ikl_G)$, then $\hat{I}_G(k; l_G)$ is now a convolution between the spectral interference $\hat{I}_{\text{int}}^+(k)$ and $\hat{G}(k; l_G)$. Therefore, an inverse Fourier transform of $\hat{I}_G(k; l_G)$ yields a multiplication between the sample reflectivity profile and the sliding window in the spatial domain. This extraction process using a sliding window to obtain the in-focus slice is shown in Fig. 3.2.

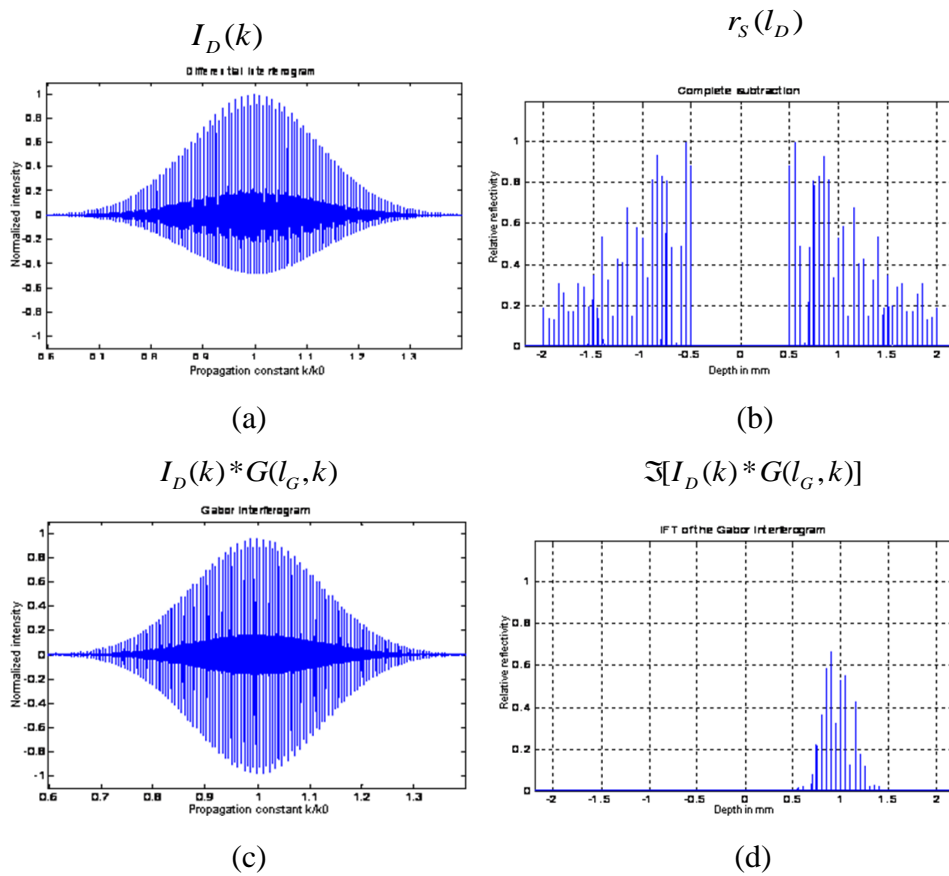


Figure 3.2: (a) Simulated spectra acquired; (b) Its Fourier transform obtained in classical FD-OCM (c) Illustration of the spectral interferogram convolved with a Gabor function, enabling (d) A zone of the reconstructed image to be extracted. The final image sums all automatically registered zones to create a depth focused fused image.

3.1.2 GD-OCM imaging

The interferometer layout used in the GD-OCM imaging scheme using the newly developed dynamic focusing OCM microscope is shown in Fig. 3.3. The dynamic focusing microscope is programmed to automatically refocus at regular intervals and therefore multiple SD-OCM images of the sample are acquired, each obtained with a different focus location. At each focus point, multiple A-scans are completed by supplying a pre-determined input voltage range and increment to the scanning mirror, resulting in a B-scan. Several B-scans are performed spaced by the periodic sampling interval set by the resolution of the microscope. These B-scans when combined yield a 3D volume data set at a single fixed focus point. The focus is then shifted by a distance equal to the depth of focus using the voltage-addressable liquid lens and multiple sample volumes are obtained.

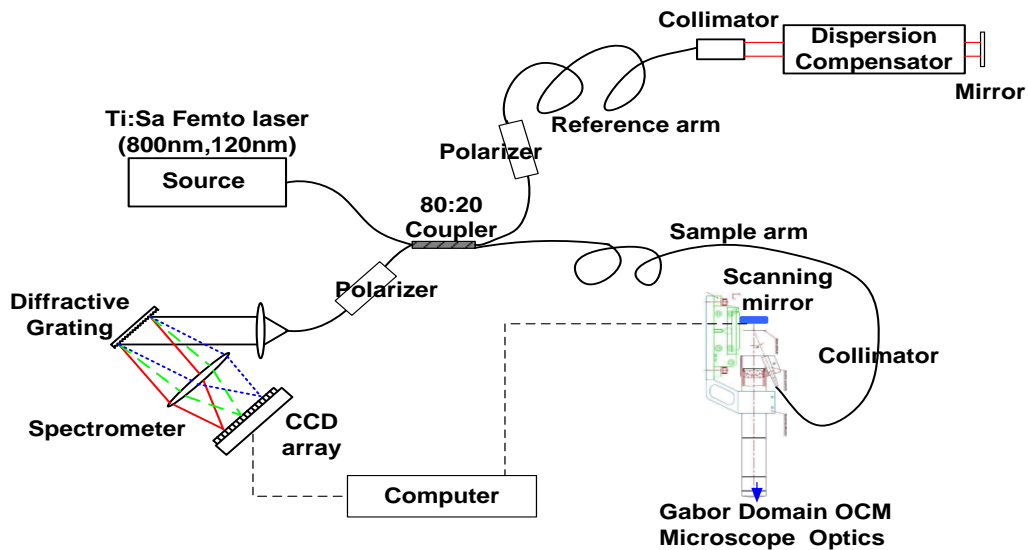


Figure 3.3: GD-OCM experimental layout with dynamic focusing in the sample arm

Next, in order to extract only the in-focus portion of each acquired image volume or cross-section, a depth sliding window whose width is set based on the depth of focus of the dynamic focusing microscope is applied to the GD-OCM images, and the center of the window is shifted to be at the estimated focal plane of the microscope- the estimation method will be detailed in the following paragraph. The cross-sectional images are sliced around each focus position, extracted, and then fused to form a quasi-invariant resolution image. The procedure to extract the in-focus portion is equivalent to an inverse process of the Gabor transformation. This Gabor Domain selective gating process is demonstrated in Fig. 3.4.

Once the volumetric data at different focus voltages is recorded, the next step is to isolate and section the in-focus portions. An algorithm is used to detect the peak or high reflectivity region in the depth profile of each B-scan. A window of width equal to the depth of focus of the microscope is then multiplied with the intensity profile to extract the in-focus section in the Gabor Domain. The shape of the window used is critical since the intensity of the data should not be shaped or altered while at the same time, a smooth transition between sections without any intensity artifacts such as peaks of intensity at the edge of the sections must be ensured. In addition, the sensitivity decreases as we move through the depth of the sample, and therefore the actual image needs to be faithfully reproduced. One such window is a flat-top (to prevent shaping of the data) rectangular function with a linear edge transition. The linear slopes of the window edges between any two sections are set to intersect at the 50% intensity point, thus enabling a smooth transition. The summation of fused B-scans yields an invariant resolution 3D volume.

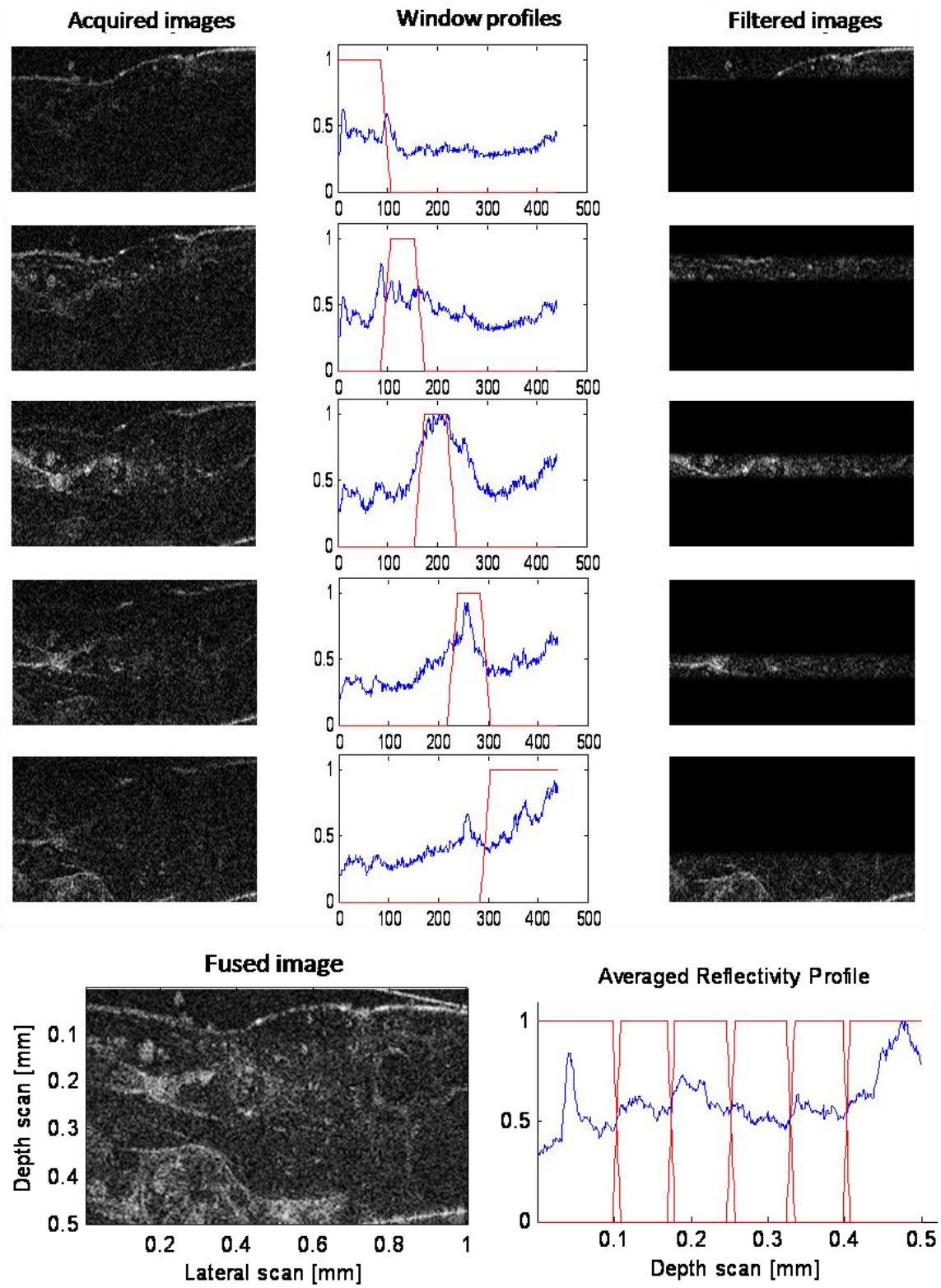


Figure 3.4: Automatic fusing algorithm for GD-OCM

3.2 Optical Design of a Dynamic Focusing Probe for GD-OCM

The most common method for focusing in optical microscopy is through the mechanical motion of the objective lens. This motion limits the speed at which a depth based scan can be accomplished. As an alternative, a variable focus microscope without moving parts can provide a faster, more compact, as well as a cost-effective solution for biomedical systems such as optical coherence microscopes and white light interferometry systems. This microscope can be realized by the incorporation of an adaptive lens within the optical design of the microscope objective where the focus change can be generated through either curvature change or refractive index change within the lens. One such adaptive focus lens is the liquid crystal lens in which a refractive index gradient can be achieved through the application of a voltage gradient (Sato 1979; Ye 2002). The liquid crystal lens can achieve large focal length variation and operate at low voltage, as has been successfully reported (Ren 2006). In this chapter, we will discuss the design and feasibility for two immersion microscopes with built-in dynamic focusing and no

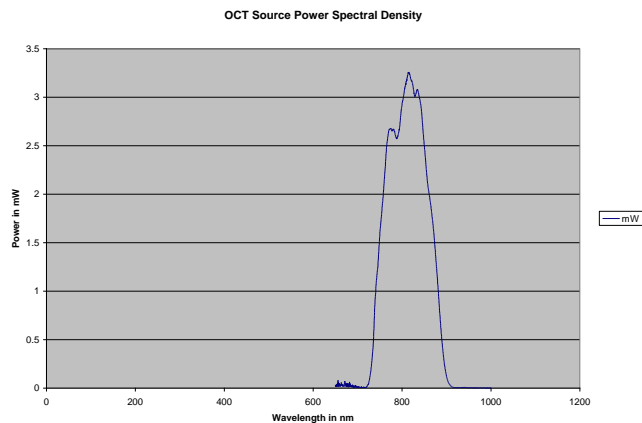


Figure 3.5: Power spectral density for system performance analysis

moving parts, enabled by a liquid crystal lens and a liquid lens respectively. Both microscopes are designed for operation in immersion under illumination by a near-infrared (NIR) source of bandwidth 120 nm shown in Fig. 3.5.

3.2.1 Aberration analysis of a plane parallel plate

Since the primary objective of the variable focus microscope design was to image planes of cells at different depths under the surface of the skin, the first step was to evaluate the theory of how the aberrations of a thin parallel plate would degrade the performance of the system. This analysis of the contribution of the imaging conditions to the optical aberrations with increasing NA of the microscope and thickness of the parallel plate (depth under the skin) can be used to guide the design process to compensate for the estimated aberrations and establish the limiting NA that would be practical under the anticipated conditions of up to 2mm of skin. In order to understand the effects caused by a plane parallel plate that represents the tissue, three summary performance metrics were compared, namely, the RMS wavefront error, the Strehl ratio, and the diameter of image point spread function (PSF) at 50% intensity (Full-Width at Half-Maximum or FWHM) and at 13% intensity (or FW at $1/e^2$). In addition, the dependence of the relevant component aberrations, spherical, coma, astigmatism, and chromatic aberration were investigated. The refractive index and dispersion of the equivalent plane parallel plate were chosen based on actual experimental measurements leading to the determination of the Cauchy coefficients of the dermis of skin tissue in the wavelength range of 300 to 1600 nm (Ding 2006). The aberrations and performance metrics were computed at an NIR wavelength of 1000 nm.

Wave aberrations for a plane parallel plate

A plane parallel plate placed into a collimated space will not affect image quality. When placed in a focusing beam however, aberrations are introduced that are related to the marginal and chief ray angles u (which is proportional to NA) and \bar{u} (which is the field angle induced by the scan mirror) respectively. Fig. 3.6 shows a plane parallel plate of thickness d and refractive index n in the path of a converging beam in air. S_I , S_{II} , S_{III} , and S_{IV} represent the wavefront spherical aberration, coma, astigmatism, and field curvature, respectively. S_V represents distortion, and C_I and C_{II} represent axial and lateral color, respectively. The different Seidel aberrations including chromatic aberrations are also summarized (Welford 1974). It must be mentioned here that the aberrations caused are independent of the height h shown in the figure, thus implying that the placement of the plate in the beam (assuming it is normal to the axis of the system) has no effect on the image point spread function.

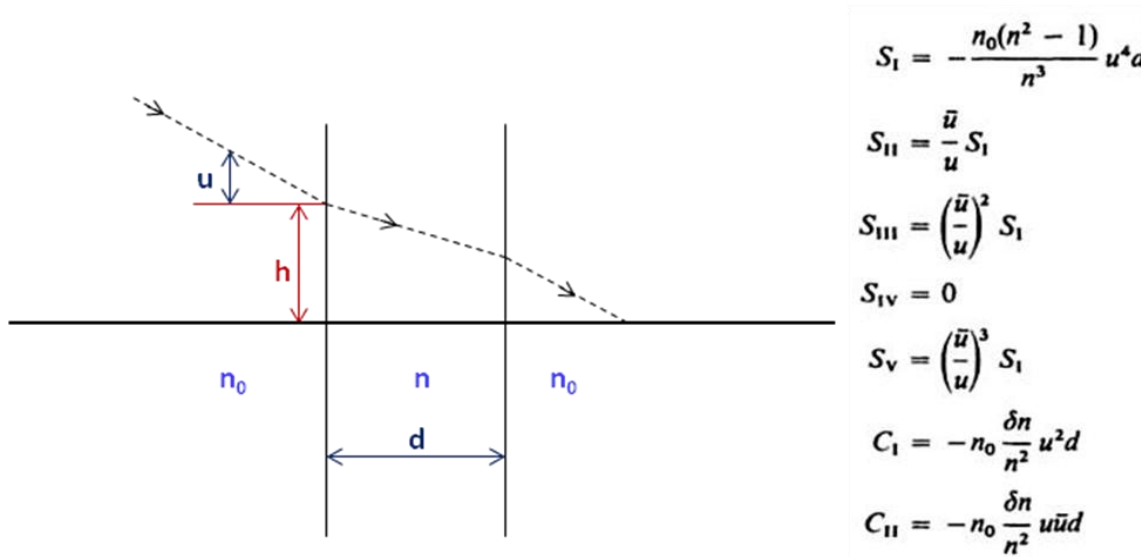


Figure 3.6: Seidel aberrations incurred from a plane parallel plate in the path of a converging beam

The Seidel aberration terms can be directly derived from the wavefront aberrations induced and their relationship is illustrated in Table 5 (Welford 1974). In the remainder of this section, we will use the wavefront aberrations in RMS waves in all the calculations and simulations.

Table 5: The Seidel coefficients and wave aberration coefficient conversions for the primary third order aberrations induced by a plane parallel plate.

	Seidel Coefficient	Conversion Seidel to Wave aberration
Spherical Aberration	$S_I = -\frac{n_0(n^2 - 1)}{n^3}u^4d$	$\frac{1}{8}S_I$
Coma	$S_{II} = \frac{\bar{u}}{u}S_I$	$\frac{1}{2}S_{II}$
Astigmatism	$S_{III} = \left(\frac{\bar{u}}{u}\right)^2 S_I$	$\frac{1}{2}S_{III}$
Field Curvature	$S_{IV} = 0$	$\frac{1}{4}S_{IV}$
Distortion	$S_V = \left(\frac{\bar{u}}{u}\right)^3$	$\frac{1}{2}S_V$
Longitudinal Color	$C_I = -n_0 \frac{\delta n}{n^2}u^2d$	$\frac{1}{2}C_I$
Lateral Color	$C_{II} = n_0 \frac{\delta n}{n^2}u\bar{u}d$	C_{II}

The wavefront aberration in an optical system can be described using the individual third order wave aberrations in units of waves. However, this method is useful in determining the departure of the aberrated wavefront only when a single third order term is present, which is most often not the case. Therefore, RMS wavefront error is used to represent the deviation of the wavefront at

the pupil as a measure of the imaging performance. In practice, an RMS wavefront error of < 0.07 waves is considered ‘diffraction limit’. The RMS wavefront error for a plane parallel plate at the paraxial focus, assuming no tilts and decenters, is given in Eq. 3.6 (Thompson 1980).

$$W_{RMS}^2 = \frac{1}{12} \cdot W_{040}^2 + \frac{1}{180} \cdot W_{040}^2 + \frac{1}{24} \cdot W_{222}^2 + \frac{1}{18} \cdot W_{131}^2 + \frac{1}{72} \cdot W_{131}^2 \quad 3.6$$

The wave aberrations were computed for different NA values ranging from 0.05 to 0.5 and for different thickness between 0 and 2 mm. The \bar{u} was set to 0.175 rad or 10 degrees corresponding to a maximum predicted FOV from the first order layout of the design. Fig. 3.7 summarizes the results obtained showing plots of the different wavefront aberration contributions as a function of NA at selected thicknesses of the sample. It can be surmised from these images that for NA values under 0.2 and thickness up to 2mm the aberration contributions are maintained to

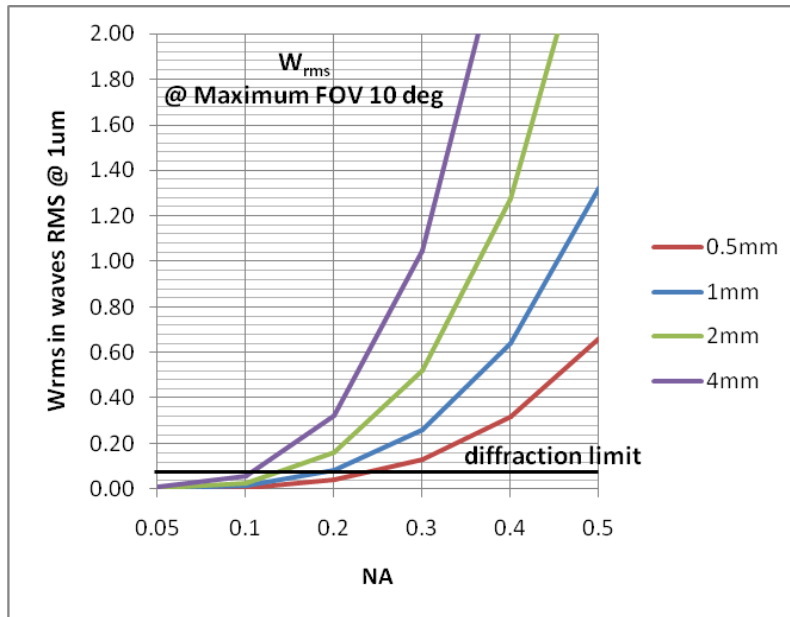


Figure 3.7: RMS Wavefront error at the exit pupil in waves at 1 μm computed in theory from the Seidel values as a function of NA with increasing thickness of the plane parallel plate

approximately less than 1 wave RMS. Beyond an NA of 0.2, coma and spherical aberration exhibit the steepest increase in slope as they vary as the NA to the third power and fourth power respectively.

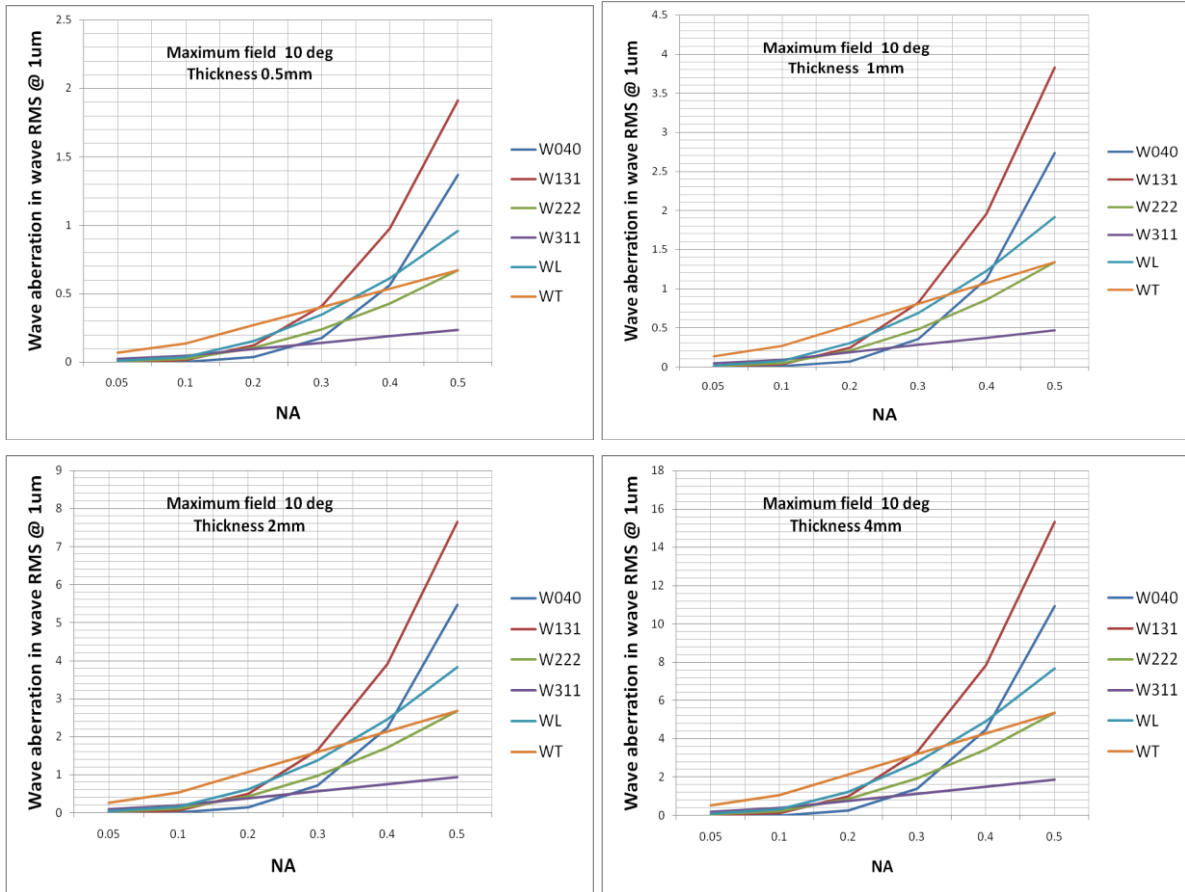


Figure 3.8: Wave aberrations in waves RMS at 1 μm as a function of NA with increasing thickness of the plane parallel plate. Data were computed at the paraxial focus using a marginal ray angle corresponding to the maximum FOV.

Fig. 3.8 shows the RMS wavefront errors as a function of NA and thickness of the plate as computed using the formula in Eq. 3.6. It can be seen that the aberrations induced by the skin cause the system to depart from diffraction limit even at a low NA of 0.2. At a maximum thickness of 2mm and at an NA of 0.2, the RMS wavefront error is still of the order of 1/10 of a wave RMS.

In addition, the spherical wave aberration arising purely from a plane parallel plate of different thicknesses was simulated in software using a stigmatic system in CODEV™. The system comprised of a focusing beam from a parabolic mirror and a plane parallel plate placed in its path on-axis with index coefficients set to simulate the experimentally determined Cauchy model described earlier [Ding 2006]. In CODEV™, we computed the Peak-Valley (P-V) of the wave aberration in the exit pupil without focus and tilt compensation, which is equivalent in the case of spherical aberration to the zero-to-peak value at paraxial focus or W_{040} in waves. The Spherical wave aberration W_{040} in waves at the paraxial focus was then compared with the theoretical values to ensure correctness. The results summarized in Table. 6 show numbers that match to within 1/10th of a wave.

Table 6: Comparison of spherical aberration on-axis computed from theory and software. In CODEV™ an analysis of the fringe Zernike polynomials was used to compute the zero to peak W_{040}

NA	0.05		0.1		0.2		0.3		0.4		0.5	
Thickness (mm)	Theory W_{040}	CodeV W_{040}	Theory W_{040}	CodeV W_{040}	Theory W_{040}	CodeV W_{040}	Theory W_{040}	CodeV W_{040}	Theory W_{040}	CodeV W_{040}	Theory W_{040}	CodeV W_{040}
0.5	0.000	0.000	0.002	0.002	0.035	0.034	0.177	0.170	0.560	0.528	1.367	1.264
1	0.000	0.000	0.004	0.004	0.070	0.068	0.354	0.340	1.120	1.057	2.733	2.529
2	0.001	0.001	0.009	0.009	0.140	0.136	0.708	0.680	2.239	2.115	5.466	5.062
4	0.001	0.001	0.017	0.017	0.280	0.272	1.417	1.361	4.478	4.236	10.933	10.143

Strehl Ratio

The Strehl ratio is one of the most commonly used metrics in optical systems to gauge the effect of wavefront aberrations on image quality. It is simply the ratio of the peak diffraction intensities

of the ideal reference wavefront to the peak intensity of an aberrated wavefront. The Strehl ratio is directly related to the RMS wavefront error for small amounts of aberration near the diffraction limit with respect to the reference wavefront and is given by the following expression (Mahajan 2004)

$$SR = e^{-(2\pi W_{RMS})^2} \quad 3.7$$

The approximation in Eq. 3.7 is accurate for RMS wavefront errors up to the order of 1/10 of a wave and can still be utilized for Strehl values of up to 0.3. The difference between the estimated Strehl ratio and exact Strehl value gradually increases with the RMS wavefront error, but even at a value approaching 0.3, this difference still doesn't exceed 10%. A Strehl ratio equal or greater than 0.8 indicates a diffraction-limited system. Fig. 3.9 plots the Strehl ratio obtained for different glass plate thicknesses as a function of increasing NA. It can be observed that at a

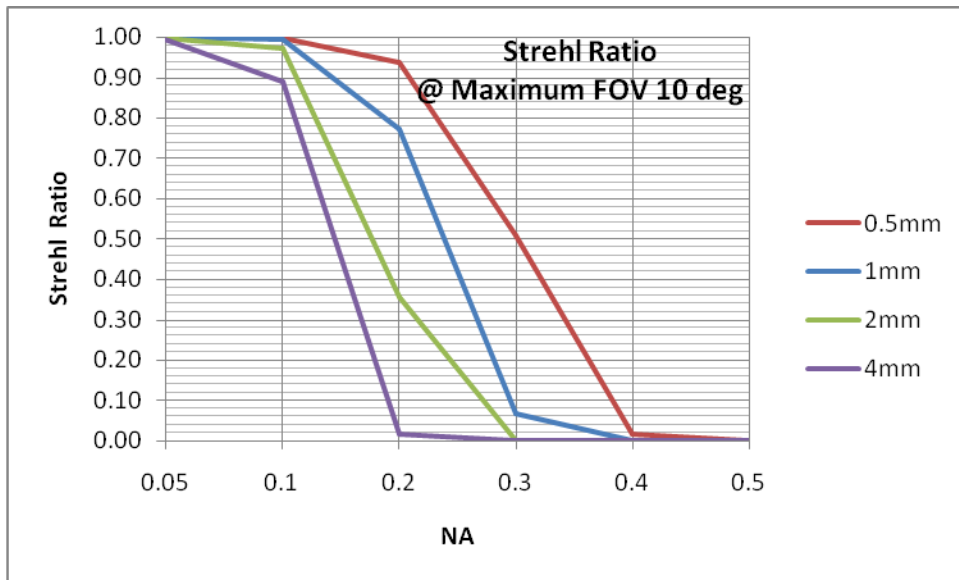


Figure 3.9: Strehl ratio vs. NA with increasing thickness of the plane parallel plate.

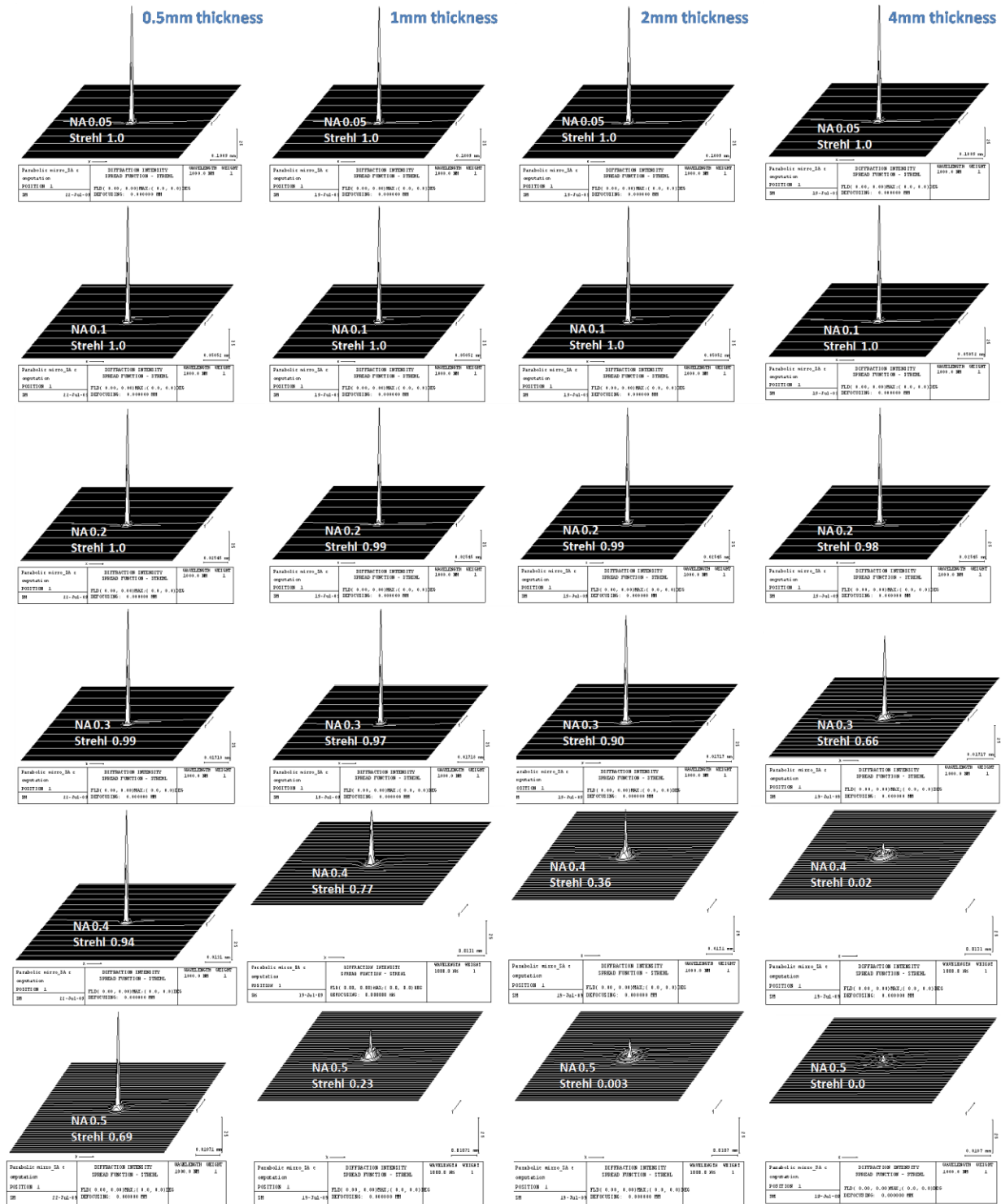


Figure 3.10: PSF and Strehl ratio generated in CODEV™ at various NA (increasing from top to bottom) and thicknesses (increasing from left to right).

thickness of 1mm and an NA of 0.2 the Strehl ratio drops to just below the criterion for a diffraction limited system of 0.8, highlighting the need for compensation in optical system design starting just below and NA of 0.2.

The Strehl ratio drops dramatically with NA as the thickness of skin increases. This effect is further demonstrated in Fig. 3.10 where the PSFs simulated at various NA and thickness values in CODEV™ are shown. The same lens system comprising of an on-axis plane parallel plate in the path of a focusing beam described was modeled for this simulation.

Full Width Half Maximum of PSF

The FWHM of the image point spread function is sometimes used as a metric for establishing the resolution of the optics. While this function has its merits in a diffraction-limited system, it can no longer meaningfully characterize the intensity distribution on the image plane for aberrated wavefronts. Additionally, this definition for resolution becomes irrelevant in low power, low SNR systems since it becomes difficult to isolate the weak signal near the noise floor leading to image degradation. Thus resolution and contrast are both important parameters that affect imaging performance. Even if a small FWHM is obtained, if the Strehl ratio is small, high resolution structures cannot be resolved

The data in Table 7 highlights one of the reasons FWHM is not a good metric for OCM. Here, in addition to tabulating the FWHM of the PSF, the PSF full width at $1/e^2$ intensity is reported. All these numbers were simulated on-axis using CODEV™. As can be seen, even though all of the previous metrics and the full width at $1/e^2$ metric show a degradation in performance, the FWHM number remains essentially unchanged. The only condition that would be appropriate for this

metric is where there are high contrast image features and where thresholding of the detector at energies as high as 30% is used to eliminate the effects of the energy that has transferred out of the peak of the PSF and into the rings of the Airy disc pattern.

It was concluded from this theoretical analysis and supporting CODEV™ simulation that in going forward with the variable focus microscope design, it is highly advantageous and enabling to take into account the drop in Strehl ratio with depth and compensate within the optical design with the goal of maintaining a value of at least 0.8 overall across the depth of the skin to be imaged. This was particularly significant for our application since a low power source was to be used in the OCM interferometer and the signal would be further weakened by backscattering. In addition, it was determined that an NA of 0.2 would be sufficient to achieve our lateral resolution goal ($< 5 \mu\text{m}$) since it would enable a diffraction limited resolution of $2.4 \mu\text{m}$. Since it was surmised from the above analysis that the aberrations start to substantially degrade performance relative to diffraction-limit at an NA of approximately 0.2 at the skin depths of interest, these would also need to be addressed in the optical design process

Table 7: Strehl ratio, wavefront error (both P-V and RMS in waves at 1 μm), and the PSF FWHM and FW at $1/e^2$ of maximum intensity simulated in CODEVTM on-axis for different NA and plate thickness.

0.5mm thickness

NA	SR	PV (waves)	Wrms (waves)	FWHM (μm)	FW@13.5% (μm)
0.05	1	0	0	10.32	16.49
0.1	1	0.001	0	5.16	8.26
0.2	1	0.009	0.003	2.60	4.16
0.3	0.993	0.043	0.013	1.75	2.80
0.4	0.938	0.135	0.04	1.33	2.13
0.5	0.689	0.328	0.097	1.08	1.73

1mm thickness

NA	SR	PV (waves)	Wrms (waves)	FWHM (μm)	FW@13.5% (μm)
0.05	1	0	0	10.32	16.49
0.1	1	0.001	0	5.16	8.26
0.2	0.999	0.017	0.005	2.60	4.16
0.3	0.974	0.086	0.026	1.75	2.80
0.4	0.774	0.27	0.08	1.33	2.84
0.5	0.225	0.657	0.195	1.06	4.68

2mm thickness

NA	SR	PV (waves)	Wrms (waves)	FWHM (μm)	FW@13.5% (μm)
0.05	1	0	0	10.32	16.49
0.1	1	0.002	0.001	5.16	8.26
0.2	0.996	0.034	0.01	2.60	4.16
0.3	0.901	0.173	0.051	1.75	2.80
0.4	0.358	0.54	0.161	1.32	5.19
0.5	0.003	1.314	0.39	1.07	1.69

4mm thickness

NA	SR	PV (waves)	Wrms (waves)	FWHM (μm)	FW@13.5% (μm)
0.05	1	0	0	10.30	16.49
0.1	1	0.004	0.001	5.16	8.26
0.2	0.984	0.069	0.02	2.60	4.16
0.3	0.658	0.345	0.102	1.74	2.79
0.4	0.016	1.081	0.322	1.29	9.18
0.5	0	2.631	0.781	1.08	9.05

3.2.2 Liquid crystal lens based microscope objective

The objective of the design process was to model a 10X immersion refractive microscope objective with an NA of 0.2 or higher and $< 5 \mu\text{m}$ lateral resolution. An immersion oil/gel was chosen that has optimum transmission at 800 nm and closely matches the index of skin. A commercially available gel from the Cargille Labs was used in the modeling. It has a refractive index of 1.46 with 99% transmittance in the NIR spectral band.

A starting point lens model was imported from LensView that was designed to work in immersion. It had an NA of 1 made possible through a meniscus lens in the front and worked at a FOV of 7 degrees. A new material was defined in the lens catalog to represent the immersion medium. A flat glass plate was inserted as the last surface to enable contact imaging. The system was then optimized to obtain a resolution of $< 5 \mu\text{m}$. At this feasibility phase of the research, we did not attempt to reduce the number of elements to a minimum. The purpose was rather to analyze if the design could meet performance specifications. After the desired resolution was obtained, glasses were fitted lens by lens within the specified glass map boundaries. The optimal fixed-focus lens system was finalized with an excellent resolution of less than $5 \mu\text{m}$. The preliminary lens MTF is shown in Fig. 3.11. The image of this system is diffraction limited i.e., the MTF at 100 cycles/mm (corresponds to $5 \mu\text{m}$ spatial resolution).

Next, the system needed to be extended to image up to a depth of 2 mm in tissue. So, the next step was to incorporate zoom positions in the system in order to enable the evaluation of image quality at different focus positions. Three zoom positions were added, at 0, 1 and 2 mm depth of tissue that corresponded to three image planes separated by a distance of 1 mm. A glass plate was added as the last element of the system, closest to the immersion gel and sample to represent

a liquid crystal lens. The position of the liquid crystal lens was chosen to minimize the diameter of the lens required to accommodate the incoming beam. At each zoom position the refractive index of the glass plate was set as an independent variable parameter. The radii of curvature of the two surfaces of the lens were set to vary similarly across all zoom positions. By optimizing the design, the refractive indices of the three lenses needed to focus at these depths were obtained ($n=1.481$ at zoom=0 mm; $n=1.609$ at zoom=1 mm; $n=1.734$ at zoom=2 mm). These were the starting parameters for the modeling of a liquid crystal dynamic focusing element that would change its refractive index gradient in order to refocus axially across 2 mm.

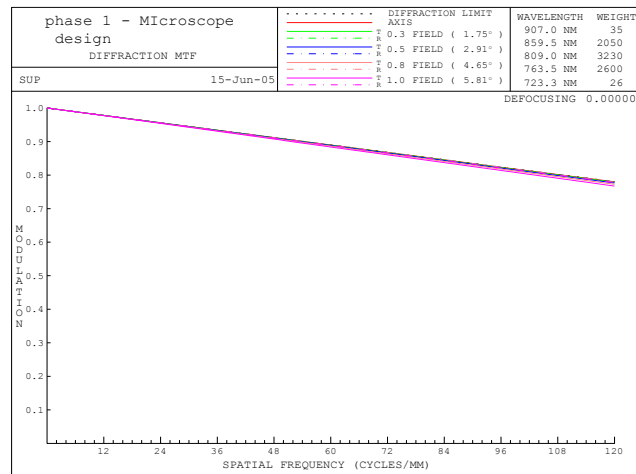


Figure 3.11: Preliminary design MTF at 100 cycles/mm corresponding to 5 μm resolution.

Liquid crystal lens model

The liquid crystal refractive index may be varied as a function of position by adjusting the birefringence properties of the material. The birefringence is given by

$$\Delta n = n_e - n_o = \frac{r^2}{2df} \quad 3.8$$

where r is the radius of the lens, d is the cell gap, f is the focal length, and Δn is the birefringence of the material. A liquid crystal can be modeled to function as a lens if the electric field is varied as a function of the radial distance from the center in order to approach the OPD of a lens of constant refractive index as demonstrated in Fig. 3.12. Thus, a constant optical path difference can be maintained by varying either the curvature or the refractive index.

The Gradient Index (GRIN) profile in a lens element can be specified by a double power series that depends on the spatial coordinates in the element:

$$n(r, z) = n_{00} + n_{01}z + n_{02}z^2 + n_{03}z^3 + n_{04}z^4 + n_{10}r^2 + n_{20}r^4 + n_{30}r^6 + n_{40}r^8 \quad 3.9$$

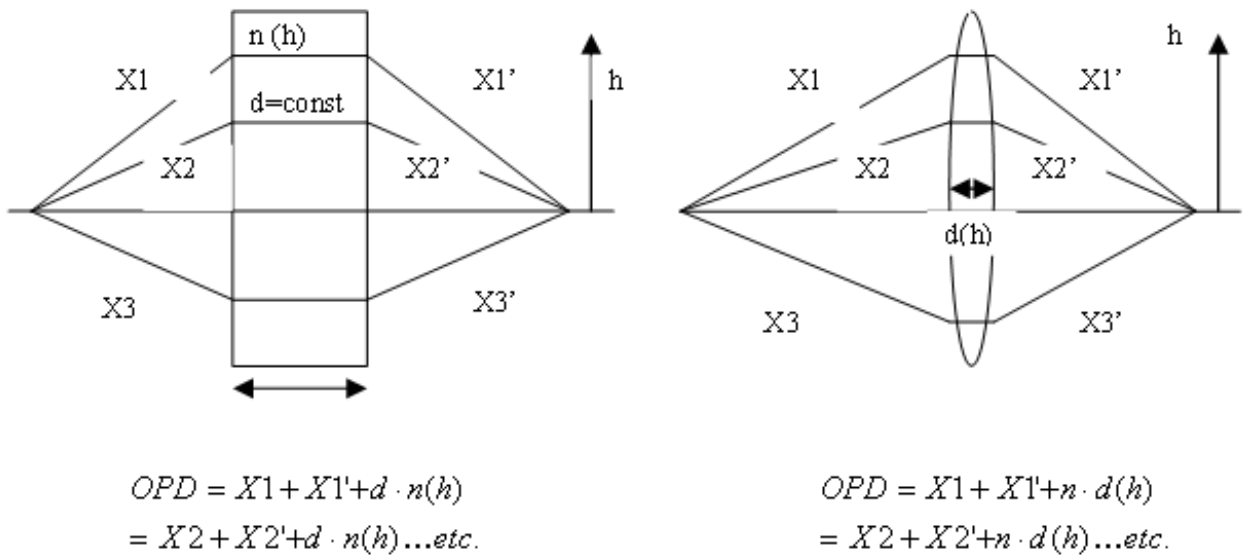


Figure 3.12: Working of a gradient index lens

where, n is the index at some point in the lens, n_{00} is the base index of the lens, n_{0i} and n_{0j} are coefficients of the index gradient, and r is the radial distance in the aperture where the index is evaluated ($r^2 = x^2 + y^2$). When the index of refraction depends only on the distance from the optical axis r , the gradient is said to be radial. Its representation simplifies to

$$n(r) = n_{00} + n_{10}r^2 + n_{20}r^4 + \dots \quad 3.10$$

The coefficients of the radial index gradient contribute in several ways to the design; n_{00} is the index of the base glass, which is the index specified in a homogeneous design, n_{10} contributes to the power of a thin Wood lens and to the Petzval field curvature due to the gradient, n_{20} has no effect on the Petzval curvature and can thus be used to correct other aberrations without affecting the Petzval curvature (Atkinson 1982).

Design results

A gradient index lens was substituted in place of an initially fixed focus lens of homogeneous refractive index positioned before the contact glass plate. A radial gradient index lens was specified in CODEVTM with a custom glass property as defined above in Eq.3.10. This simulates what is known as a Wood lens and can be used to model the mechanism of the liquid crystal lens (Atkinson 1982). The radial coefficients were then coupled to vary simultaneously over all zoom positions, while the base index was optimized independently over each zoom position. The system was then optimized to achieve a resolution of less than 2 μm . The first order data for the optimized dynamic focusing microscope objective are summarized in Table 8 (all units are in mm). The lens layout, and the MTF plots are given as a function of the zoom/focus position in

Fig. 3.13 and Fig. 3.14. The MTF falls well above 20% for the required spatial frequency of 250 cycles/mm, thus giving a resolution of 2 μm .

Table 8: First order parameters of the liquid crystal lens based microscope when focused at 0 mm, 1 mm and 2 mm from the surface of the sample (all units in mm)

	Image Distance	0 mm	1 mm	2 mm
INFINITE CONJUGATES	EFL	10.13	11.64	11.92
	BFL	1.08	1.73	2.68
	FFL	10.61	6.69	6.61
	FNO	1.73	1.65	1.65
AT USED CONJUGATES	RED	0.08	0.1	0.10
	FNO	1.79	1.79	1.79
	OBJ DIS	73.49	73.49	73.49
	TT	133	134	135
	IMG DIS	1.89	2.89	3.89
	OAL	57.63	57.63	57.63
PARAXIAL IMAGE	HT	1	1	1
	THI	1.92	2.90	3.90
	ANG	7.96	6.60	6.44
ENTRANCE PUPIL	DIA	4.03	4.86	4.98
	THI	13.2	13.2	13.2
EXIT PUPIL	DIA	10.8	5.97	6.20
	THI	26.12	12.58	12.18
	STO DIA	6.27	7.61	7.82

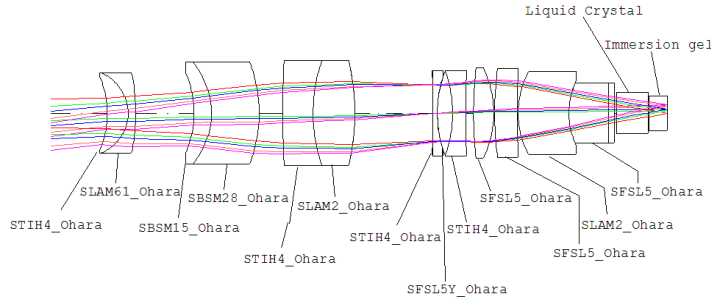


Figure 3.13: Liquid crystal based microscope objective – lens layout when focused at the surface of the sample (0 mm depth)

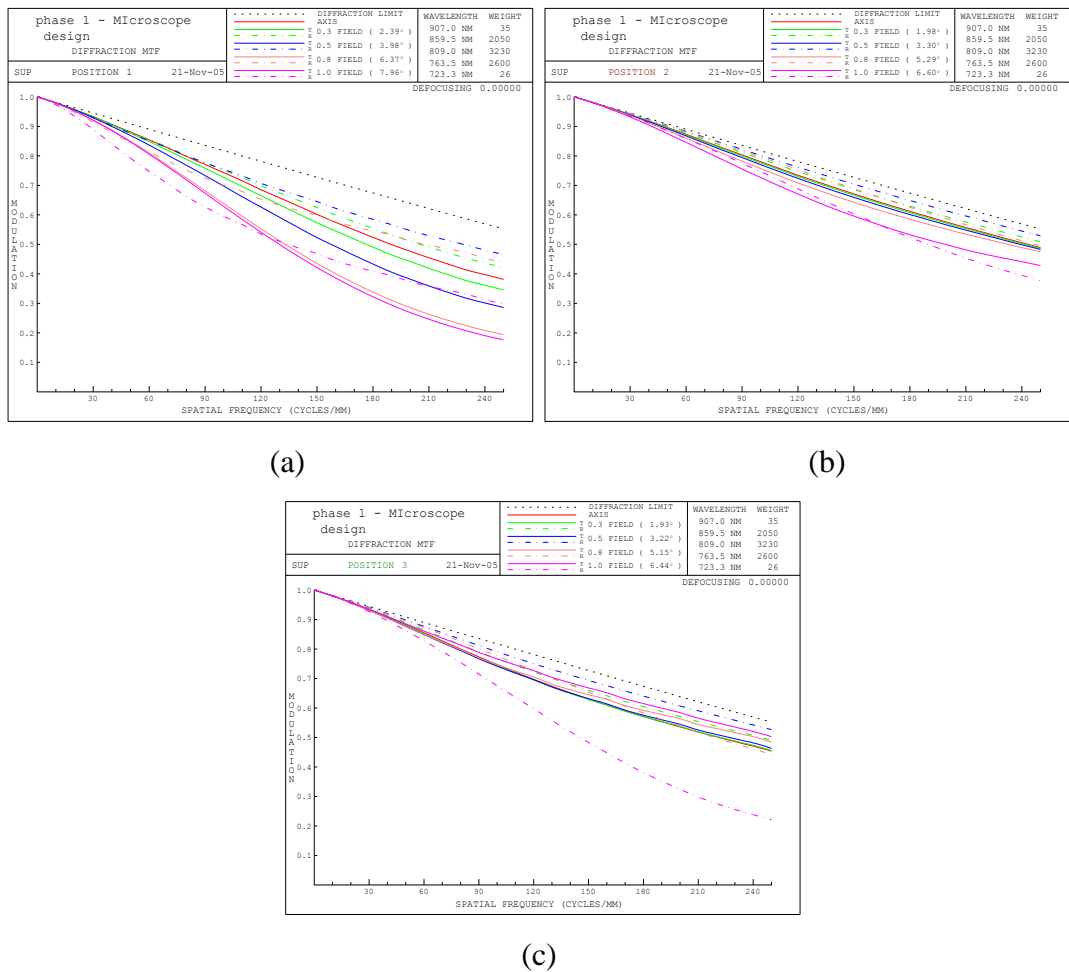


Figure 3.14: MTF of the liquid crystal based dynamic focusing microscope objective obtained at (a) 0 mm focus; (b) 1 mm focus; (c) 2 mm focus

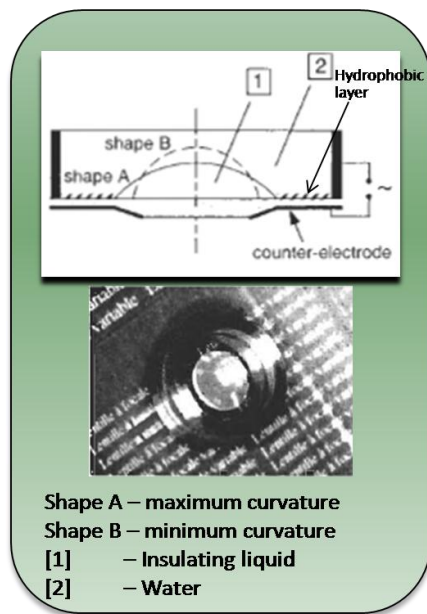
This system has one primary limitation– the speed of the liquid crystal lens. Scanning the 2mm×2mm sample at video rate (30 frames/sec) with a lateral sampling of 1 μm and re-focusing in discrete steps every 50 μm requires a depth scan approximately every 10 milliseconds. In our design, we require an LC of approximately 3 mm diameter. The time estimate for dynamically refocusing this lens would be 0.5-1 second, which is several orders of magnitude slower than necessary for imaging at video rate. Since this design cannot offer sufficient speeds, it did not proceed to prototyping, wherein the number of elements would have been significantly reduced, and the glass map boundary would have been defined to meet low cost and robustness requirements.

3.2.3 Liquid lens based microscope objective

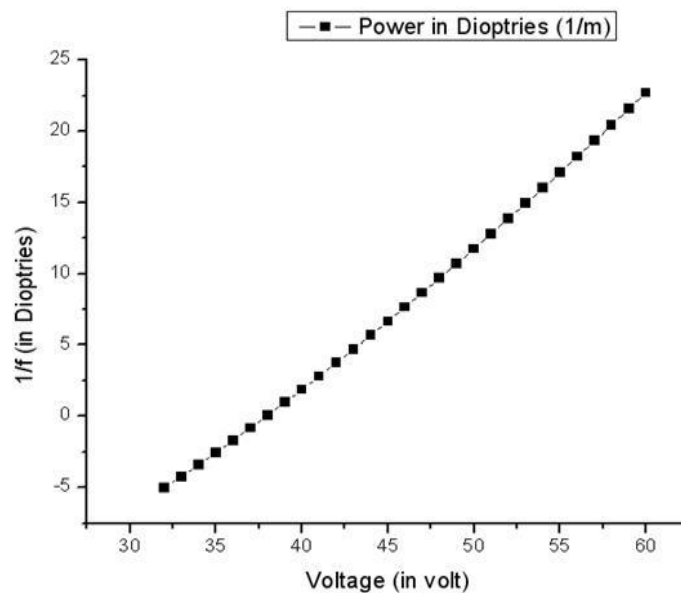
A liquid lens is another effective solution to the problem of a variable-focus lens without mechanically moving parts. It offers the advantage of higher speed and diameter (~3 mm, in our case) when compared to the liquid crystal lens. In addition, adaptive liquid lenses also provide higher quality performance, do not require polarized light, and are therefore being extensively researched today (Ren 2006). Liquid lenses can be driven through two different operating mechanisms that result in a change in the curvature of the lens. One method is through electro-wetting, where the meniscus formed by two immiscible liquids is controlled through the application of voltage (Berge 2000; Krupenkin 2003; Kuiper 2004c). The other method is through mechanical control of the curvature of the lens (Knollman 1971; Zhang 2003; Moran 2006; Ren 2006). To-date the best resolution achieved using adaptive lenses of aperture size less than 5 mm approaches 25 lp/mm (Wu 2007).

Electro-wetting liquid lens

This research uses the electro-wetting based liquid lens in order to allow dynamic control with no mechanical motion. Electro-wetting typically involves changing the shape of a liquid drop on a substrate by the modification of the contact angle of the drop (Berge 2000). Two immiscible, isodensity liquids of different refractive index such as water and oil are placed in contact with each other forming an interface between them. One is insulating and non-polar, the other is a conducting solution. The same density is required to prevent distortion of the shape due to gravity at the liquid-liquid interface. The insulating liquid is in the form of a drop placed on a thin hydrophobic insulating window to trap the liquid (shown hatched in Figure 3.10(a). The



(a)



(b)

Figure 3.15: Electro-wetting based liquid lens. (a) Focus mechanism; (b) Power of the liquid lens as a function of the voltage applied:

exterior surface of the entire window is coated with a transparent electrode called the counter-electrode. Application of voltage between the counter-electrode and the conducting liquid favors the wettability of the substrate by the conducting liquid and deforms the liquid-liquid interface from shape A to shape B. Varioptic Inc. is a liquid lens company that has pioneered electro-wetting based variable focal length lenses and is at the forefront of advances in this field. They have demonstrated such an electro-wetting based liquid lens of diameter 3 mm (Arctic 320) for phone camera lenses with a focal range of 5 cm to infinity that facilitated this research.

Starting Point for the dynamic focusing 3D microscope

It was determined that the starting point for the dynamic focusing 3D microscope should be a fixed-focus, high resolution Lister microscope configuration. The Lister microscope provides an ideal starting point as it provides high resolution at shorter working distances for systems with an NA of up to 0.3. Microscopes typically have an aplanatic-concentric meniscus shaped lens in front of the system to ensure high NA, while at the same time minimizing spherical aberrations where the rays bend the most. However, off-axis aberrations such as coma and astigmatism will arise from the lens. Fig. 3.16(a) shows the optical layout of the starting point design configuration of the fixed-focus Lister microscope. The design achieved an NA of 0.65 for an FOV of 0.25 mm. It also achieved greater than 20% contrast in MTF at 450 lp/mm that corresponds to a resolution of 1.1 μm . Since our goal was to operate in immersion, we required very short working distances and therefore, a low-medium range NA of less than 0.3 was determined to be adequate to achieve a lateral resolution of less than 5 μm , as inferred from cell morphology in Chapter 2. Therefore, following the preliminary fixed-focus Lister design, the source spectral properties were included to enable function in an NIR broadband spectrum of

bandwidth 120 nm centered at 800 nm acquired from a Ti:Sa femtosecond pulsed laser source shown earlier in Fig. 3.5. A BK7 glass plate was placed in front of the lens system to allow for immersion and contact imaging. The fixed lens system was then optimized for a high resolution 2 μm . Fig.3.11 shows the fixed-focus NIR Lister-type microscope with NA 0.25 and a magnification of 10X. This system was optimized for greater than 20% contrast MTF at 250 lp/mm over a 2mm \times 2mm FOV at a given point in depth.

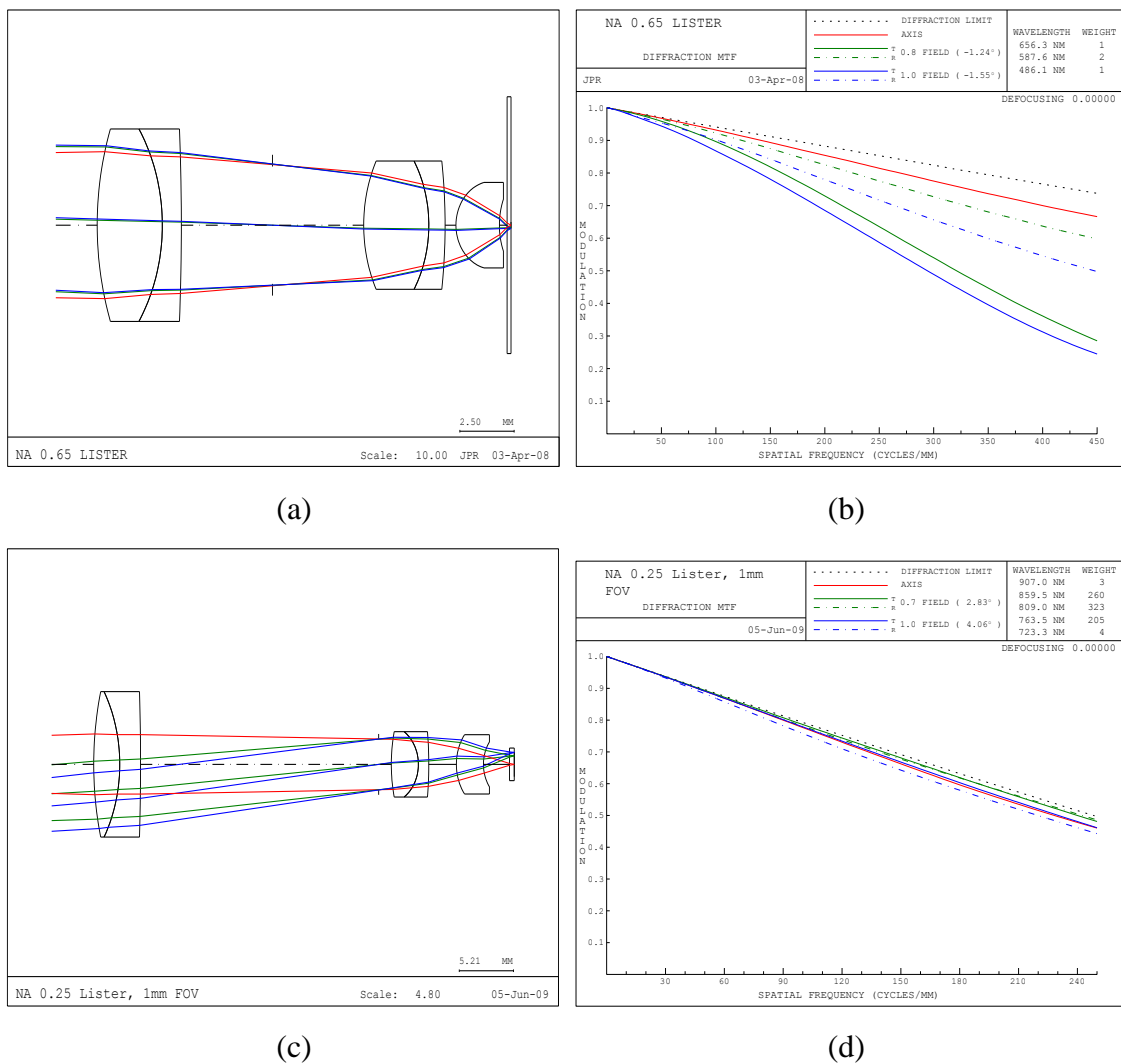


Figure 3.16: (a) Lister microscope 0.65NA with (b) MTF > 20% at 450lp/mm ; (c) NA 0.25 NIR Lister with (d) MTF >20% at 250 lp/mm

Optical design and theoretical performance

The variable-focus configuration was set-up into the fixed-focus optimized Lister microscope by creating three zoom positions representing three different imaging planes in depth located at 0 mm, 1 mm and 2 mm. In each zoom position, all liquid lens parameters were frozen except for the liquid-liquid interface curvature and the thickness of the liquids along the optical axis. The overall thickness (sum) of the liquids was constrained to be constant along the optical axis. The imaging space was now immersed in a homogeneous medium of refractive index 1.45 defined in the user material catalog of CODE V. This refractive index was chosen to approach the mean index of skin. Immersion was used to not only prevent aberrations caused by a converging beam in air focusing into a parallel plate of significantly higher index, but also allows greater depth since it prevented loss of light/contrast caused by the high scattering arising from the tissue surface because of the roughness or irregularity of the surface. The liquid lens in this design was placed at the aperture stop of the system in between the two doublets in order to minimize the spherical aberration contribution from the lens. The last element of the microscope was a flat glass plate to allow for contact imaging in immersion. Constraints were placed in the optimization according to the specifications as laid out in Table 9. Circular aperture diameters of each surface of the liquid lens were fixed and the starting point curvatures for each zoom position were input based on first order calculations. Glass map boundaries were defined for the lens materials such that a large range of index and high Abbe numbers were encompassed in order to allow for effective chromatic correction. The design was then converged to a 10X microscope objective with a lateral field of view of 2mm×2mm and a simultaneously minimized spot size at the three image positions.

Table 9: Microscope design specifications

	GOALS	ACHIEVED
Microscope type	Immersion	Immersion
Immersion medium refractive index	~1.4	Glycerol (n=1.45)
Operating Spectrum (nm)	750-850	760-860; Weighted as 859.5nm-260, 809nm-323,763.5nm-205
Lateral Resolution (μm) MTF criteria $\geq 20\%$ contrast at 250 lp/mm	< 5	2
NA	0.2	0.2
FOV (mm)	2×2	2×2
Working Range(mm)	0-2	0-2
Magnification	10X	10X
Outer Diameter(cm)	< 5 (handheld)	3.1

A scanning lens was added to the microscope objective configuration in order to render the beam telecentric in the object plane. The incoming collimated beam was coupled into the microscope and scanned along the lateral direction using a single or dual axis scanning. The scan lens was modeled to be a simple doublet and the mirror was modeled to be a 2 mm×2 mm square aperture placed at the entrance pupil. A Gaussian apodization of I_0/e^2 was applied at the edge of the entrance pupil to simulate the property of the incoming laser beam. The microscope system was then further optimized to compensate for residual optical aberrations and dispersion within the system including the wavefront errors from the liquid lens according to its theoretical model provided by the lens manufacturer and the aberration caused by the increasing optical path of the focused beam in the skin. Thereafter, glass fitting was carried out to fit industrial glass to the optimized index parameters in the design. The objective was to minimize the number of glasses used, while at the same time preserve the resolution and dispersion correction of the system. Additionally, the glass melt frequency, price range, and the tolerance to handling during the

manufacturing process were taken into account in arriving at the final choice of the glass materials used.

Fig. 3.17(a) shows the optical model of the final prototype design. Fig. 3.17(b) plots the microscope image distance and the liquid lens curvature as they change through the depth range of the sample, namely 0 mm to 2 mm. In addition it also shows the corresponding linear best fit curve. The actual change in curvature of the liquid lens at the 0, 1 and 2 mm imaging distances of the microscope are demonstrated in Fig. 3.17(c), extending from negative to positive focal

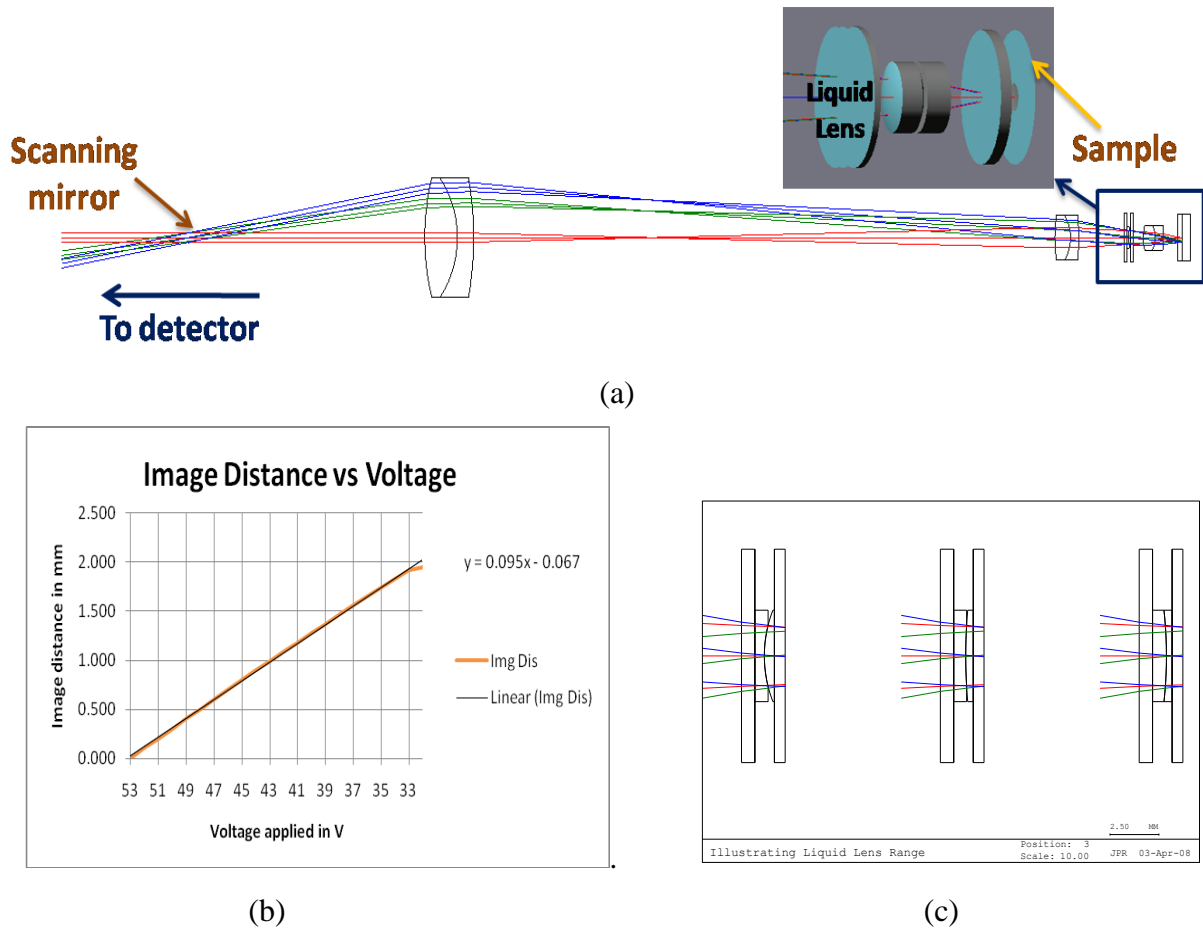


Figure 3.17: Final design of liquid lens based dynamic focusing immersion microscope. (a) Optical layout; (b) Image plane position vs. voltage applied; (c) Change in liquid lens curvature across three focal positions through the working depth range

powers. The focal range of the liquid lens alone is varied from 6 mm to -20 mm in order to achieve the 2 mm working depth range. The dynamic focusing imaging probe is designed to image in 3D at a lateral resolution of 2 μm across a 2 mm³ imaging volume. The axial resolution when used in a broadband low-coherence interferometric set-up is determined by the coherence length of the source, in this case 2.4 μm in air and 1.8 μm in skin-equivalent tissue.

The first order parameters of the final optical system design are summarized in Table 10. The overall length of the microscope is approximately 25 cm, the diameter is 4 cm, and net weight is estimated to be 21 g without the mechanical components, thus allowing it to be handheld and portable. Since the focal length of the liquid length is changed in order to achieve varied image depth, the magnification and F-number also differ across different image planes. An average F-number of 2.8 and a magnification of 8X was achieved.

Table 10: First order parameters of the liquid lens based microscope (all units are in mm)

	Image Distance	0 mm	1 mm	2 mm
INFINITE CONJUGATES	EFL	-5.57	-5.89	-6.14
	BFL	0.02	0.01	0.00
	FFL	0.12	-0.01	-0.12
	FNO	-2.79	-2.94	-3.07
	OAL	249.7	250.8	251.6
AT USED CONJUGATES	RED	0.12	0.12	0.13
	FNO	2.66	2.81	2.93
PARAXIAL IMAGE	HT	0.98	1.04	1.08
	ANG	10	10	10
ENTRANCE PUPIL	DIA	2	2	2
	THI	5.85	5.85	5.85
EXIT PUPIL	DIA	1.94	2.01	2.06
	THI	-5.40	-5.91	-6.31
	STO DIA	2	2	2

The third and higher order aberration contributions from each surface as we move from element to element of the microscope when it is focused at the center of the sample, i.e. 1mm in depth, are laid out in Fig. 3.18. It must be emphasized that the system design is diffraction-limited with an RMS wavefront error of less than 0.07 waves. Therefore, these plots show the role of the various elements towards balancing the correction of the different residual aberrations. Distortion is less than 4% and in all cases, and is not a fringe degrading aberration. Therefore, it can be calibrated and corrected during post-processing. The remaining third order aberrations, namely spherical aberration, coma, field curvature and astigmatism are found to be approximately less than 2 waves. The higher order aberrations come into play to balance these residual third order aberrations, resulting in a diffraction limited system. Fig. 3.19 shows the net significant ($\lambda/10$ or higher) third and higher order aberrations at three different focus positions of the microscope. Higher order spherical aberrations (W_{060} and W_{080}) have been excluded in these plots as their values were of the order of $\lambda/50$. The axial and lateral color due to dispersion in the immersive medium was also computed. It was found that the system is well corrected for dispersion with a longitudinal axial color of $3.2 \mu\text{m}$ that translates to $1.28 \mu\text{m}$ of transverse blur, and a lateral color of $0.07 \mu\text{m}$ respectively.

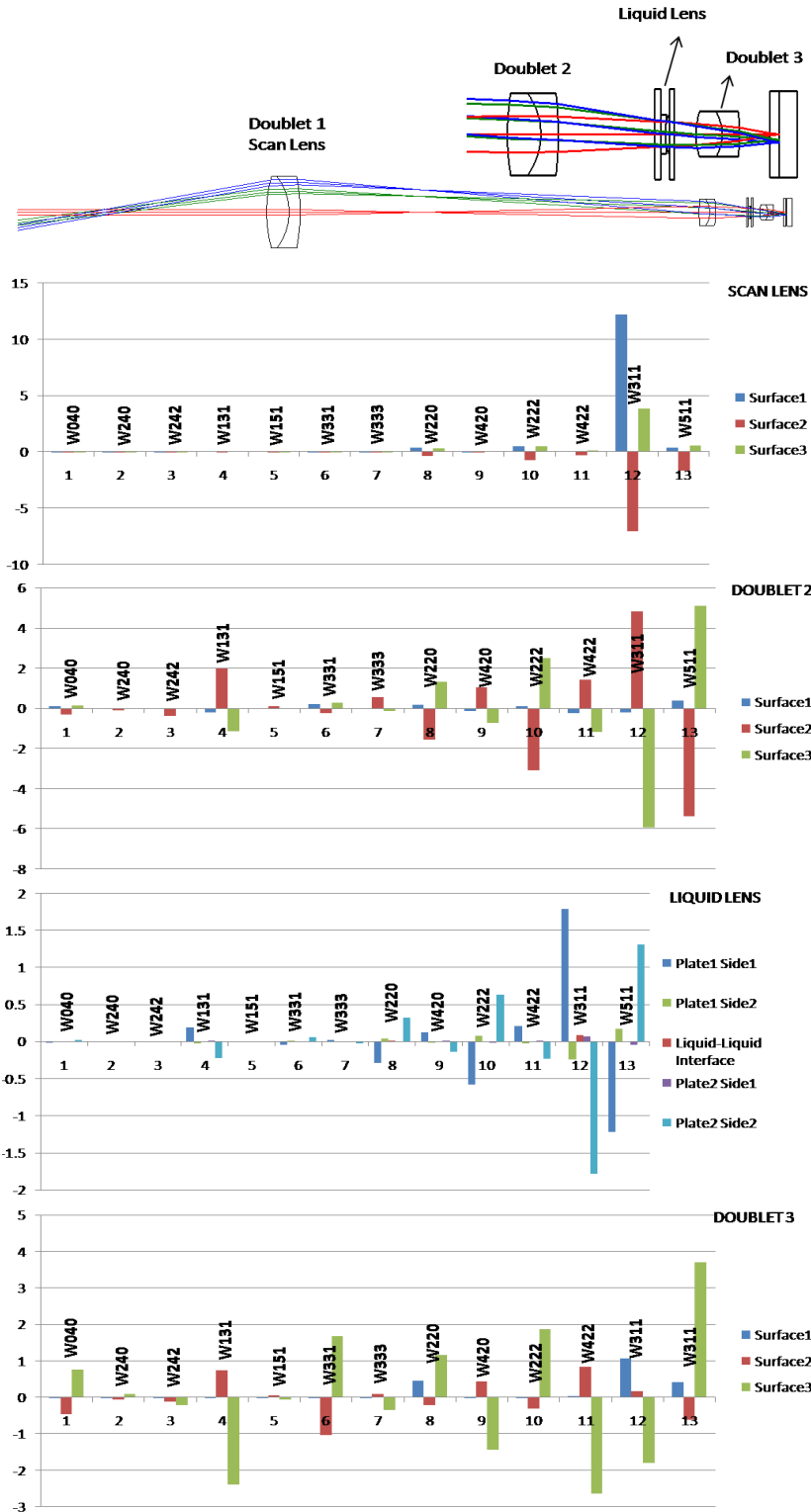
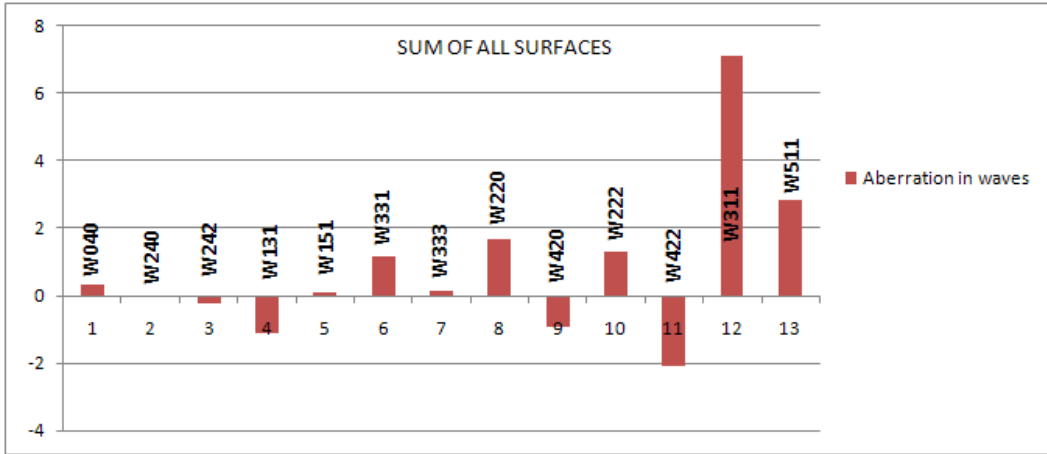
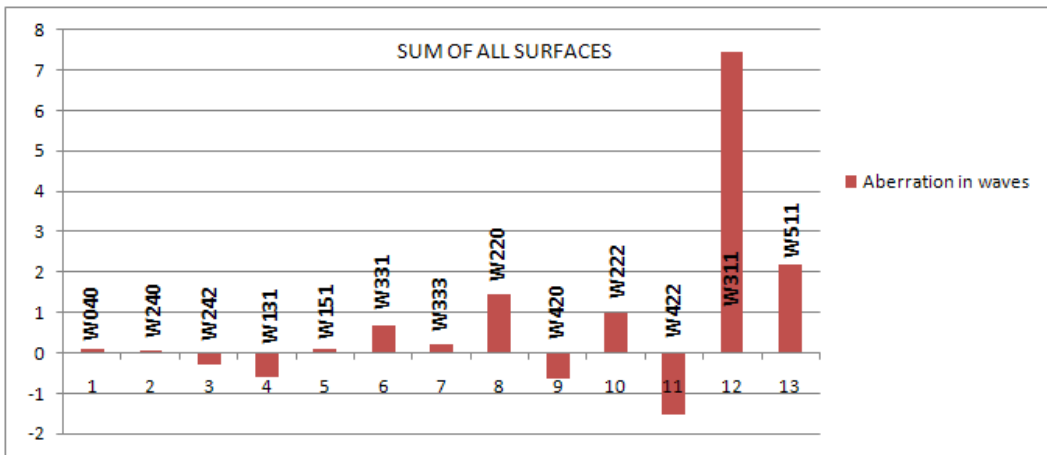


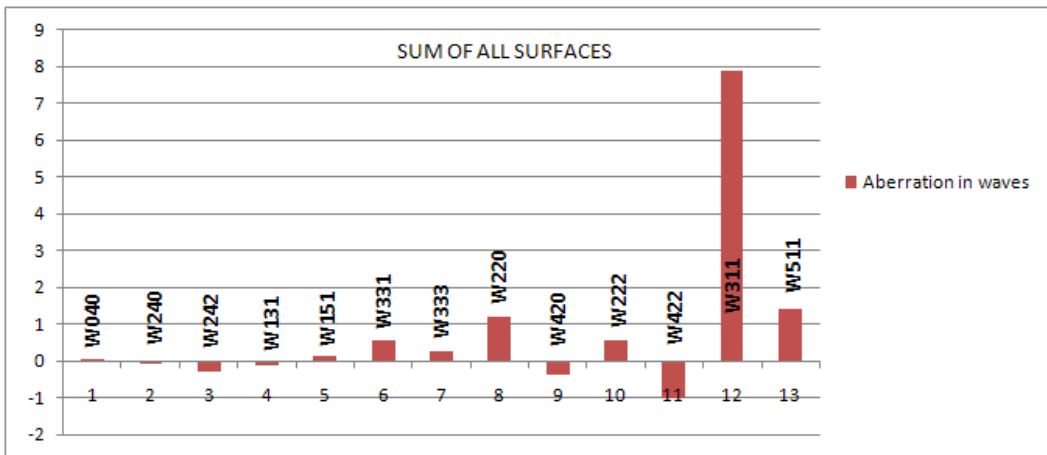
Figure 3.18: Optical layout and third and fifth order aberration contribution (units in waves @ 809 nm) for each surface of the dynamic focusing microscope with focus location fixed at the center (i.e.1 mm depth) of the sample



(a)



(b)



(c)

Figure 3.19: Third and fifth order aberrations of the dynamic focus microscope (units in waves @ 809 nm) at focal depths of (a) 0 mm, (b) 1 mm and (c) 2 mm inside the sample

The astigmatic field curves and distortion for the system are shown in Fig. 3.20. The largest residual astigmatic error is present at approximately the 70% field of view. The effect of this residual astigmatism in addition to the small amount of residual coma can be witnessed in the marginally larger asymmetry of the FWHM of the PSF function generated at the 70% field (shown in Table 11), when compared to the on-axis values.

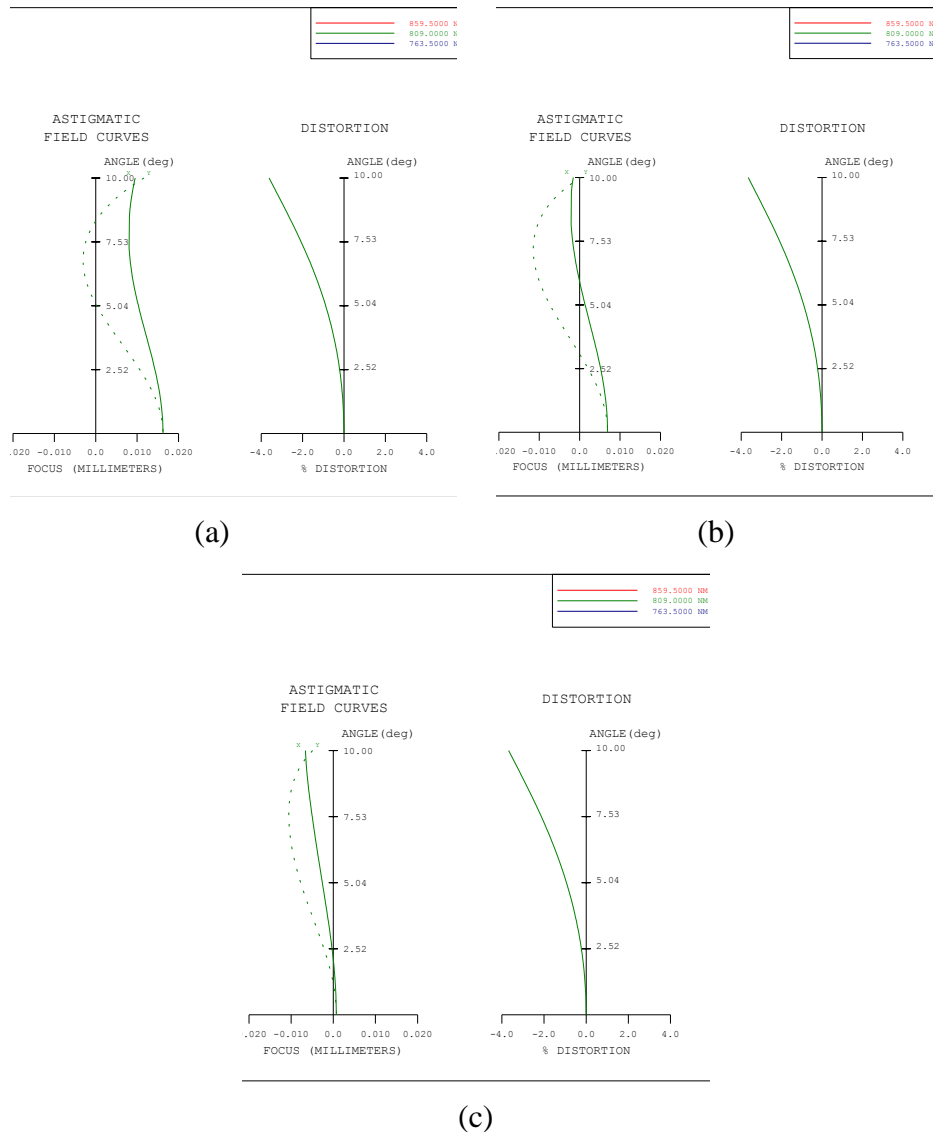
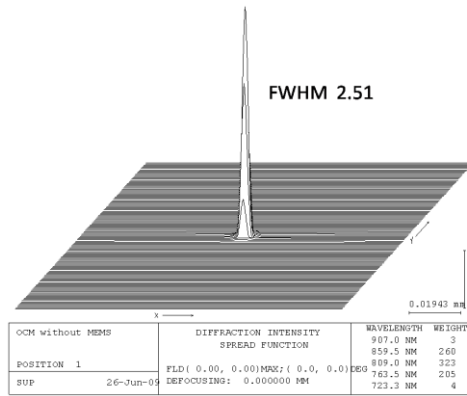
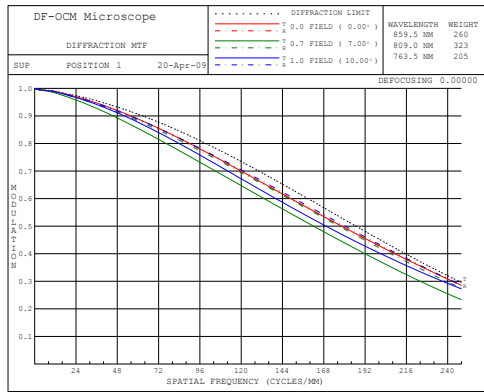


Figure 3.20: Field curves of the dynamic focus microscope at focal positions of (a) 0 mm; (b) 1 mm; (c) 2 mm inside a medium of refractive approaching that of skin

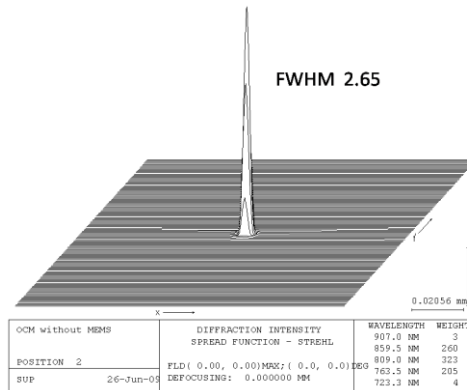
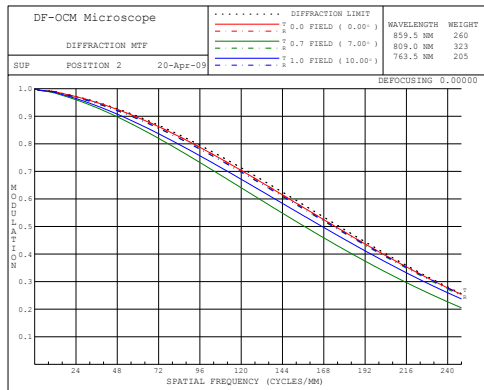
Table 11: RMS wavefront error and Strehl ratio at the composite best focus image plane located at $-0.46 \mu\text{m}$ from the paraxial image plane.

Focus position (mm)	FOV (a.u.)	RMS wavefront error (waves)	Strehl ratio	FWHM (μm)		
				X Dia	Y Dia	Y/X
0	0	0.034	0.95	2.51	2.51	1.00
	0.7	0.047	0.92	2.51	2.68	1.07
	1	0.050	0.91	2.52	2.55	1.01
1	0	0.019	0.99	2.65	2.65	1.00
	0.7	0.034	0.96	2.63	2.81	1.07
	1	0.042	0.93	2.65	2.70	1.02
2	0	0.007	0.998	2.77	2.77	1.00
	0.7	0.029	0.97	2.72	2.92	1.07
	1	0.039	0.94	2.76	2.80	1.02

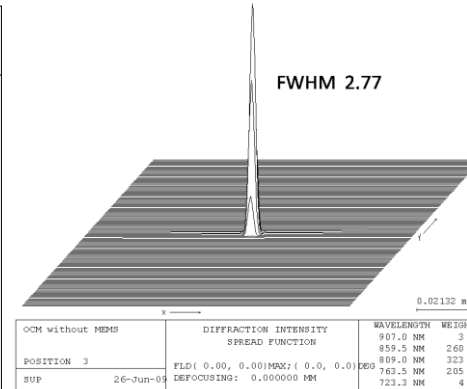
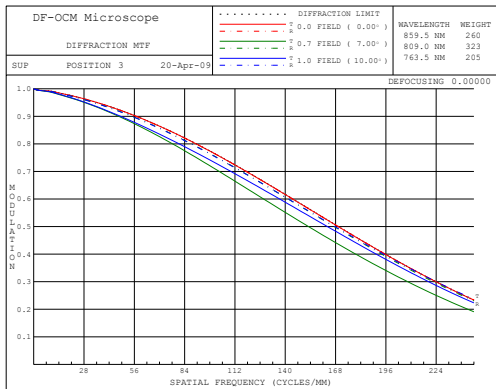
MTF plots were used to estimate the resolution achieved by the system. Fig. 3.21 shows the diffraction MTF curves generated for 3 different focus positions located at 0, 1 and 2 mm, respectively. The MTF curves indicate a constant contrast of greater than 20% at a frequency of 250 lp/mm (corresponding to $2 \mu\text{m}$ lateral resolution) at all the analyzed focal depths and FOV. It can be noted that the effect of astigmatism at the 0.7 relative FOV shown earlier can be easily related to the MTF contrast% drop in the plots for that field as shown by the green line in Fig. 3.21. Additionally, the minimal effect of coma can be detected in the slight difference in MTF contrast between the sagittal (dotted line) and tangential (plain line) curves, which increases with larger FOVs corresponding to the green and blue lines. The PSF on-axis at all three focal positions are plotted in Fig. 3.21 as well. As a measure of resolution, Table 11 summarizes the Strehl ratios, RMS wavefront errors and the FWHM of the point spread function as a function of the focal depth and FOV. The ray aberration curves shown in Fig. 3.22 trace the ray error as a function of the aperture in the tangential and sagittal planes. It can be seen from these curves that lateral color has been minimized.



(a) 0 mm

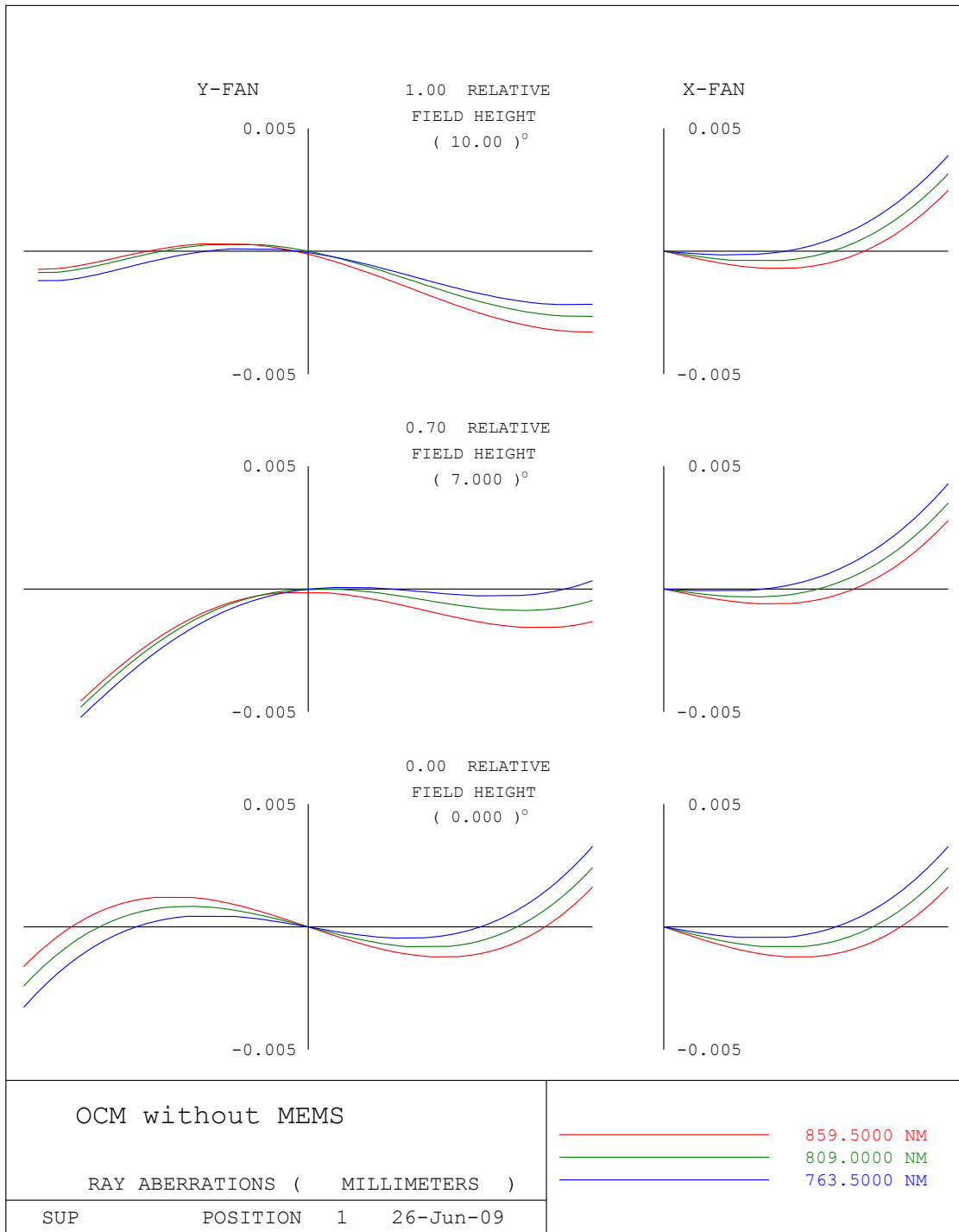


(b) 1 mm



(c) 2 mm

Figure 3.21: (Left) MTF curves and (Right) PSF on-axis are shown at the three focal positions namely 0 mm, 1 mm and 2 mm inside a medium of refractive approaching that of skin.



(a)

Figure 3.22: (Contd. next page) Ray aberration curves across the FOV at the focus depths of (a) 0 mm; (b) 1 mm; (c) 2 mm inside a medium of refractive approaching that of skin

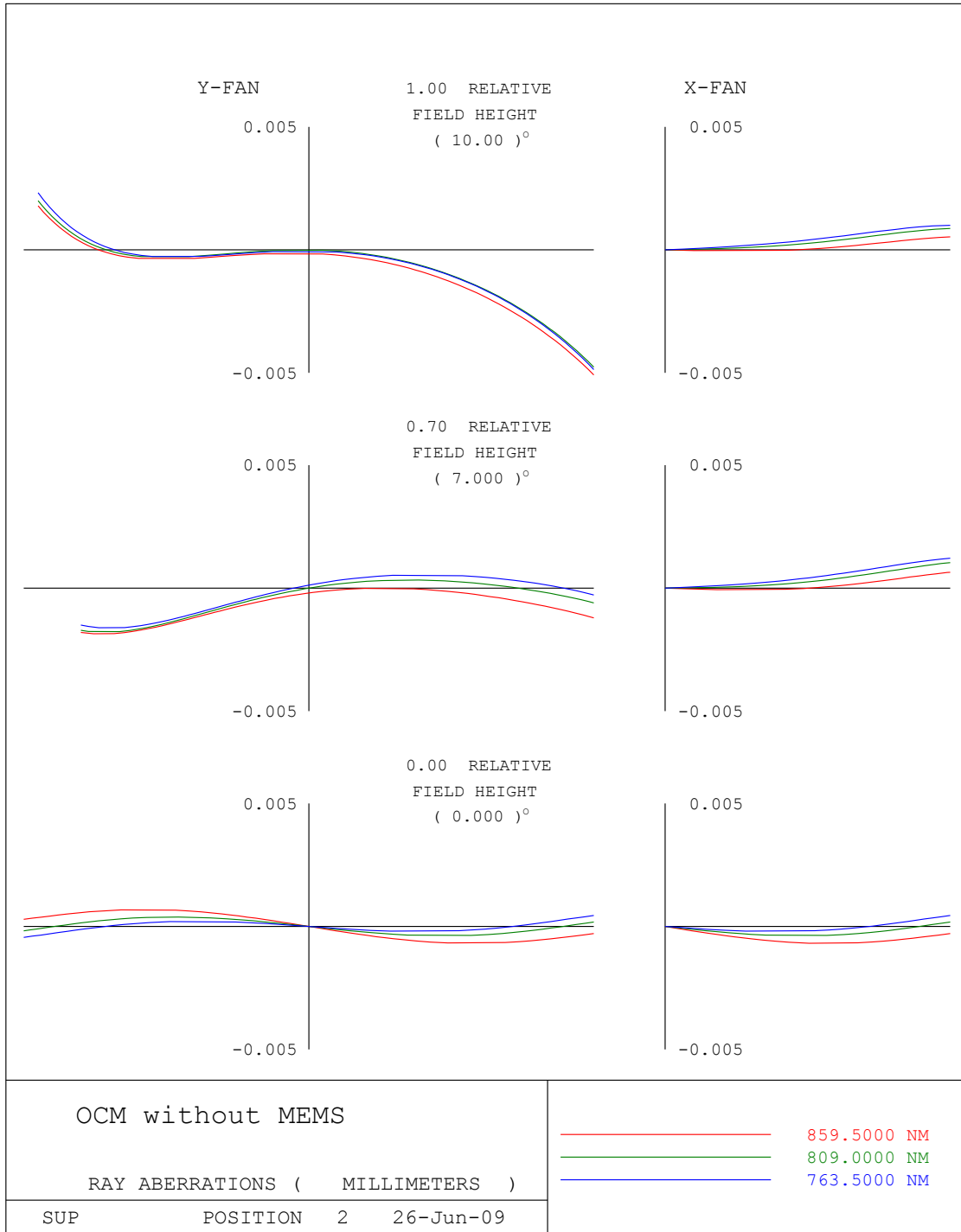


Figure 3.22(b)

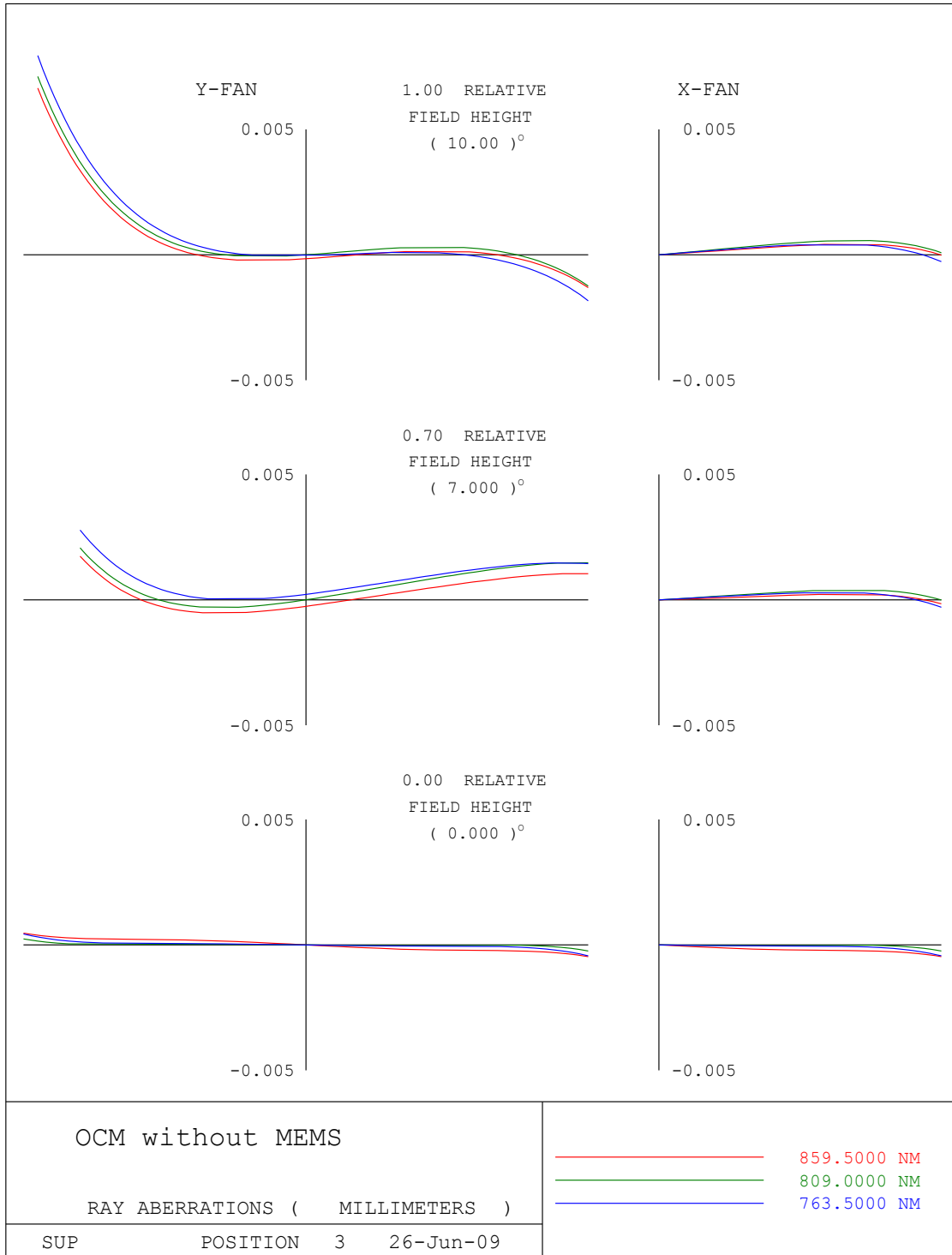


Figure 3.22(c)

CHAPTER 4- DESIGN TOLERANCING, FABRICATION AND TESTING

The optical design having been completed and analyzed for optimal performance, the next step was to test the design for sensitivity and arrive at the desired manufacturer tolerances. Subsequently, the requirements and constraints were to be laid out for the design of the mechanical housing for the three doublets, liquid lens, and related components. This was then followed by fabrication and assembly of the research prototype and finally testing for performance metrics.

4.1 Optical Tolerancing

Determining the sensitivity of a system to fabrication errors is a crucial step in an optical system design process. Therefore, designing a robust system that is pre-evaluated for its tolerance to manufacturing inaccuracies is a vital link between design and engineering. A thorough tolerance assignment contributes considerably towards the improvement of the production cost factor, process selection, tooling, set-up cost, required operator skills, quality inspection and rework. System tolerances that are tight can limit the choice in optical fabrication shops available that can meet the demand for high accuracy. Moreover, tight tolerances increase the fabrication, assembly and testing costs. Therefore, a rational and exhaustive algorithm is necessary to predict the tolerances of a system. Statistical methods are a powerful tool that can assess the effect of deviations from design specifications on system performance. Moreover, such predictive algorithms can be used to devise compensation parameters to simulate adjustments that can be made during the assembly process.

A tolerance analysis was conducted in CodeV™ for the dynamic focusing microscope objective using Optical Research Associates' proprietary wavefront differential algorithm for diffraction MTF performance measures. In this algorithm, a single ray trace of the nominal system is used to compute the differential wavefront changes as a function of the parameter changes for each tolerance limit. The function is then extended into a function of multiple variables by taking permutations of wavefront differentials for two parameters at a time. These results are then statistically combined to arrive at an overall system performance prediction, along with the individual MTF performance values for each surface. The tolerance analysis was executed in the inverse sensitivity mode, where tolerance values were varied within user-defined limits and each limit was optimized to have approximately the same impact on the system performance.

Table 12: Fabrication tolerances and cost category for General Optics (Asia) Ltd.

PARAMETERS	TOLERANCE LIMITS	
Radius of Curvature error (μm) - 0.1% Standard		
<i>Radius Range</i>	<i>Best (μm)</i>	<i>Standard (μm)</i>
2-20 mm	2.0	5.0
20-50 mm	3.0	5.0
50-100 mm	5.0	15.0
Wedge & Tilt -single indicator reading (μm)		
<i>Lens Diameter</i>	<i>Small volume <10</i>	<i>Large volume > 10</i>
Dia < 10 mm	1.5	2.5
Dia > 10 mm	0.5	2.0
Decenter Roll -2 indicator reading (μm)		
Dia < 10 mm	3.0	5.0
Dia > 10 mm	1.0	4.0

The tolerance limits were set to fall within the 'Standard' cost category of the manufacturer (See Table 12). A thickness compensator was included for the image surface defocus in order to find the best focus. A z displacement tolerance or power tolerance was added to the tolerance set to

allow up to 4 fringes of error on the outer surfaces and 12 fringes on the inner surface of the doublets. Radius tolerances of 0.25% were specified on all surfaces except those of the liquid lens. Thickness tolerances of 0.05 mm in glass and 0.025 mm in air were allowed between surfaces along the optical axis. Material errors were limited to the order of 0.001 in homogeneity of index and to the order of 0.008 for the abbe number. The surface irregularity tolerances were controlled to 1 wave on the outside surfaces and 4 waves in the interface between each doublet. Barrel tilt in radians for doublet 1 was set to 0.011, doublet 2 set to 0.0019, and doublet 3 set to 0.0038. While the decenter of the scan lens was controlled more loosely at 0.1 mm, for the doublets 2 and 3 they were tighter at 0.025 and 0.05 mm respectively since they were more sensitive to overall performance. Roll of each doublet as indicated by the TIR was controlled to vary up to 0.025 mm. Only decenter tolerances were applied to the liquid lens to the order of 0.25 mm given the uncertainty of the centering of the lens within its mount. The specified fabrication tolerances in design are summarized in Table 14. An MTF performance drop of less than 10% after fabrication is predicted in theory. The MTF performance summary measured at 70% of the maximum modulation frequency, namely 143 lp/mm, with tolerances included in the design is shown in Table 13. Given that typically post-fabrication tests for resolution measures are performed on-axis, the off-axis fields were assigned minimum weights for the computation.

Table 13: Performance summary after tolerance analysis
Polychromatic Modular Transfer Function

RELATIVE FIELD	FREQ L/MM	AZIM DEG	WEIGHT	DESIGN	DESIGN + TOL *	COMPENSATOR RANGE (+/-) *
						DLZ S24
0.00, 0.00	143.00	TAN	1.00	0.6175	0.5755	0.242431
0.00, 0.70	143.00	TAN	0.01	0.5500	0.4814	0.242431
0.00, 1.00	143.00	TAN	0.01	0.5873	0.4754	0.242431
0.00, 0.00	143.00	RAD	1.00	0.6175	0.5747	0.242431
0.00, 0.70	143.00	RAD	0.01	0.6119	0.5682	0.242431
0.00, 1.00	143.00	RAD	0.01	0.6141	0.5575	0.242431

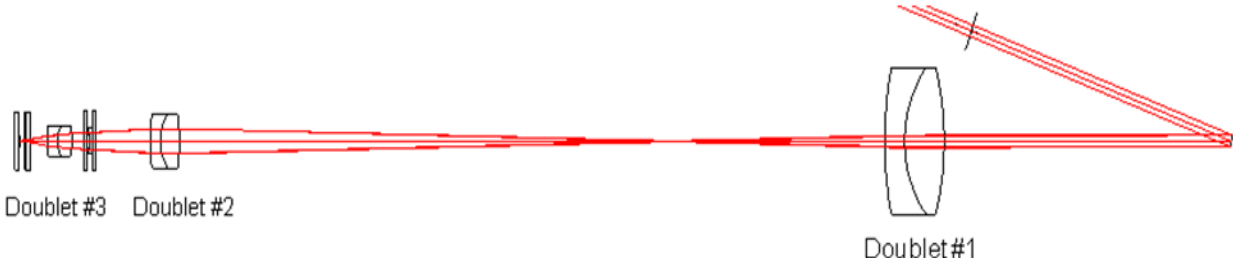


Figure 4.1: Optical design layout and doublet naming convention in the tables that follow.

Table 14: Fabrication data and initial design specified tolerances

Doublet #	Surface	Radius (mm)	Thickness (mm)	Power (fringes) @ 546.1nm	Irregularity (fringes) @ 546.1nm	Radius Error		Thickness Error (mm)	Index Error	Abbe No. Error	Element Wedge TIR (mm) (arc min.)		
						(%)	(mm)						
1	1	46.950	8.000	4	1	0.25%	0.117	0.050	0.001	0.800	0.048	7.0	
	2	-20.850	4.000	12	4	0.25%	0.052	0.050	0.001	0.800			
	3	-63.000	142.585	4	1	0.25%	0.158	0.025	air		0.030	4.4	
2	4	29.000	3.850	4	1	0.25%	0.073	0.050	0.001	0.800	0.025	10.7	
	5	-8.200	2.000	12	4	0.25%	0.021	0.050	0.001	0.800			
	6	-44.000	11.100	4	1	0.25%	0.110	0.025	air		0.013	5.6	
			2.230	Liquid lens goes here									
			2.500					0.025					
3	7	8.625	3.000	4	1	0.25%	0.022	0.050	0.001	0.800	0.013	12.8	
	8	-5.050	2.000	12	4	0.25%	0.013	0.050	0.001	0.800			
	9	-19.050	3.475	4	1	0.25%	0.048	0.025	air		0.013	12.8	
	10		1.000	Cover glass						0.001	0.800	0.013	20.7
	11		0.100										
	12		2.000										

The tolerances on the optical elements were further tightened during manufacturing because of the higher standard shop optical tolerances that could be met by the manufacturer at no additional cost. The final assigned radius tolerances are shown in Table 15. In addition, the wedge tolerances being critical for final imaging performance were controlled to about 20% of the design specified tolerances to the order of 1 to 2 arc minutes. Other tolerances such as power and irregularity that were looser than the standard shop tolerances were set to the standard limits.

Table 15: Final assigned shop tolerances for prototype fabrication

Doublet #	Specified Radius +/- tolerance (mm)	Assigned Radius +/- tolerance (mm)
1	46.95 +/- 0.117	46.95 +/- 0.022
	20.85 +/- 0.052	20.85 +/- 0.014
	63 +/- 0.158	63 +/- 0.04
2	29.00 +/- 0.073	29.00 +/- 0.035
	8.2 +/- 0.021	8.2 +/- 0.018
	44 +/- 0.110	44 +/- 0.090
3	8.625 +/- 0.022	8.625 +/- 0.013
	5.05 +/- 0.013	5.05 +/- 0.013
	19.05 +/- 0.048	19.05 +/- 0.040

4.2 Fabrication and Calibration

Several constraints were taken into consideration in the mechanical design of the microscope. The first was the ease of handling required for future applications as a clinical prototype. The microscope also needed to have modular construction to enable independent evaluation of the objective and collimator after fabrication as well as the easy removal and replacement of the liquid lens in case of malfunction. In addition, a break in the tube at the focus of the scan lens, where an alignment crosshair might be inserted (and later removed) for alignment, was incorporated in the design. Also, the prevention of ingress of gel into the microscope by

incorporating air-tight construction around the cover glass was an important feature that had to be taken into account due to the intended operation in immersive medium. The design had to accommodate the voltage controlled liquid lens, and provide an attached mount to interface with a scanning mirror to enable 3D GD-OCM. Furthermore, a precisely inclined housing had to be built in order to seat the fiber-optic feed from the femto-second laser with sufficient alignment for the scanner. The ease of positioning of fiber optic coupler and scanning mirror in order to obtain accurate alignment and orientation of the scanning beam was taken into consideration.

For the fabrication of the mechanical components, the machining process was chosen to give a smooth surface finish in addition to meeting dimensional tolerances. A satin dull black anodizing

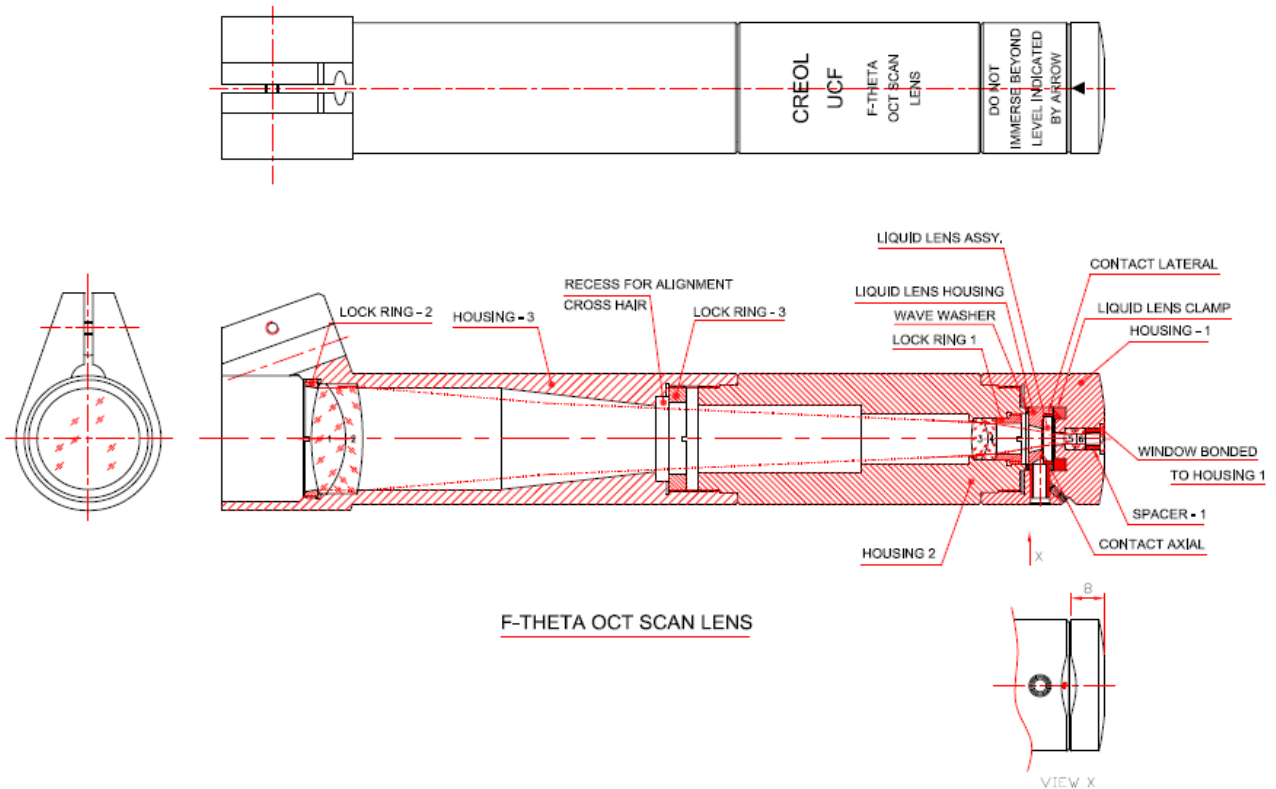
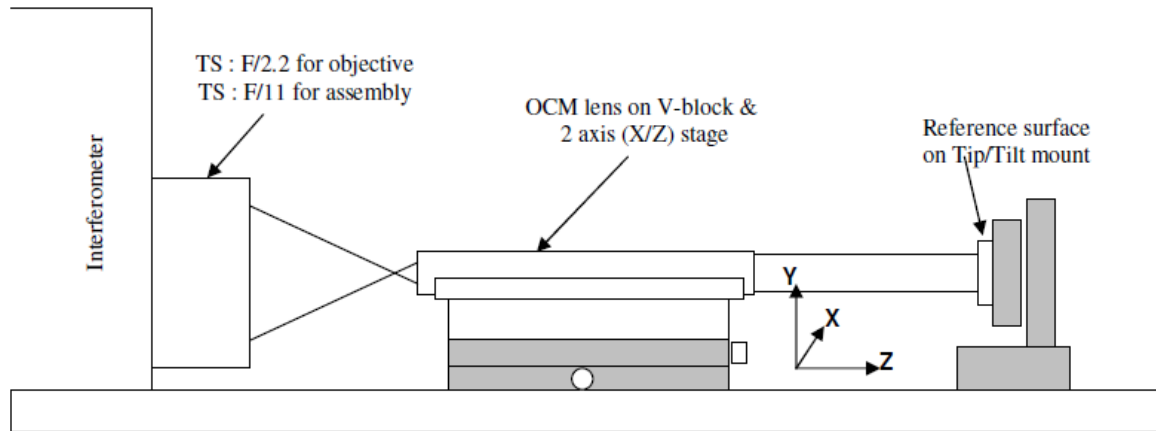


Figure 4.2: Mechanical design layout – top view and section view.

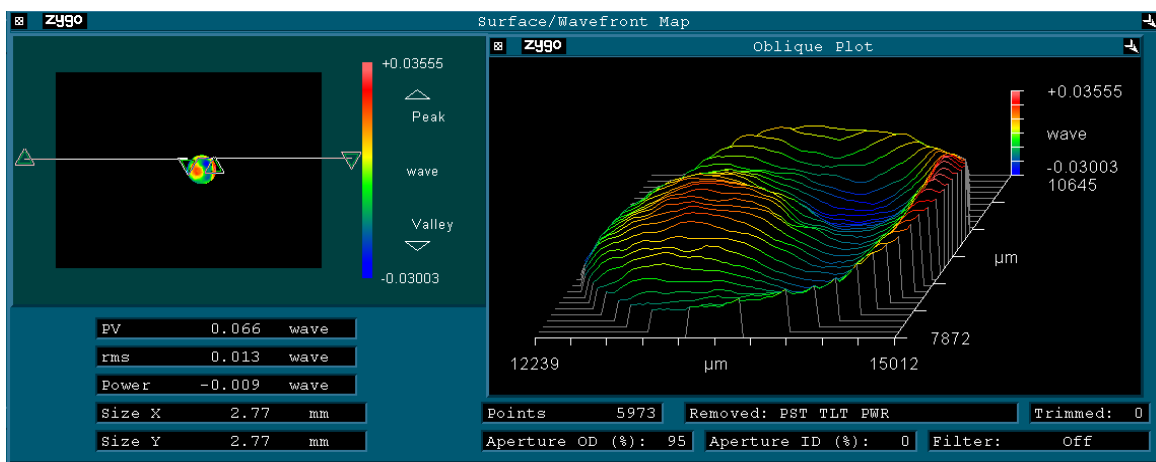
surface treatment was given to reduce unwanted reflections from the metal components and thereby contribute to improve system performance. The final mechanical housing for the optics of the microscope is shown in Fig. 4.2. A tolerance grade of H7G6 was followed for the manufacture of the metal parts, where H7 corresponds to the tolerance of holes, G6 for shafts as outlined in the precision guidelines of ISO 286-1 –1988 and ISO 286-2 –1988 for positioning and sliding. During the fabrication process, the concentricity of lens seats, spigots and their locating bores were ensured to be better than specified tolerances by machining in one setting.

Following the final opto-mechanical design and fabrication, the assembly was tested for output wavefront error using a plane transmission sphere (TS) and a Helium Neon light source at 632.8 nm in a Zygo interferometric set-up show in Fig. 4.3(a) The RMS wavefront error of 0.013 waves (shown in Fig. 4.3(b)) achieved by the assembled optics with the liquid lens removed from the system exceeded the standard definition for a diffraction-limited system, typically < 0.07 waves. The diffraction-limited RMS performance of less than 0.07 waves was still retained with the liquid lens installed within the assembly as shown in the measurements in Fig. 4.3(c).

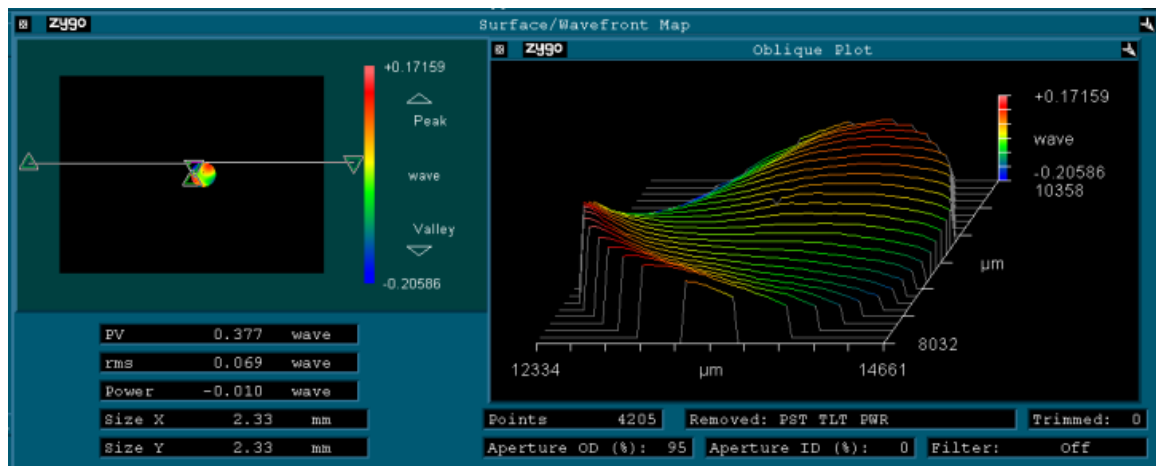
These nominal performance measures demonstrate the success of the fabrication process on meeting alignment specifications as well as fabrication tolerances of the system. Furthermore, the diffraction limited performance also reflects on the validity of the theoretical model of the liquid lens and counteracts some industry misconceptions that the wavefront from liquid lenses is not adequate for high performance imaging applications. While this is often true for liquid lenses used standalone, when properly packaged in an integrated optical design the performance of the liquid lens is found not to be a factor that degrades the performance of the system.



(a) Zygo interferometric test set-up



(b) No liquid lens



(c) With/liquid lens

Figure 4.3: Wavefront aberration map of the fabricated optics on axis with and without the liquid lens included in the system tested in a Zygo interferometer at 632.8 nm –Performance demonstrates diffraction limit given that RMS wavefront error < 0.07 waves

In addition, post-fabrication, departure from the original specifications for radius of curvature and surface irregularity of the individual surfaces was measured. The results reported in Table 16 show that the prototype parameters were met within specifications. It must be noted that the surface irregularity values were measured over the full diameter of the lens. The measurements over the clear aperture (used area of the lens) are expected to be higher.

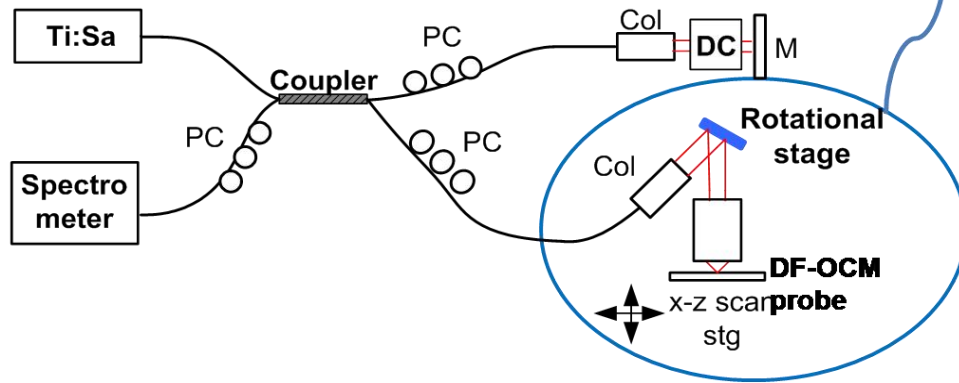
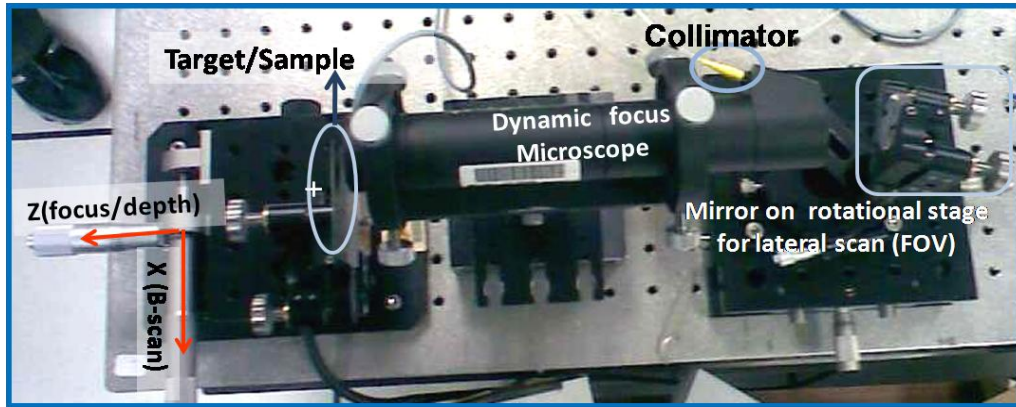
Table 16: Surface by surface errors of each doublet measured after fabrication

Doublet#	Side#	Radius of curvature (mm) Spec.	Radius of curvature (mm) Measured	Surface Irregularity PV (wave) Spec.	Surface Irregularity PV (wave) RMS (wave) Measured
1	1	63.00+/-0.040 (cx)	62.995	0.4	0.147 0.027
	2	46.95+/-0.022 (cx)	46.950	0.4	0.080 0.016
2	1	44.00+/-0.090 (cx)	44.016	0.4	0.067 0.009
	2	29.00+/-0.035 (cx)	28.990	0.4	0.110 0.020
3	1	19.05+/-0.040 (cx)	19.048	0.4	0.053 0.009
	2	8.625+/-0.013 (cx)	8.633	0.4	0.176 0.035
Window	1	Infinity (Power : 0.25 wave)	Power : 0.085 wave	0.1	PV : 0.019
	2	Infinity (Power : 0.25 wave)	Power : 0.060 wave	0.1	PV : 0.018

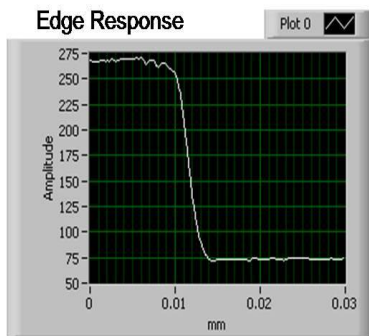
4.3 Testing and Experimental Analysis

The Modulation Transfer Function (MTF) was used to represent image quality as quantified by lateral resolution and depth of focus of the optical system (Murali 2009a).

4.3.1 Experimental set-up

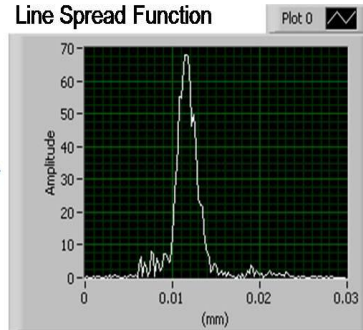


(a)



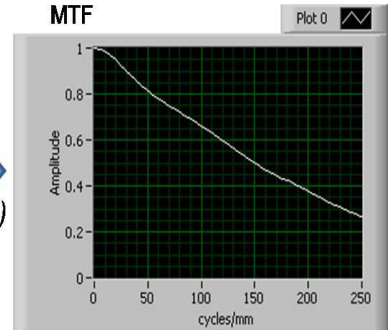
(b)

$\frac{d}{dx}$



(c)

$F(x)$



(d)

Figure 4.4: (a) Experimental set-up: PC – Polarization controller; Col – Collimator, DC – Dispersion compensator; M- Mirror, DF-OCM –Dynamic focus OCM and (b-c) MTF calculation method.

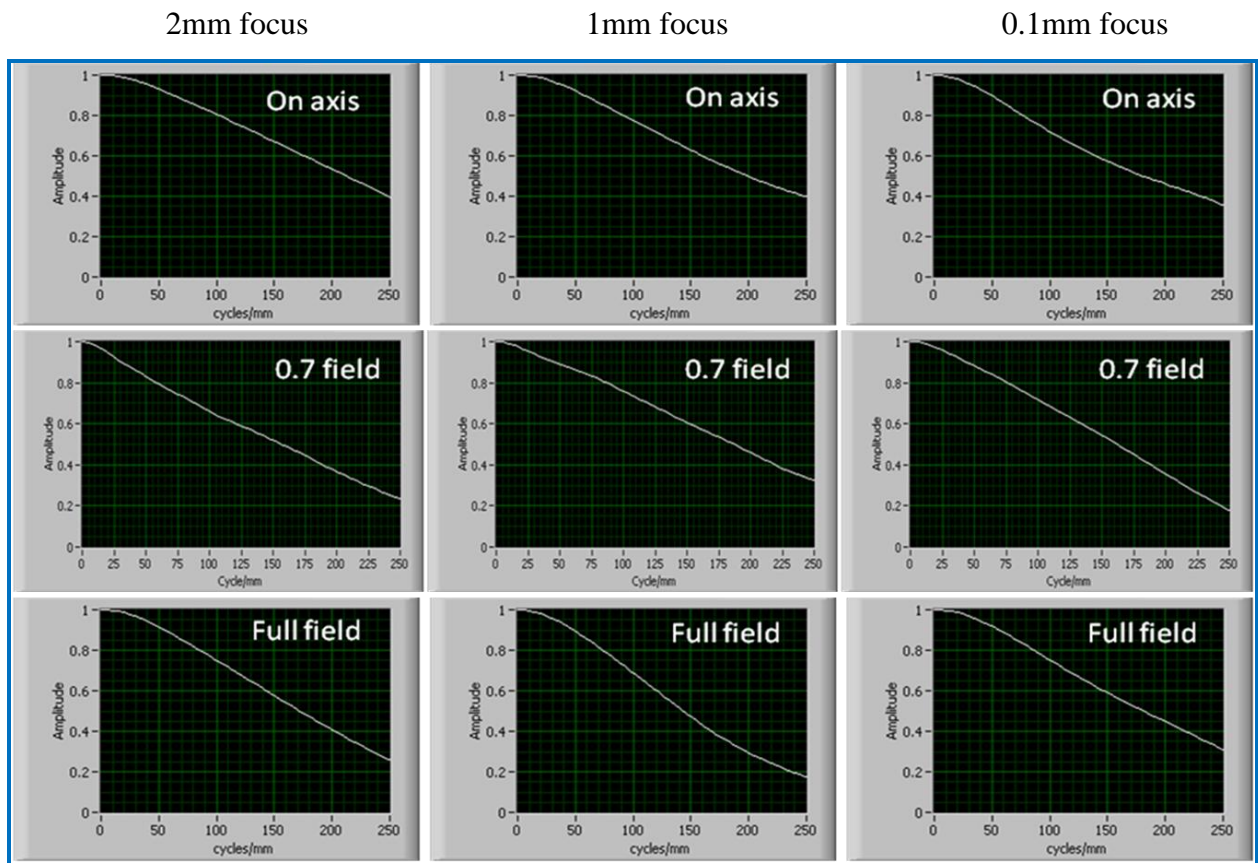
We first implemented a spectral domain OCM system based on a fiber optic interferometer as shown in Fig. 4.4(a). The dynamic focusing probe was integrated into the sample arm of the Michelson-geometry interferometric set-up for enabling GD-OCM. A variable frequency target (Edmund Optics, 5-200 lp/mm) was used as the sample, and was illuminated by a broadband Titanium: Sapphire laser source (Femtolasers Inc.), which has a spectral bandwidth of 120 nm centered at 800 nm providing $\sim 2.5 \mu\text{m}$ axial resolution in air. A spectrometer with a 3648 CCD pixel line array (HR 4000; Ocean optics Inc.) was used as the detector. The 80% intensity beam from the fiber-coupler was collimated and then incident on the dynamic focusing microscope integrated into the sample arm of the GD-OCM system. The light was then focused on a reflective edge of chrome on glass of the target. The 20% intensity beam from the fiber-coupler was passed through a Fourier-domain optical-delay-line (Lee 2005) and a polarization controller (Thorlabs, Model FPC030) in the reference arm in order to control the overall dispersion and maximize the signal modulation depth in the system. The dynamic focusing microscope was illuminated by a collimated beam of diameter 2 mm that was reflected into the optics by the use of a rotationally adjustable mirror. The position of the mirror sets the field angle for imaging. The focal plane in the sample was varied by adjusting the voltage on the built-in liquid lens in the dynamic focusing microscope objective.

4.3.2 Measurement of lateral resolution in air

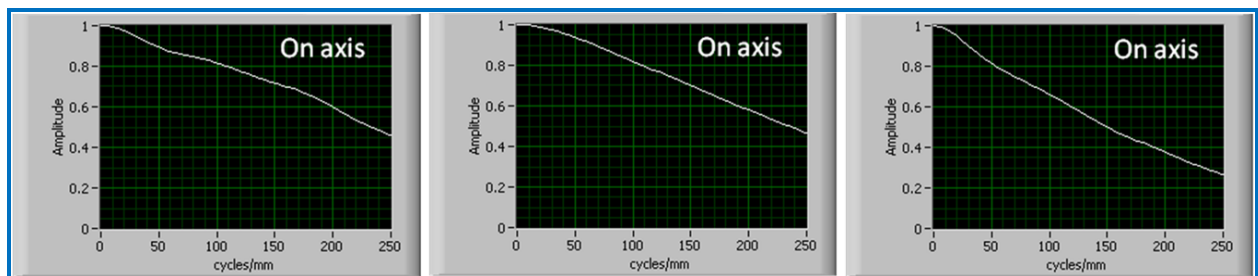
The MTF of the microscope was calibrated by scanning the 5 lp/mm reflective chrome edge on soda lime glass of the variable frequency target (Edmund Optics) with the microscope focused on the surface. Multiple scans (a total of 8 per focus) were measured and averaged to reduce the effects of random noise on the edge profile. The edge was sampled every $0.2 \mu\text{m}$ and

400 sampling points were recorded. Thereafter, a differentiation of the edge profile was carried out to yield the line spread function (LSF). The magnitude of the Fourier transform of the LSF yields the MTF. Figs. 4.4(b)-(d) show an example of such an MTF calculation. The MTF measurements were carried out at several focus positions of the liquid lens and different points in the FOV of the microscope. Fig. 4.5(a) shows the MTF curves at three focal depths ranging from the smallest to the largest value, each measured at three different points in the FOV. The MTF contrast at 250 lp/mm was found to be greater than 20%, thus validating the theoretical optical performance of the system.

The microscope was also tested in a vertical configuration in order to verify that there were no significant wavefront errors caused by the orientation of the liquid lens. It has been reported that liquid lenses less than 4 mm in diameter are insensitive to orientation and vibration (Kuiper 2004a; Kuiper 2004b). Moreover, the liquids used are chosen to minimize the effects of gravity on the liquid lens curvature. Fig. 4.5(b) shows the MTF curves measured across the FOV at three different focal depths in the vertical configuration. These results show that there is no significant loss in resolution when compared to the measurements in the horizontal configuration.



(a) Horizontal configuration



(b) Vertical configuration

Figure 4.5: MTF curves measured at 2 mm, 1 mm and 0.1 mm focus positions in a (a) horizontal configuration; (b) vertical configuration.

4.3.3 Depth of focus assessment in air

The theoretical full range DOF calculated according to the Gaussian beam confocal parameter based metric defined earlier in Eq.2.8 is $\pm 25 \mu\text{m}$. The theoretical full range DOF obtained using the Raleigh quarter wave defocus criterion defined in earlier in Eq.2.9 is $\pm 20 \mu\text{m}$. In order to experimentally quantify the DOF for the dynamic focusing probe, we measured the MTF at regular intervals of defocus from a fixed focus point i.e., a fixed voltage. Fig. 4.6(a) shows the MTF contrast measured at locations of increasing defocus with in-focus point set to be at the center of the depth range, namely at 1 mm in air. All the measurements were made with the microscope in the vertical orientation. We use the 20% minimum contrast criterion for the evaluation of the depth of focus a two-point separation of $2 \mu\text{m}$ (i.e., spatial frequency of

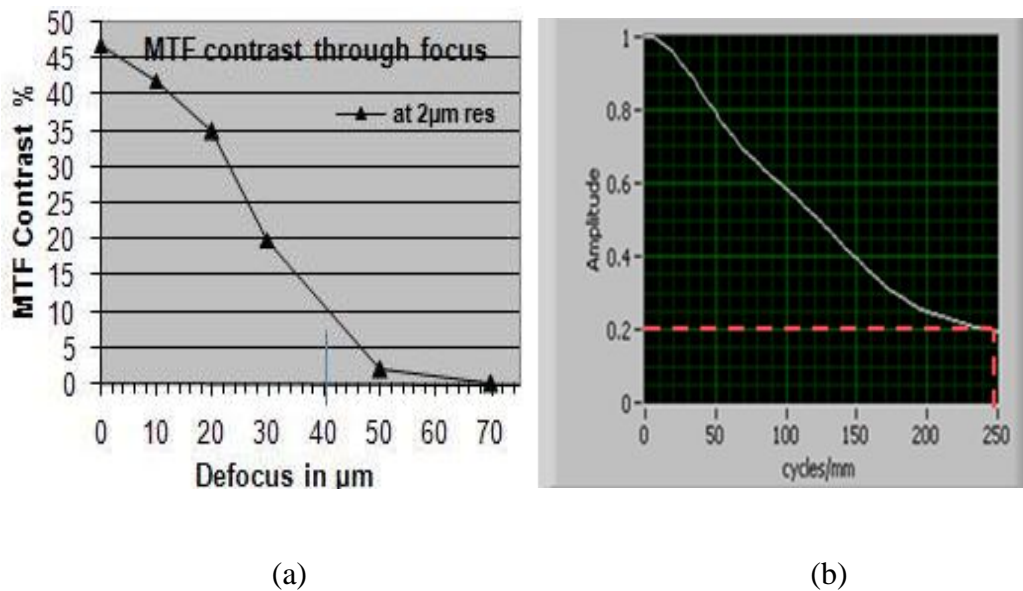


Figure 4.6: MTF measured at the center of the focus range, i.e.1 mm focal depth in air:
(a) Contrast % obtained at various points of defocus (b) MTF measured at $\pm 30 \mu\text{m}$ defocus still maintains over 20% contrast at 250 lp/mm corresponding to $2 \mu\text{m}$ resolution

250 lp/mm). Using this criterion, the two points were found to be resolved up to a defocus of

30 μm , corresponding to a DOF of 60 μm . Fig. 4.6(b) shows the measured MTF curve at the edge of the defocus range, namely 30 μm from a fixed focus location at the center of the depth range, namely at 1 mm in air. The DOF criteria and measurement results are summarized in Table 17.

Table 17: Summary of criteria for DOF

DOF Criterion	DOF definition	Full range DOF (μm)
Rayleigh range	$DOF = \pm \frac{\bar{\lambda}}{\pi\theta_s^2}$ (theoretical)	25
Rayleigh quarter wave defocus	$DOF = \pm \frac{\bar{\lambda}}{2 \cdot NA^2}$ (theoretical)	20
2 μm resolution	20% contrast in MTF @ 250 lp/mm (measured)	60

4.3.4 Evaluation of resolution and depth of focus in scattering media

The measurement of the above metrics for the quantification of system performance was followed by the evaluation of the imaging in scattering media. In order to simulate the scattering property of skin, a diluted 25 vol% solution of 3.5% fat milk and water solution was used (Eigensee 1996). The fat particles in milk serve as light scatterers and their density in a 25 vol% dilution gives rise to a scattering coefficient of 9.5 cm^{-1} that approximates that of bloodless skin tissue (Knuettel 1993). The dynamic focusing microscope head was then immersed in the milk solution in its vertical orientation and the voltage supplied to the liquid lens was adjusted for an image distance of 1 mm on-axis. The MTF data was then recorded on-axis when the target was

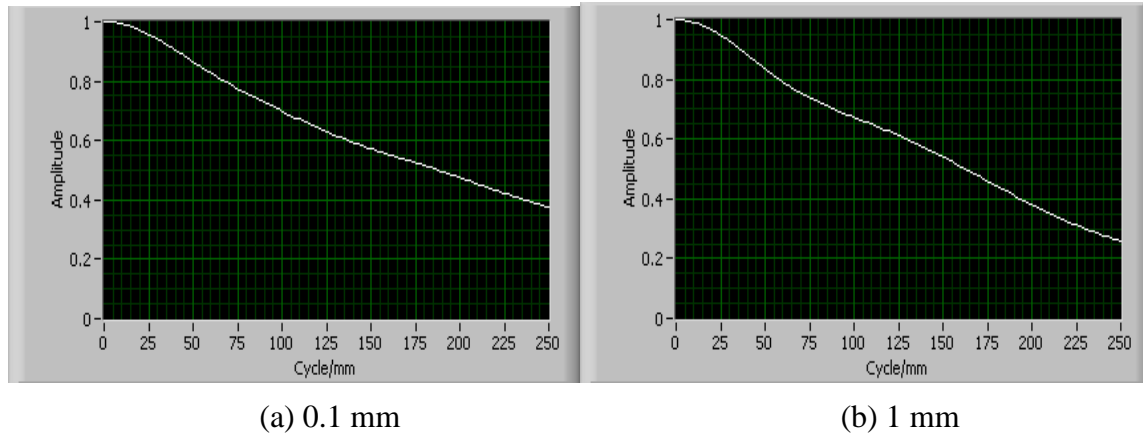


Figure 4.7: MTF curves measured at 0.1 mm, 1 mm focus positions with the dynamic focusing OCM microscope placed in a vertical configuration

in focus as well as at regular intervals of defocus as explained previously. The image distance was then changed in discrete steps by changing the voltage application and the MTF measurements were repeated. It was found that the MTF at 250 lp/mm was maintained over 20% while in focus up to a depth of 1mm. Fig. 4.7 shows the MTF curves obtained in focus at an imaging distance of approximately 0.1 mm and 1 mm inside the immersive medium.

Fig 4.8 shows the MTF curves recorded experimentally when the target was placed at different defocus distances from the best focus point when the voltage was fixed to image at a depth of 1 mm within the medium. It can be seen from the plot that using a minimum 20% at 250 lp/mm criterion, the DOF of the microscope approaches $\pm 30 \mu\text{m}$ in skin-equivalent medium. Results also concluded that beyond a depth of 1 mm in scattering media, the SNR is low due to high scattering and the interference signal becomes weak and is difficult to identify. Therefore, MTF measurements are reported only up to 1 mm in depth in this case.

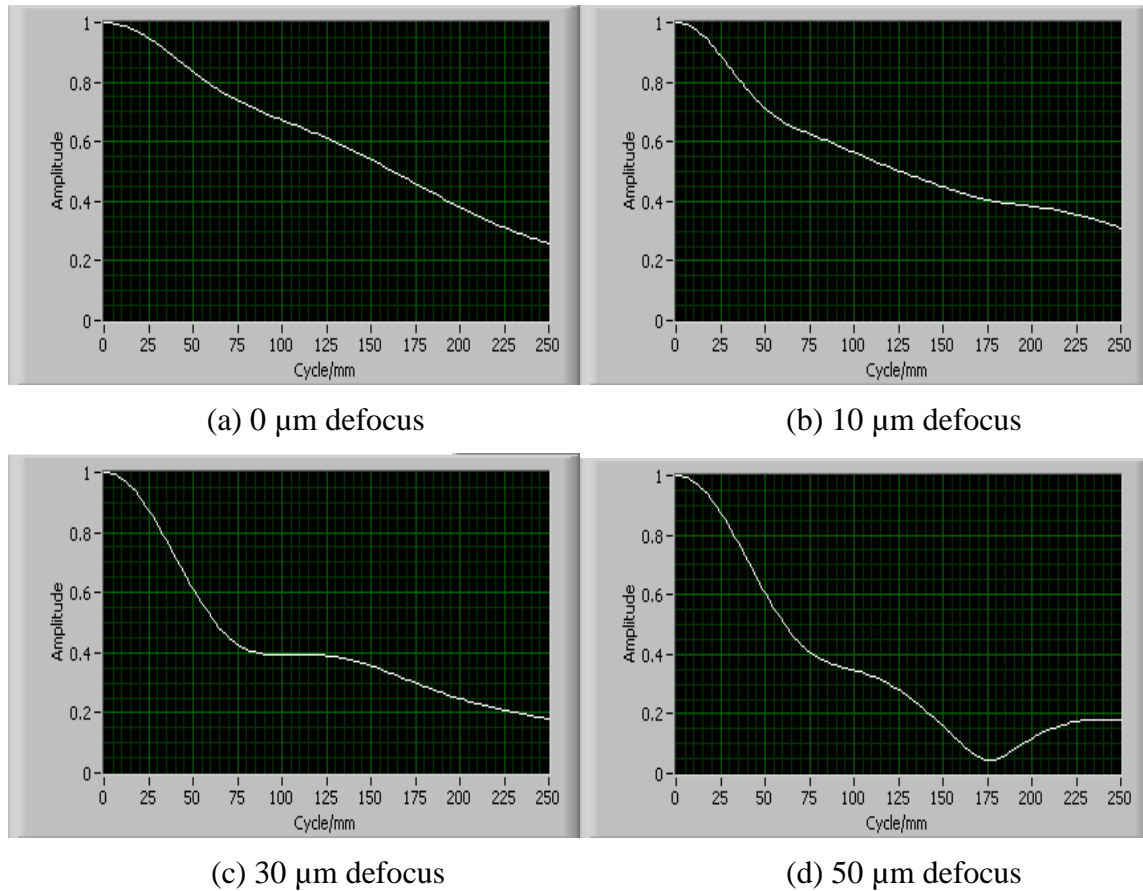


Figure 4.8: MTF curves measured at 0.1 mm, 1 mm focus positions with the dynamic focusing OCM microscope in a vertical configuration.

4.4 Biological Tissue Imaging Results

The next step after the quantification of performance metrics was to test the imaging capability of the dynamic focusing microscope in biological specimens. The microscope was mounted in the vertical configuration within a GD-OCM experimental set-up and images were acquired in both 2D and 3D in immersion in either water or glycerol.

4.4.1 2D imaging using the dynamic focusing microscope

The dynamic focusing microscope was used to obtain a 1mm^2 depth cross-section of the African frog tadpole (*Xenopus Laevis*) as shown in Fig. 4.9. The sample image was acquired in 10 depth zones with successive focus intervals of $100\ \mu\text{m}$ in depth, and water as the immersive medium.

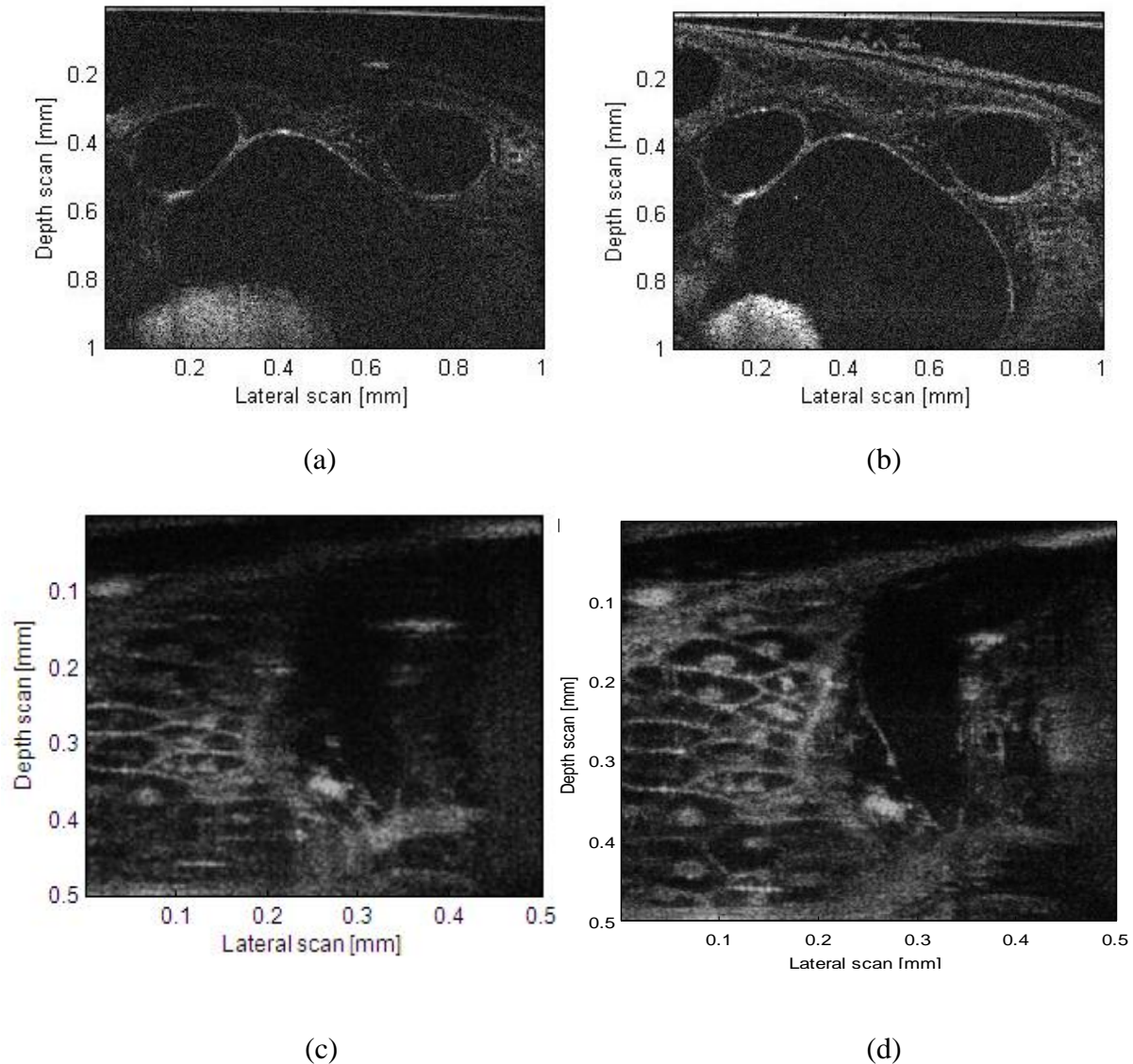


Figure 4.9: Cross-sectional image of *Xenopus Laevis* acquired (a) with fixed focus at $400\ \mu\text{m}$ below the sample surface; (b) with dynamic focusing every $100\ \mu\text{m}$ for 10 zones; (c) with fixed focus at $350\ \mu\text{m}$ below the sample surface; (d) with dynamic focusing every $100\ \mu\text{m}$ for 5 zones

The data in each B-scan or 2D slice contained 1000 A-scans with a sampling interval of 1 μm . Fig. 4.9(a) shows the depth cross-sectional image obtained with the focus approximately in the center of the sample. The loss in resolution outside the focus is clearly seen. The final Gabor domain fused image obtained from dynamic zone focusing is shown in Fig. 4.9(b) (Murali 2009a). Similarly, Fig. 4.9(c) and (d) show a different cross-section of an African frog tadpole immersed in glycerol, the former with the focus at approximately 350 μm and the latter after final fusion in the Gabor domain respectively. Results show that using dynamic focusing high lateral resolution is maintained across the depth of the sample, enabling the visualization of the cell structure and the sub-cellular nuclei under the surface. It can be seen from these images that dynamic focusing not only enables quasi-invariant lateral resolution throughout the depth of imaging, it also maximizes sensitivity and renders accurate scale of structures throughout the depth of imaging.

The process of obtaining invariant sub-cellular resolution using the Gabor domain algorithm is demonstrated in the African frog tadpole in Fig.4.10. A 500 μm^2 depth cross-section of the tadpole was imaged in 5 focus zones. The sample was immersed in 99% glycerol solution. The invariant high resolution is readily seen in the fused image since the cell walls are clear and the nuclei are sharply distinguished simultaneously throughout the lateral FOV and depth, thus demonstrating the invariant lateral and axial resolution capability at the sub-cellular level.

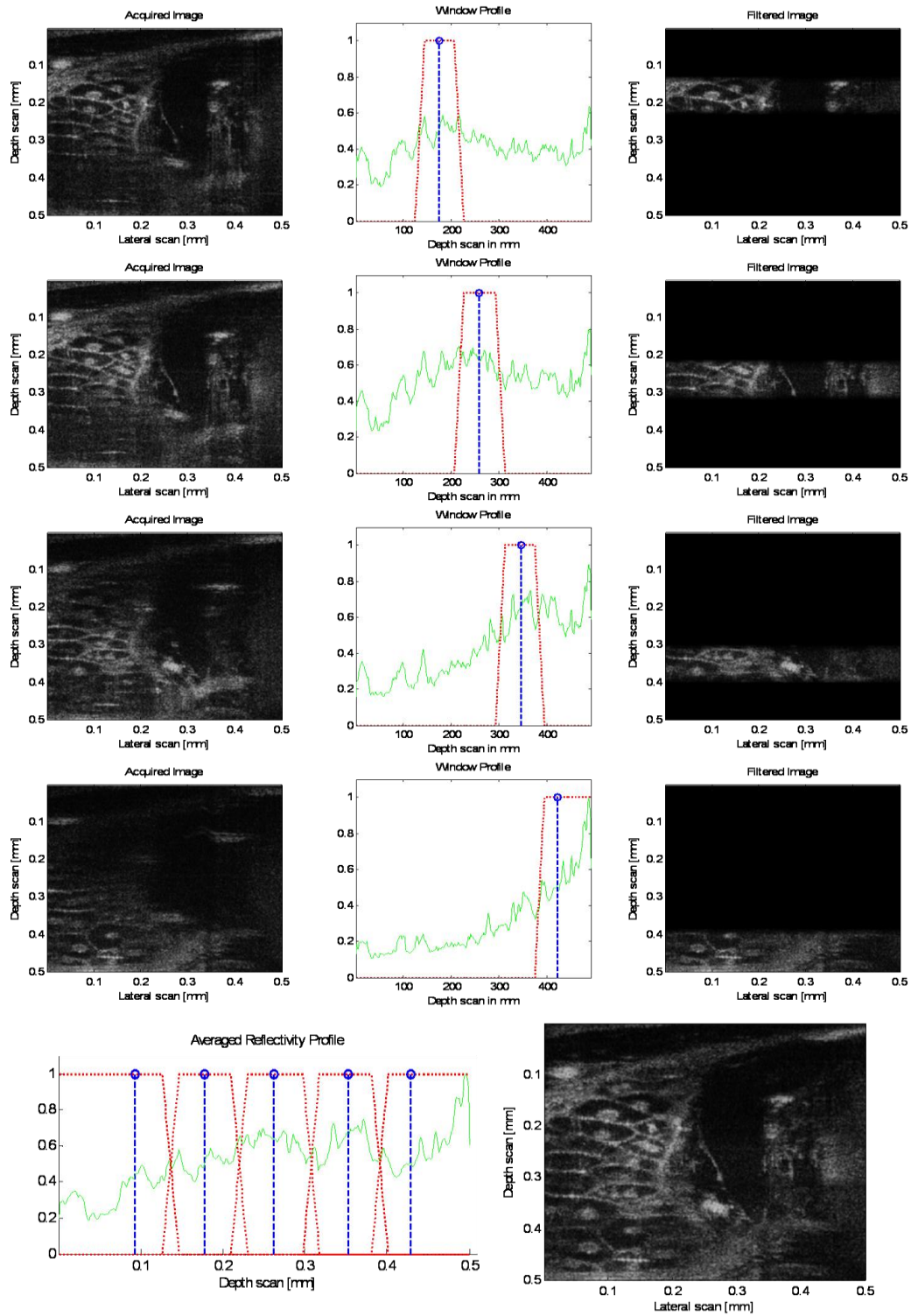
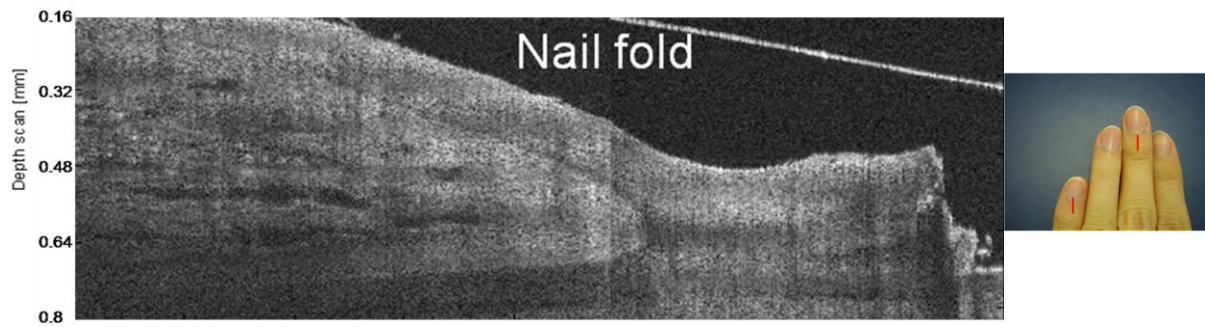
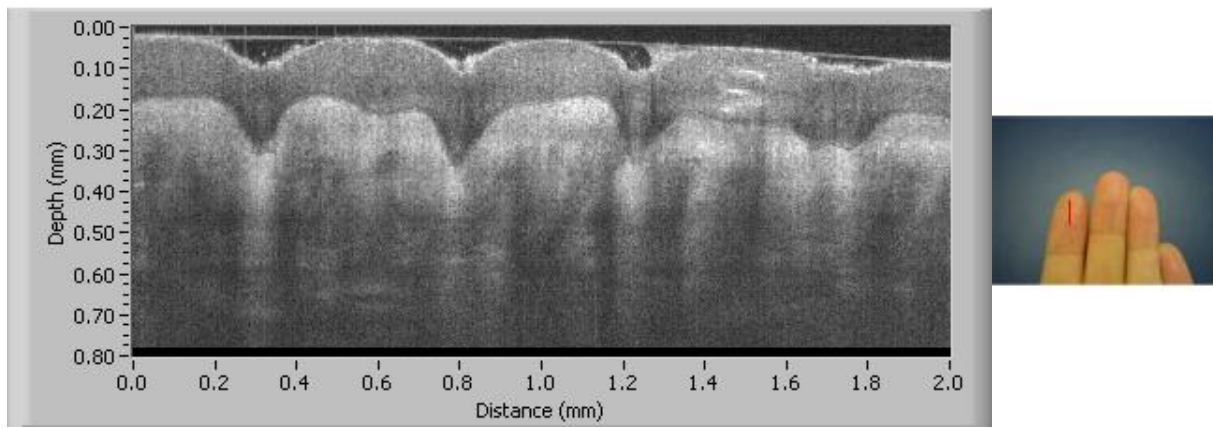


Figure 4.10: Cross-sectional image of *Xenopus Laevis* acquired (a) with fixed focus at 400 μm below the sample surface; (b) with dynamic focusing every 100 μm for 10 zones



(a)



(b)

Figure 4.11: *In vivo* depth cross-sections with a 2 mm lateral extent, imaged in 8 zones in the region of (a) the finger nail fold and (b) the finger tip of the palm. Images acquired along the red line shown on the right.

Finally, *in vivo* and *ex vivo* contact imaging was conducted on skin tissue with immersion in glycerol. Fig. 4.11 shows $2 \times 0.8 \text{ mm}^2$ sections of a human nail fold and a human fingertip acquired *in vivo* using dynamic focusing in GD-OCM. The data was acquired at a $1 \mu\text{m}$ lateral sampling interval with 8 C-zones. Fig. 4.12 shows a $2 \times 0.7 \text{ mm}^2$ depth section of a human finger joint acquired in 5 C-zones at a $1 \mu\text{m}$ lateral sampling interval using GD-OCM.

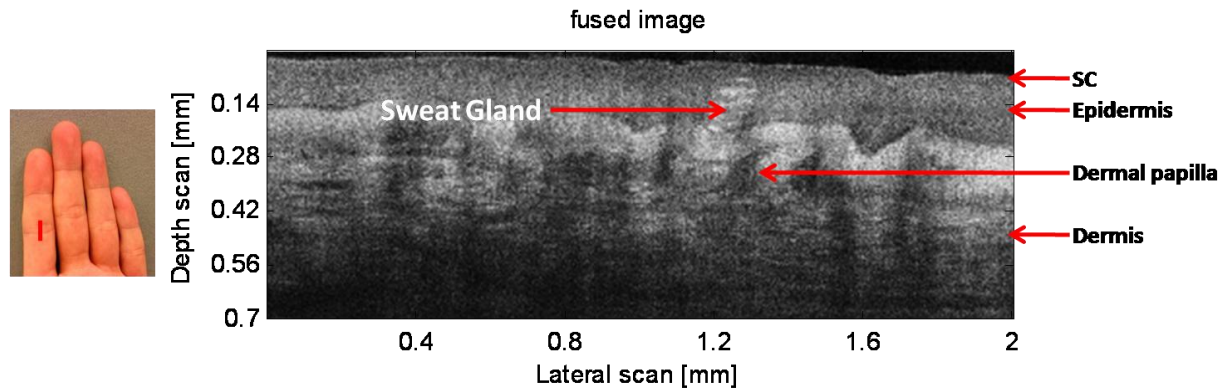


Figure 4.12: *Ex vivo* skin depth cross-section with a 2 mm lateral extent, imaged in 5 zones in the region of the finger joint. Image acquired along the red line shown on the left.

4.4.2 3D imaging using the dynamic focusing microscope

The next step in imaging using the dynamic focusing probe was 3D image acquisition. Early results of volumetric imaging of a $400 \mu\text{m}^3$ cubic cross-section of an African frog tadpole (*Xenopus Laevis*) are displayed in Fig. 4.13. The images are located near the gills of the tadpole and were acquired with a sampling interval of $1 \mu\text{m}$ between A-scans. In these preliminary tests, given the speed of the detector available, only 2 focusing zones were acquired -one near the surface of the sample and the other approximately $200 \mu\text{m}$ below the surface. Using GD-OCM as described in Chapter 3, a sliding window was applied to extract the in-focus portion from each acquired image. The window was chosen to be a flat top with linear transition at both edges. The center and the width of the windows were determined automatically and dynamically for each focus position. The filtered image zones were summed to form a high resolution with extended DOF image as shown earlier in Fig. 4.10. These preliminary results show invariant sub-cellular resolution throughout the depth and lateral cross-section validating the invariant performance of the probe in biological medium across FOV and depth.

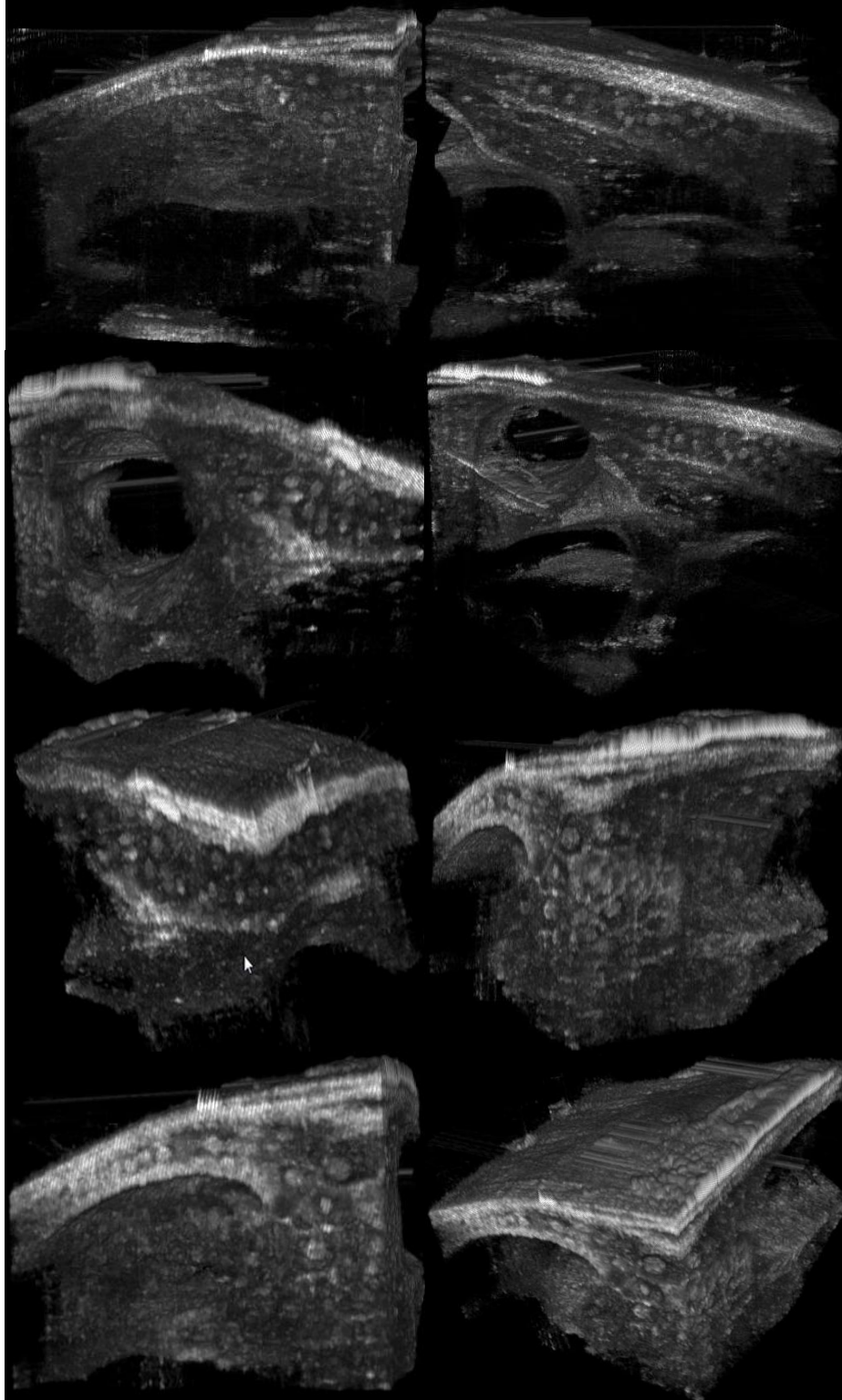


Figure 4.13: Perspective views of a $400 \mu\text{m}^3$ image volume acquired *ex vivo* in an African frog tadpole with 2 mm lateral extent and 2 depth zones in preliminary tests.

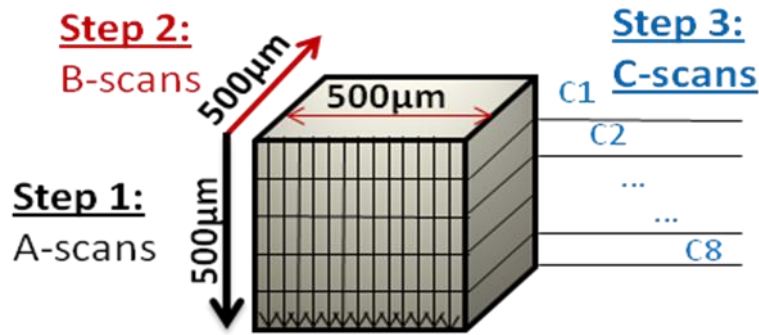


Figure. 4.14: Scanning mechanism for a $500 \mu\text{m}^3$ image volume in GD-OCM.

Fig. 4.14 is a schematic of the scanning mechanism for 3D imaging of a $400 \mu\text{m}^3$ cubic volume. The currently available detector in the laboratory (Ocean Optics HR 4000) limits the imaging speed to 12 seconds per B-scan. However, using a state-of-the-art high-speed detector such as a Sprint CMOS camera can enable scanning at the rate of 235,000 A-scans/sec and thus allow images with similar dimensions to those shown in Fig. 4.14 to be acquired with 8 focus zones separated by $60 \mu\text{m}$ (corresponding to the DOF of the microscope) within 8.5 seconds. This is equivalent to an imaging frame rate of approximately 59 frames/sec for an 8-zone, $500 \mu\text{m}^3$ volume. Thus, this technology will enable *in vivo* imaging and visualization in real-time at an invariant high resolution of $2 \mu\text{m}$ throughout the cubic volume.

CHAPTER 5- SUMMARY AND CONCLUSIONS

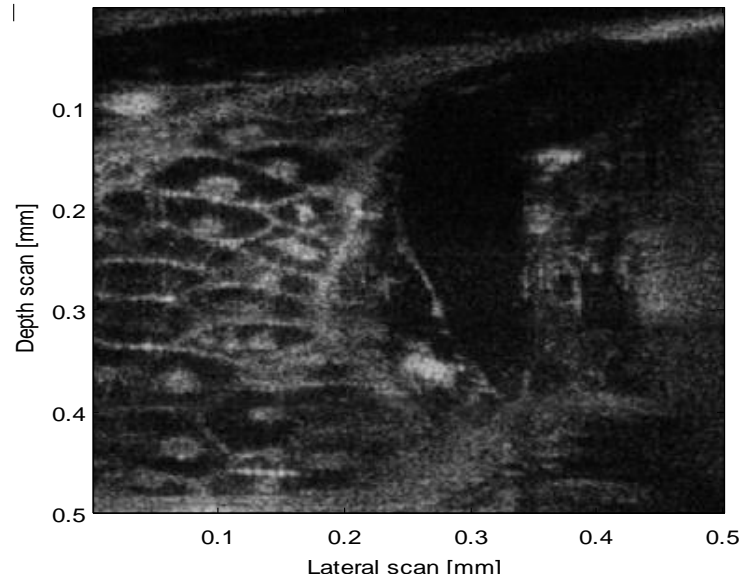
Tissue biopsy, involving excision of samples, is the current gold standard for skin cancer detection. A certified, reliable, non-invasive diagnostic instrument is being sought by the medical community that will provide faster, scar-free methods. Such a device would enhance patient compliance for optical skin cancer screening resulting in the earliest detection of abnormal pre-cancerous cells. In the introductory chapter, the structural properties of normal, pre-cancer and cancer tissue were reviewed. An overview of several imaging modalities that are currently being researched for non-invasive imaging of cancer such as confocal microscopy, spectroscopy, and high frequency ultrasound were presented.

Optical Coherence Microscopy (OCM), an imaging modality introduced in 1994, has gathered much interest in the biomedical research community because of its ability, like Optical Coherence Tomography (OCT), to reject a significant amount of multiply backscattered light thereby providing an imaging capability to a depth of a few mm in highly scattering media. Furthermore, OCM also provides micron-level axial resolution intrinsically through the coherence gating property of the light source, which is in this case a femtosecond laser. As we show here for the first time, it is in fact possible to create an FD-OCM (Fourier Domain OCM) based approach that simultaneously provides sub-cellular, micron-level axial and lateral resolution.

OCM shows great promise for non-invasive micron-scale volumetric imaging and has demonstrated the ability to image microscopic structures in biological tissues at sub 10 μm

resolution and at depths beyond the scope of confocal microscopy. Early stages of carcinoma occur in the upper layers of skin, approximately at depths of less than 1 mm. Therefore, if structural changes in the skin can be identified at the sub-cellular level during early screening using OCM, it would dramatically increase the chances of a permanent cure for both melanoma and non-melanoma cases. The main focus of this research, which was accomplished, was to achieve sub-cellular resolution through a substantial imaging volume, approaching a 2 mm cube using OCM.

The research presented here accomplished three major steps forward towards developing an OCM system that could be introduced in a clinical environment for noninvasive skin cancer detection. First, an emerging technology, liquid lenses, was successfully integrated into an OCM system to enable focusing through the 2 mm depth at video data rates with no moving parts. Simultaneously, a custom microscope optical design was created that increases the resolution that can be achieved with a liquid lens system (which restricts the maximum aperture to 2-3 mm) by a full order of magnitude, creating for the first time a FD-OCM with micron class sub-cellular lateral resolution. Third, this new, state-of-the-art instrumentation designed for data collection was integrated with a Gabor domain image processing algorithm to provide volumetric imaging cubes over a 2 mm cube in real-time. These three major improvements in the technology were successfully integrated into a working system that was then used to provide the sub-cellular 3-D imagery shown here.



The first goal for this research, which is ultimately aimed at a clinical instrument, is to get the technology off of the moving stages used in the original research. The first step in this process was to introduce a dynamic focusing capability into an OCM microscope involving no axially moving parts. While the axial coherence gate eliminates contrast reducing backscatter it must be registered with the OCM imagery so that the axial region that is in focus is registered with the coherence gate and then both must be scanned through the depth of the tissue at video rates, ideally with invariant resolution. The design study that supports this step was presented in Chapter 3. A preliminary feasibility investigation of a dynamic focusing 10X microscope using a liquid crystal lens to achieve a 2 μm lateral resolution was pursued initially. Owing to the speed restrictions imposed by the required diameter (~ 3 mm) of the liquid crystal lens design, this design did not proceed to fabrication. Following this feasibility analysis, we investigated the application of an electro-wetting liquid lens based dynamic focusing microscope. With this design work, which used actual optical properties of the liquid lens (proprietary) provided by the manufacturer (Varioptic Inc.), we demonstrate that through the depth of focus we could accommodate both the changes in the aberration of the liquid lens and the variation in

aberrations with imaging depth (due to a non-collimated beam in the skin) over a 2 mm refocusing depth in a homogeneous sample of refractive index 1.4 that approximates that of skin.

OCM, like many technologies, has two conflicting needs, large depth of focus and high resolution. Previously, researchers have sacrificed lateral resolution for large depth of focus. By introducing dynamic focusing, the requirement for large depth of focus is greatly reduced, allowing for an increase in numerical aperture that leads to higher resolution. However, the mode selected for focusing, liquid lenses, imposes its own limits on NA (and FOV). Within the restrictions created by the physical dimensions of the liquid lens, we found that we could increase the NA to 0.2. As we demonstrated, this substantial advance is the key to achieving sub-cellular resolution in an FD-OCM system. By fully integrating the liquid lens into a custom microscope optical design, we have increased the resolution capabilities by a full order of magnitude.

Finally, to move from a data collecting instrument to a visualization tool for a clinical environment, we introduced a new image processing framework, called Gabor Domain OCM (GD-OCM). This is a new modality for image acquisition where a voltage-controlled dynamic focus microscope is utilized to acquire multiple depth cross-sections or B-scans of the sample in the spectral domain at different focal planes in depth (Rolland 2008). These images are then registered and their in-focus zones are extracted and fused using an automated Gabor domain image registration and fusion algorithm to provide full resolution images across the data cube in real-time. The principles of GD-OCM were outlined in Chapter 3.

In Chapter 4, experimental measurements of MTF for the fabricated dynamic focusing microscope were shown that corroborate the theoretical predictions of lateral resolution with

greater than 20% contrast at 250 lp/mm, which is invariant across the 3D volume. The DOF of the microscope was measured and quantified to be 60 μm , determined based on a measured MTF contrast of 20% at 250 lp/mm. Measurement of resolution in scattering media with properties similar to skin, such as a 25 vol% solution of 3.5% fat milk, was reported. Results show that a 2 μm resolution is maintained up to a depth of 1 mm. The refocus time over the full range of focus of the liquid lens is approximately 100 ms. When combined with currently available technology of scanners (speeds order of kHz) and detectors (commercial state-of-the-art at 235,000 Ascans/sec with a Sprint CMOS camera), it can be concluded from this research that it is indeed possible to obtain a high resolution (lateral and axial) 3D image at a fast imaging speed of 59 frames/sec for obtaining a 500 μm^3 sample volume using OCM. It was also demonstrated that in the GD-OCM methodology, high resolution microscopy can be combined with OCM in the spectral domain. Biological imaging at the sub-cellular level was demonstrated in tadpole and skin samples, where 2D cross-sections of the samples were taken at regular intervals of focus. The data obtained from the dynamic focusing OCM microscope was then registered, sectioned in depth, and fused in the Gabor domain using an automatic data processing algorithm developed in the laboratory.

The significance of this research work is that it provides a clear, experimentally verified path toward the development of a clinical working solution for non-invasive skin cancer detection using OCM. By combining custom optical design and engineering of an OCM head to integrate the emerging liquid lens technology in such a way as to achieve simultaneously axial and lateral resolution at the sub-cellular level with a image processing and fusion algorithm that operates in real-time, all of the components needed for a clinical system have been demonstrated. The next step will be a clinical trial of this new technology.

REFERENCES

- Aguirre, A. D., P. Hsiung, et al. (2003). "High-resolution optical coherence microscopy for high-speed, in vivo cellular imaging." *Optics Letters*. **28**(21): 2064-2066.
- Akcay, C., P. Parrein, et al. (2002). "Estimation of longitudinal resolution in optical coherence imaging." *Appl. Opt.* **41**(25): 5256-5262.
- Alcamo, I. E. and B. Krumhardt (2004). Anatomy and Physiology the Easy Way, Barron's Educational Series.
- Alexander, H. and D. L. Miller (1979). "Determining Skin Thickness with Pulsed Ultra Sound." *Journal of Investigative Dermatology*. **72**(1): 17-19.
- Anderson, R. R. (1991). "Polarized light examination and photography of the skin." *Archives of Dermatology*. **127**(7): 1000-1005.
- Argenziano, G., G. Fabbrocini, et al. (1999). "Clinical and dermatoscopic criteria for the preoperative evaluation of cutaneous melanoma thickness." *J Am Acad Dermatol*. **40**(1): 61-8.
- Argenziano, G., H. P. Soyer, et al. (2002). "Impact of dermoscopy on the clinical management of pigmented skin lesions." *Clinics in Dermatology*. **20**(3): 200-202.
- Arnone, D. D., C. M. Ciesla, et al. (1999). "Applications of terahertz (THz) technology to medical imaging." *Proceedings of SPIE*. **3828**: 209.
- Asawanonda, P. and C. R. Taylor (1999). "Wood's light in dermatology." *Int J Dermatol*. **38**(11): 801-7.
- Aspres, N., I. B. Egerton, et al. (2003). "Imaging the skin." *Australasian Journal of Dermatology*. **44**(1): 19-27.
- Atkinson, L. G., S. N. Houde-Walter, et al. (1982). "Design of a Gradient-Index Photographic Objective." *Applied Optics*. **21**(6): 993-998.
- Backman, V., R. Gurjar, et al. (1999). "Polarized light scattering spectroscopy for quantitative measurement of epithelial cellular structures in situ." *Selected Topics in Quantum Electronics, IEEE Journal of*. **5**(4): 1019-1026.
- Barr, R. J. (1984). "Cutaneous cytology." *Journal of the American Academy of Dermatology*. **10**(2): 163-180.
- Barr, R. J., G. M. White, et al. (1991). "Scanning Acoustic Microscopy of Neoplastic and Inflammatory Cutaneous Tissue Specimens." *J Investig Dermatol*. **96**(1): 38-42.

- Barrett, H. H. and K. J. Myers (2004). Mixed Representations. Foundations of Image Science. B. E. Saleh. Hoboken, NJ, Wiley Interscience.
- Berge, B. and J. Peseux (2000). "Variable focal lens controlled by an external voltage: An application of electrowetting." *The European Physical Journal E-Soft Matter*. **3**(2): 159-163.
- Bigio, I. J., S. G. Bown, et al. (2000). "Diagnosis of breast cancer using elastic-scattering spectroscopy: preliminary clinical results." *Journal of Biomedical Optics*. **5**: 221.
- Bigio, I. J. and J. R. Mourant (1997). "Ultraviolet and visible spectroscopies for tissue diagnostics: fluorescence spectroscopy and elastic-scattering spectroscopy." *Phys. Med. Biol.* **42**(5): 803–814.
- Binder, M., M. Puespoeck-Schwarz, et al. (1997). "Epiluminescence microscopy of small pigmented skin lesions: short-term formal training improves the diagnostic performance of dermatologists." *J Am Acad Dermatol*. **36**(2 Pt 1): 197-202.
- Binder, M., M. Schwarz, et al. (1995). "Epiluminescence microscopy. A useful tool for the diagnosis of pigmented skin lesions for formally trained dermatologists." *Archives of Dermatology*. **131**(3): 286-291.
- Bittoun, J., H. Saint-Jalmes, et al. (1990). "In vivo high-resolution MR imaging of the skin in a whole-body system at 1.5 T." *Radiology*. **176**(2): 457-60.
- Boppart, S. A., B. E. Bouma, et al. (1998). "In vivo cellular optical coherence tomography imaging." *Nature Medicine*. **4**(7): 861-865.
- Bordenave, E., E. Abraham, et al. (2002). "Wide-field optical coherence tomography: imaging of biological tissues." *Appl. Opt.* **41**(10).
- Bouma, B. E. and G. J. Tearney (2002). Handbook of Optical Coherence Tomography. New York, Marcel Dekker Inc.
- Brancaleon, L., A. J. Durkin, et al. (2001). "In vivo Fluorescence Spectroscopy of Nonmelanoma Skin Cancer." *Photochemistry and Photobiology*. **73**(2): 178-183.
- Brenan, C. J. H. (1996). "Volumetric Raman Microscopy Through Turbid Medium." *Journal of Raman Spectroscopy*. **27**: 561-570.
- Breslin, T. M., F. Xu, et al. (2004). Autofluorescence and Diffuse Reflectance Properties of Malignant and Benign Breast Tissues, *Soc Surgical Oncol*. **11**: 65-70.
- Breslow, N. E. and N. E. Day (1987). "Statistical methods in cancer research. Volume II--The design and analysis of cohort studies." *IARC Sci Publ*. **82**: 1-406.

- Brezinski, M. E. and J. G. Fujimoto (1999). "Optical coherence tomography: high-resolution imaging in nontransparent tissue." *Selected Topics in Quantum Electronics, IEEE Journal of.* **5**(4): 1185-1192.
- Brezinski, M. E., G. J. Tearney, et al. (1996). "Optical Coherence Tomography for Optical Biopsy Properties and Demonstration of Vascular Pathology." *Circulation.* **93**(6): 1206-1213.
- Broer, N. M., T. Liesenhoff, et al. (2004). "Laser-induced Fluorescence Spectroscopy for Real-Time Tissue Differentiation." *Medical Laser Application.* **19**(1): 45-53.
- Busam, K. J., K. Hester, et al. (2001). Detection of Clinically Amelanotic Malignant Melanoma and Assessment of Its Margins by In Vivo Confocal Scanning Laser Microscopy, *Am Med Assoc.* **137**: 923-929.
- Carmeliet, P. and R. K. Jain (2000). "Angiogenesis in cancer and other diseases." *Nature.* **407**(6801): 249-257.
- Caspers, P. J., G. W. Lucassen, et al. (2003). "Combined In Vivo Confocal Raman Spectroscopy and Confocal Microscopy of Human Skin." *Biophysical Journal.* **85**(1): 572-580.
- Chinn, S. R., E. A. Swanson, et al. (1997). "Optical coherence tomography using a frequency-tunable optical source." *Optics Letters.* **22**(5): 340.
- Chung, A., S. Wachsmann-Hogiu, et al. (2005). "Advanced Optical Imaging Requiring No Contrast Agents—A New Armamentarium for Medicine and Surgery." *Current Surgery.* **62**(3): 365-370.
- Cole, B. E., R. M. Woodward, et al. (2001). "Terahertz imaging and spectroscopy of human skin in vivo." *Proceedings of SPIE.* **4276**: 1.
- Corcuff, P. and J. L. Leveque (1993). "In vivo vision of the human skin with the tandem scanning microscope." *Dermatology.* **186**(1): 50-4.
- Cotton, S. (1998). A non-invasive imaging system for assisting in the diagnosis of malignant melanoma, PhD Thesis, School of Computer Science, The University of Birmingham.
- Crupi, V., D. De Domenico, et al. (2001). "FT-IR spectroscopy study on cutaneous neoplasie." *Journal of Molecular Structure.* **563**: 115-118.
- Danaei, G., S. Vander Hoorn, et al. (2005). "Causes of cancer in the world: comparative risk assessment of nine behavioural and environmental risk factors." *The Lancet.* **366**(9499): 1784-1793.
- Demos, S. G. and R. R. Alfano (1997). "Optical polarization imaging." *Appl. Opt.* **36**(36): 150-55.

- Denk, W., J. H. Strickler, et al. (1990). "2-photon laser scanning fluorescence microscopy." *Science*. **248**(4951): 73-76.
- Derrick, E. K., R. Smith, et al. (1994). "The use of cytology in the diagnosis of basal cell carcinoma." *British journal of dermatology*(1951). **130**(5): 561-563.
- Diem, M., S. Boydston-White, et al. (1999). "Infrared Spectroscopy of Cells and Tissues: Shining Light onto a novel Subject."
- Diem, M., M. Romeo, et al. (2004). "A decade of vibrational micro-spectroscopy of human cells and tissue (1994–2004)." *The Analyst*. **129**(10): 880-885.
- Diffey, B. L. (1983). "Mathematical model for ultraviolet optics in skin." *Physics in Medicine & Biology*. **28**(6): 647-657.
- Ding, H., J. Q. Lu, et al. (2006). "Refractive indices of human skin tissues at eight wavelengths and estimated dispersion relations between 300 and 1600 nm." *Physics in Medicine and Biology*. **51**(6): 1479-1490.
- Ding, Z., H. Ren, et al. (2002). "High-resolution optical coherence tomography over a large depth range with an axicon lens." *Optics Letters*. **27**(4): 243-245.
- Divetia, A., T. H. Hsieh, et al. (2005). "Dynamically focused optical coherence tomography for endoscopic applications." *Applied Physics Letters*. **86**: 103902.
- Drexler, W. (2004). "Ultrahigh-resolution optical coherence tomography." *Journal of Biomedical Optics*. **9**: 47.
- Drexler, W., U. Morgner, et al. (1999). "In vivo ultrahigh-resolution optical coherence tomography." *Optics Letters*. **24**(17): 1221-1223.
- Edwards, E. A. and D. Q. (1939). "The pigments and color of living human skin." *American journal of Anatomy*. **65**: 1-33.
- Edwards, H. G. M., A. C. Williams, et al. (1995). "Potential applications of FT-Raman spectroscopy for dermatological diagnostics." *Journal of Molecular Structure*. **347**: 379-387.
- Eigensee, A., G. Haeusler, et al. (1996). A new method of short-coherence-interferometry in human skin (in vivo) and in solid volume scatterers. European biomedical optics week. Vienna, Proceedings of SPIE. **2925**: 169-178.
- Eigenwillig, C. M., W. Wieser, et al. (2009). "Subharmonic Fourier domain mode locking." *Optics Letters*. **34**(6): 725-727.

- El Gammal, S., C. El Gammal, et al. (1999). "Sonography of the Skin at 100 MHz Enables In Vivo Visualization of Stratum Corneum and Viable Epidermis in Palmar Skin and Psoriatic Plaques." *Journal of Investigative Dermatology*. **113**: 821-829.
- El Gammal, S., R. Hartwig, et al. (1996). "Improved Resolution of Magnetic Resonance Microscopy in Examination of Skin Tumors." *Journal of Investigative Dermatology*. **106**(6): 1287-1292.
- Elbaum, M., A. W. Kopf, et al. (2001). "Automatic differentiation of melanoma from melanocytic nevi with multispectral digital dermoscopy: a feasibility study." *J Am Acad Dermatol*. **44**(2): 207-18.
- Elias, P. M. and M. L. K. Williams. (2008). "Structure and Function of the Stratum Corneum." from <http://www.aad.org/education/students/StratumCorneum.htm>.
- Erhard, H., F. J. Rietveld, et al. (1997). "Transition of horizontal to vertical growth phase melanoma is accompanied by induction of vascular endothelial growth factor expression and angiogenesis." *Melanoma Res*. **7**(2): S19-26.
- Evan, G. I. and K. H. Vousden (2001). "Proliferation, cell cycle and apoptosis in cancer." *Nature*. **411**(6835): 342-348.
- Farina, B., C. Bartoli, et al. (2000). "Multispectral imaging approach in the diagnosis of cutaneous melanoma: potentiality and limits." *Phys Med Biol*. **45**(5): 1243-54.
- Farrell, T. J., M. S. Patterson, et al. (1992). "A diffusion theory model of spatially resolved, steady-state diffuse reflectance for the noninvasive determination of tissue optical properties in vivo." *Medical Physics*. **19**: 879.
- Fendel, S. and B. Schrader (1998). "Investigation of skin and skin lesions by NIR-FT-Raman spectroscopy." *Fresenius' Journal of Analytical Chemistry*. **360**(5): 609-613.
- Fercher, A. F., C. K. Hitzenberger, et al. (1995). "Measurement of intraocular distances by backscattering spectral interferometry." *Optics Communications*. **117**(1-2): 43-48.
- Fitzpatrick, T. B., A. R. Rhodes, et al. (1988). "Primary malignant melanoma of the skin: the call for action to identify persons at risk; to discover precursor lesions; to detect early melanomas." *Pigment Cell*. **9**: 110-117.
- Flournoy, P. A., R. W. McClure, et al. (1972). "White-light interferometric thickness gauge." *Appl. Opt.* **11**(9): 1907-1915.
- Fornage, B. D., M. H. McGavran, et al. (1993). "Imaging of the skin with 20-MHz US." *Radiology*. **189**(1): 69-76.
- Frank, C. J., R. L. McCreery, et al. (1995). "Raman Spectroscopy of Normal and Diseased Human Breast Tissues." *Analytical Chemistry*. **67**(5): 777-783.

- Gallagher, R. P., B. Ma, et al. (1990). "Trends in basal cell carcinoma, squamous cell carcinoma, and melanoma of the skin from 1973 through 1987." *J Am Acad Dermatol.* **23**(3 Pt 1): 413-21.
- Gambichler, T., R. Matip, et al. (2006). "In vivo data of epidermal thickness evaluated by optical coherence tomography: Effects of age, gender, skin type, and anatomic site." *Journal of Dermatological Science.* **44**(3): 145-152.
- Georgakoudi, I., B. C. Jacobson, et al. (2001). "Fluorescence, Reflectance, and Light-Scattering Spectroscopy for Evaluating Dysplasia in Patients With Barrett's Esophagus." *Gastroenterology.* **120**(7): 1620-1629.
- George, N. and W. Chi (2003). "Extended depth of field using a logarithmic asphere." *J. Opt. A, Pure Appl. Opt.* **5**: 157-163.
- Gladkova, N. D., G. A. Petrova, et al. (2000). "In vivo optical coherence tomography imaging of human skin: norm and pathology." *Skin Research and Technology.* **6**(1): 6-16.
- Gniadecka, M. and G. B. E. Jemec (1998). "Quantitative evaluation of chronological ageing and photoageing in vivo: studies on skin echogenicity and thickness." *British Journal of Dermatology.* **139**: 815-821.
- Gniadecka, M., P. A. Philipsen, et al. (2004). "Melanoma Diagnosis by Raman Spectroscopy and Neural Networks: Structure Alterations in Proteins and Lipids in Intact Cancer Tissue." *Journal of Investigative Dermatology.* **122**: 443-449.
- Gniadecka, M., H. C. Wulf, et al. (1997a). "Distinctive Molecular Abnormalities in Benign and Malignant Skin Lesions: Studies by Raman Spectroscopy." *Photochemistry and Photobiology.* **66**(4): 418-423.
- Gniadecka, M., H. C. Wulf, et al. (1997b). "Diagnosis of Basal Cell Carcinoma by Raman Spectroscopy." *Journal of Raman Spectroscopy.* **28**(23): 125-129.
- Gremlich, H. U. and B. Yan (2001). Infrared and Raman Spectroscopy of Biological Materials, Marcel Dekker.
- Gurjar, R. S., V. Backman, et al. (2001). "Imaging human epithelial properties with polarized light-scattering spectroscopy." *Nat. Med.* **7**(11): 1245–1248.
- Hanahan, D. and R. A. Weinberg (2000). "The Hallmarks of Cancer." *Cell.* **100**(1): 57-70.
- Häusler, G. and M. W. Lindner (1998). "“Coherence Radar” and “Spectral Radar”—New Tools for Dermatological Diagnosis." *Journal of Biomedical Optics.* **3**: 21.
- Hee, M. R., J. A. Izatt, et al. (1995). "Optical coherence tomography of the human retina." *Archives of Ophthalmology.* **113**(3): 325-332.

- Hill, C. R., J. C. Bamber, et al. (2004). Methodology for Clinical Investigation. Physical Principles of Medical Ultrasonics. C. R. Hill, J. C. Bamber and G. R. Haar, John Wiley & Sons.
- Hoffmann, K., M. Happe, et al. (1999). "Ranking of 20 MHz sonography of malignant melanoma and pigmented lesions in routine diagnosis." *Ultraschall Med.* **20**(3): 104-9.
- Hoffmann, K., M. Stuucker, et al. (1994). "Twenty MHz B-scan sonography for visualization and skin thickness measurement of human skin." *Journal of the European Academy of Dermatology & Venereology.* **3**(3): 302-313.
- Holman, H. Y. N., M. C. Martin, et al. (2003). "Synchrotron-Based FTIR Spectromicroscopy: Cytotoxicity and Heating Considerations." *Journal of Biological Physics.* **29**(2): 275-286.
- Holmes, J., S. Hattersley, et al. (2008). Multi-channel Fourier domain OCT system with superior lateral resolution for biomedical applications. Coherence Domain Optical Methods and Optical Coherence Tomography in Biomedicine XII. J. A. Izatt, J. G. Fujimoto and V. V. Tuchin. Kent, UK, Proceedings of SPIE. **6847**: 684700.
- Huang, D., E. A. Swanson, et al. (1991). "Optical coherence tomography." *Science.* **254**(5035): 1178-1181.
- Huber, R., D. C. Adler, et al. (2006). "Buffered Fourier domain mode locking: unidirectional swept laser sources for optical coherence tomography imaging at 370,000 lines/s." *Optics Letters.* **31**(20): 2975-2977.
- Huber, R., M. Wojtkowski, et al. (2005). "Three-dimensional and C-mode OCT imaging with a compact, frequency swept laser source at 1300 nm." *Optics Express.* **13**(26): 10523-10538.
- Huzaira, M., F. Rius, et al. (2001). "Topographic variations in normal skin, as viewed by in vivo reflectance confocal microscopy." *J Invest Dermatol.* **116**(6): 846-52.
- Hyde, J. S., A. Jesmanowicz, et al. (1987). "Surface coil for MR imaging of the skin." *Magn Reson Med.* **5**(5): 456-61.
- Izatt, J. A., M. R. Hee, et al. (1994). "Optical coherence microscopy in scattering media." *Optics Letters.* **19**(8): 590-592.
- Jacques, S. L., J. C. Ramella-Roman, et al. (2002). "Imaging skin pathology with polarized light." *Journal of Biomedical Optics.* **7**: 329.
- Jacques, S. L., J. R. Roman, et al. (2000). "Imaging superficial tissues with polarized light." *Lasers in Surgery and Medicine.* **26**(2): 119-129.
- Jemal, A., R. Siegel, et al. (2008). "Cancer statistics, 2008." *CA Cancer J Clin.* **58**(2): 71-96.

- Jeon, M. Y., J. Zhang, et al. (2008). "High-speed and wide bandwidth Fourier domain mode-locked wavelength swept laser with multiple SOAs." *Optics Express*. **16**(4): 2547-2554.
- Junqueira, L. C. U. and J. Carneiro (2005). Basic Histology: Text & Atlas, McGraw-Hill.
- Kino, G. S. and S. S. C. Chim (1990). "Mirau correlation microscope." *Appl. Opt.* **29**(26): 3775-3783.
- Klaessens, J., J. C. W. Hopman, et al. (2008). "A modified algorithm for continuous wave near infrared spectroscopy applied to in-vivo animal experiments and on human skin." *Proceedings of SPIE*. **6848**: 68480A.
- Knollman, G. C., J. L. S. Bellin, et al. (1971). "Variable-Focus Liquid-Filled Hydroacoustic Lens." *The Journal of the Acoustical Society of America*. **49**: 253.
- Knuettel, A. R., J. M. Schmitt, et al. (1993). Spatial localization using interfering photon density waves: contrast enhancement and limitations. Photon Migration and Imaging in Random Media and Tissues, Proceedings of SPIE. C. Britton and R. A. Robert. Los Angeles, USA. **1888**: 322-333.
- Koh, H. K., R. A. Lew, et al. (1989). "Screening for melanoma/skin cancer: theoretic and practical considerations." *J Am Acad Dermatol*. **20**(2 Pt 1): 159-72.
- Kollias, N., R. Gillies, et al. (1998). "Endogenous Skin Fluorescence Includes Bands that may Serve as Quantitative Markers of Aging and Photoaging." *Journal of Investigative Dermatology*. **111**(5): 776-780.
- Kollias, N. and G. N. Stamatias (2002). "Optical Non-Invasive Approaches to Diagnosis of Skin Diseases." *Journal of Investigative Dermatology*. **7**: 64-75.
- Kopf, A. W., M. Mintzis, et al. (1975). "Diagnostic accuracy in malignant melanoma." *Archives of Dermatology*. **111**(10): 1291-1292.
- Korde, V. R., G. T. Bonnema, et al. (2007). "Using optical coherence tomography to evaluate skin sun damage and precancer." *Lasers Surg Med*. **39**(9): 687-95.
- Krupenkin, T., S. Yang, et al. (2003). "Tunable liquid microlens." *Applied Physics Letters*. **82**: 316.
- Kuiper, S., B. H. Hendriks, et al. (2004a). Variable-focus liquid lens for portable applications. Current Developments in Lens Design and Optical Engineering V. Bellingham, WA, Proceedings of SPIE. **5523**: 100-109.
- Kuiper, S., B. H. Hendriks, et al. (2004b). "Variable-focus liquid lens for portable applications." SPIE.

- Kuiper, S. and B. H. W. Hendriks (2004c). "Variable-focus liquid lens for miniature cameras." *Applied Physics Letters*. **85**: 1128.
- Kumar, V., A. K. Abbas, et al. (2005). Robbins and Cotran pathologic basis of disease, Elsevier Saunders, Philadelphia.
- Langley, R. G., M. Rajadhyaksha, et al. (2001). "Confocal scanning laser microscopy of benign and malignant melanocytic skin lesions in vivo." *J Am Acad Dermatol*. **45**(3): 365-76.
- Lasagni, C. and S. Seidenari (1995). "A study on 162 subjects." *Skin Research and Technology*. **1**(2): 81-85.
- Lassau, N., A. Spatz, et al. (1997). "Value of high-frequency US for preoperative assessment of skin tumors." *Radiographics*. **17**(6): 1559-65.
- Lee, K. S. (2008a). Extended focus range high resolution endoscopic Optical Coherence Tomography. CREOL - College of Optics and Photonics. Orlando, University of Central Florida. **PhD**.
- Lee, K. S., A. C. Akcay, et al. (2005). "Dispersion control with a Fourier-domain optical delay line in a fiber-optic imaging interferometer." *Applied Optics*. **44**(19): 4009-4022.
- Lee, K. S. and J. P. Rolland (2008b). "Bessel beam spectral-domain high-resolution optical coherence tomography with micro-optic axicon providing extended focusing range." *Optics Letters*. **33**(15): 1696-1698.
- Lexer, F., C. K. Hitzenberger, et al. (1999). "Dynamic coherent focus OCT with depth-independent transversal resolution." *Journal of Modern Optics*. **46**(3): 541-553.
- Li, T., A. Wang, et al. (1995). "White-light scanning fiber Michelson interferometer for absolute position-distance measurement." *Opt. Lett.* **20**(7): 785-787.
- Lindner, M. W. (2002). Spectral Radar: Optical Coherence Tomography in the Fourier Domain. Handook of Optical Coherence Tomography. M. W. Lindner, F. Andretzky, F. Kieseletter and G. Häusler. Boston, MA, Marcel Dekker.
- Lodha, S., S. Sagar, et al. (2008). "Discordance in the histopathologic diagnosis of difficult melanocytic neoplasms in the clinical setting." *Journal of Cutaneous Pathology*. **35**(4): 349-352.
- Mahajan, V. N. (2004). Optical Imaging and Aberrations. Bellingham, USA, SPIE Press.
- Marbach, R. and H. M. Heise (1995). "Optical Diffuse Reflectance Accessory for Measurements of Skin Tissue by Near-Infrared Spectroscopy." *Applied Optics*. **34**(4): 610-621.

- Marchesini, R., M. Brambilla, et al. (1991). "In vivo spectrophotometric evaluation of neoplastic and non-neoplastic skin pigmented lesions. I, Reflectance measurements." *Photochemistry and Photobiology*. **53**(1): 77-84.
- Marchesini, R., N. Cascinelli, et al. (1992). "In vivo spectrophotometric evaluation of neoplastic and non-neoplastic skin pigmented lesions. II: Discriminant analysis between nevus and melanoma." *Photochemistry and Photobiology*. **55**(4): 515-522.
- Marchesini, R., S. Tomatis, et al. (1995). "In vivo spectrophotometric evaluation of neoplastic and non-neoplastic skin pigmented lesions. III. CCD camera-based reflectance imaging." *Photochemistry and Photobiology*. **62**(1): 151-154.
- Marghoob, A. A., L. D. Swindle, et al. (2003). "Instruments and new technologies for the in vivo diagnosis of melanoma." *Journal of the American Academy of Dermatology*. **49**(5): 777-797.
- Marks, D. L., T. S. Ralston, et al. (2007). "Inverse scattering for frequency-scanned full-field optical coherence tomography." *Journal of the Optical Society of America A*. **24**(4): 1034-1041.
- Marks, D. L., T. S. Ralston, et al. (2006). "Inverse scattering for rotationally scanned optical coherence tomography." *Journal of the Optical Society of America A*. **23**(10): 2433-2439.
- Marks, R. (1995). "The epidemiology of non-melanoma skin cancer: who, why and what can we do about it." *J Dermatol*. **22**(11): 853-7.
- Marshall, R. J. (1976). "Infrared and ultraviolet photography in a study of the selective absorption of radiation by pigmented lesions of skin." *Med Biol Illus*. **26**(2): 71-84.
- Masters, B. R., P. T. C. So, et al. (1998). "Multiphoton Excitation Microscopy of In Vivo Human Skin: Functional and Morphological Optical Biopsy Based on Three-Dimensional Imaging, Lifetime Measurements and Fluorescence Spectroscopy a." *Annals of the New York Academy of Sciences*. **838**(1 ADVANCES IN OPTICAL BIOPSY AND OPTICAL MAMMOGRAPHYa): 58-67.
- McCance, K. L. and S. E. Huether (2006). *Pathophysiology: The Biologic Basis for Disease in Adults and Children*, StLouis, Elsevier Mosby.
- McGovern, T. W. and D. J. Leffell. (2008). "Actinic Keratoses and Non-Melanoma Skin Cancer." from http://www.aad.org/education/students/ak_nonmelanoma.htm.
- McMasters, K. M., V. K. Sondak, et al. (1999). "Recent Advances in Melanoma Staging and Therapy." *Annals of Surgical Oncology*. **6**(5): 467-475.
- Mendelsohn, R., H. C. Chen, et al. (2003). "Infrared microspectroscopic imaging maps the spatial distribution of exogenous molecules in skin." *Journal of Biomedical Optics*. **8**: 185.

- Menzies, S. W. (2003). An Atlas of Surface Microscopy of Pigmented Skin Lesions: Dermoscopy, McGraw-Hill Book Company Australia.
- Mirabal, Y. N., S. K. Chang, et al. (2002). "Reflectance spectroscopy for in vivo detection of cervical precancer." *Journal of Biomedical Optics*. **7**: 587.
- Mirabella, F. M. (1998). Modern Techniques in Applied Molecular Spectroscopy, Wiley-Interscience.
- Mogensen, M. and G. B. E. Jemec (2007). "Diagnosis of nonmelanoma skin cancer/keratinocyte carcinoma: a review of diagnostic accuracy of nonmelanoma skin cancer diagnostic tests and technologies." *Dermatologic Surgery*. **33**(10): 1158-1174.
- Moncrieff, M. (2002). "A simple classification of the resolution and depth of imaging systems for pigmented skin lesions." *Melanoma Research*. **12**(2): 155.
- Moran, P. M., S. Dharmatilleke, et al. (2006). "Fluidic lenses with variable focal length." *Applied Physics Letters*. **88**: 041120.
- Moss, D. A., M. Keese, et al. (2005). "IR microspectroscopy of live cells." *Vibrational Spectroscopy*. **38**(1-2): 185-191.
- Mourant, J. R., I. J. Bigio, et al. (1995). "Spectroscopic diagnosis of bladder cancer with elastic light scattering." *Lasers Surg Med*. **17**(4): 350-7.
- Muccini, J. A., N. Kollias, et al. (1995). "Polarized light photography in the evaluation of photoaging." *J Am Acad Dermatol*. **33**(5 Pt 1): 765-9.
- Murali, S., P. Meemon, et al. (2009a). "Skin imaging with a liquid-lens enabled dynamic focusing OCM microscope." *Submission in Progress*.
- Murali, S. and J. Rolland (2006). "Dynamic-focusing microscope objective for optical coherence tomography." Vancouver, BC, Canada, International Society for Optical Engineering, Bellingham WA, WA 98227-0010, United States.
- Murali, S. and J. Rolland (2007a). "Dynamic focusing imaging probe for optical coherence microscopy." *Lasers and Electro-Optics Society, 2007. LEOS 2007. The 20th Annual Meeting of the IEEE*.
- Murali, S. and J. Rolland (2007b). "Invariant high resolution optical skin imaging." *Proceedings of SPIE*.
- Murali, S., K. P. Thompson, et al. (2009b). "Three-dimensional adaptive microscopy using embedded liquid lens." *Optics Letters*. **34**(2): 145-147.
- Murray, A. E. (1988). "A routine method for the quantification of physical change in melanocytic naevi using digital image processing." *J Audiov Media Med*. **11**(2): 52-7.

- Nordstrom, R. J., L. Burke, et al. (2001). "Identification of cervical intraepithelial neoplasia(CIN) using UV-excited fluorescence and diffuse-reflectance tissue spectroscopy." *Lasers in Surgery and Medicine*. **29**(2): 118-127.
- Nouveau-Richard, S., M. Monot, et al. (2004). "In vivo epidermal thickness measurement: ultrasound vs. confocal imaging." *Skin Research and Technology*. **10**(2): 136-140.
- Olsen, L. O., H. Takiwaki, et al. (1995). "High-frequency ultrasound characterization of normal skin. Skin thickness and echographic density of 22 anatomical sites." *Skin Research and Technology*. **1**(2): 74-80.
- Oram, Y., O. Turhan, et al. (1997). "Diagnostic value of cytology in basal cell and squamous cell carcinomas." *Int J Dermatol*. **36**(2): 156-7.
- Parivar, F., H. Hricak, et al. (1996). "Detection of locally recurrent prostate cancer after cryosurgery: evaluation by transrectal ultrasound, magnetic resonance imaging, and three-dimensional proton magnetic resonance spectroscopy." *Urology*. **48**(4): 594-9.
- Parrish, J. A. (1981). "New Concepts in Therapeutic Photomedicine; Photochemistry, Optical Targeting and the Therapeutic Window." *Journal of Investigative Dermatology*. **77**(1): 45-50.
- Perelman, L. T., V. Backman, et al. (1998). "Observation of Periodic Fine Structure in Reflectance from Biological Tissue: A New Technique for Measuring Nuclear Size Distribution." *Physical Review Letters*. **80**(3): 627-630.
- Perkins, W. D. (1986). "Fourier transform-infrared spectroscopy: Part I. Instrumentation (TICI)." *Journal of Chemical Education*. **63**(1): 6.
- Petrich, W. (2006). "MID-INFRARED AND RAMAN SPECTROSCOPY FOR MEDICAL DIAGNOSTICS?" *Shock*. **26**(4): 1.
- Physorg. (2004). "Philips' fluid Lenses Bring Things into Focus; Unique Variable-Focus With No Mechanical Moving Parts." Physorg - Technology, from <http://www.physorg.com/news308.html>.
- Poste, G. and I. J. Fidler (1980). "The pathogenesis of cancer metastasis." *Nature*. **283**(5743): 139-146.
- Povazay, B., K. Bizheva, et al. (2002). "Submicrometer axial resolution optical coherence tomography." *Optics Letters*. **27**(20): 1800-1802.
- Povazay, B., B. Hofer, et al. (2009). "In vivo frequency domain optical coherence tomography of the human retina at 800nm with up to 312,000 lines/s." *SPIE Photonics West*, San Jose, CA, SPIE Proceedings.

- Powell, C. R., G. Menon, et al. (2000). "Cytological examination of basal cell carcinoma-a useful tool for diagnosis." *Br J Dermatol.* **143**(57): 71.
- Qi, B., A. Phillip Himmer, et al. (2004). "Dynamic focus control in high-speed optical coherence tomography based on a microelectromechanical mirror." *Optics Communications.* **232**(1-6): 123-128.
- Querleux, B., S. Richard, et al. (1994). "In vivo hydration profile in skin layers by high-resolution magnetic resonance imaging." *Skin Pharmacol.* **7**(4): 210-6.
- Querleux, B., M. M. Yassine, et al. (1988). "Magnetic resonance imaging of the skin." *A comparison with the ultrasonic technique. Bioeng Skin.* **4**: 1-14.
- Rajadhyaksha, M., S. González, et al. (1999). "In Vivo Confocal Scanning Laser Microscopy of Human Skin II: Advances in Instrumentation and Comparison With Histology." *Journal of Investigative Dermatology.* **113**: 293-303.
- Rajadhyaksha, M., M. Grossman, et al. (1995). "In Vivo Confocal Scanning Laser Microscopy of Human Skin: Melanin Provides Strong Contrast." *Journal of Investigative Dermatology.* **104**(6): 946-952.
- Ralston, T. S., D. L. Marks, et al. (2006). "Inverse scattering for optical coherence tomography." *Journal of the Optical Society of America A.* **23**(5): 1027-1037.
- Ralston, T. S., D. L. Marks, et al. (2007). "Interferometric synthetic aperture microscopy." *Nat. Phys.* **3**(2): 129-134.
- Ramanujam, N. (2000). "Fluorescence Spectroscopy of Neoplastic and Non-Neoplastic Tissues." *Neoplasia.* **2**(1/2): 89-117.
- Ren, H., D. Fox, et al. (2006). "Tunable-focus liquid lens controlled using a servo motor." *Optics Express.* **14**(18): 8031-8036.
- Richard, S., B. Querleux, et al. (1993). "Characterization of the Skin In Vivo by High Resolution Magnetic Resonance Imaging: Water Behavior and Age-Related Effects." *Journal of Investigative Dermatology.* **100**(5): 705-709.
- Richards-Kortum, R., R. P. Rava, et al. (1991). "Spectroscopic diagnosis of colonic dysplasia." *Photochem Photobiol.* **53**(6): 777-86.
- Richards-Kortum, R. and E. Sevick-Muraca (1996). "Quantitative Optical Spectroscopy for Tissue Diagnosis." *Annual Reviews in Physical Chemistry.* **47**(1): 555-606.
- Rolland, J. P. (2009). "Gabor Domain Optical Coherence Microscopy." *Submission in Progress.*

- Rolland, J. P., P. Meemon, et al. (2008). Gabor Domain Optical Coherence Microscopy. 1st Canterbury Workshop on Optical Coherence Tomography and Adaptive Optics. A. Podoleanu, Proceedings of SPIE. **7139**: 71390F.
- Rollins, A. M., M. D. Kulkarni, et al. (1998). "In vivo video rate optical coherence tomography." *Optics Express*. **3**(6): 219-229.
- Ruocco, V. and E. Ruocco (1999). "COMMENTARY/MILLENNIUM Tzanck smear, an old test for the new millennium: when and how." *International Journal of Dermatology*. **38**(11): 830.
- Sahin, S., B. Rao, et al. (1997). "Predicting ten-year survival of patients with primary cutaneous melanoma." *Cancer*. **80**(8): 1426-1431.
- Sandby-moller, J. and H. C. Wulf (2004). "Ultrasonographic subepidermal low-echogenic band, dependence of age and body site." *Skin Research and Technology*. **10**(1): 57-63.
- Sato, S. (1979). "Liquid-crystal lens-cells with variable focal length." *Jpn. J. Appl. Phys.* **18**(9): 1679-1684.
- Schmitt, J. M., A. H. Gandjbakhche, et al. (1992). "Use of polarized light to discriminate short-path photons in a multiply scattering medium." *Appl. Opt.* **31**(30): 6535.
- Schmitt, J. M., S. L. Lee, et al. (1997). "An optical coherence microscope with enhanced resolving power in thick tissue." *Optics Communications*. **142**(4-6): 203-207.
- Schmitt, J. M., M. J. Yadlowsky, et al. (1995). "Subsurface imaging of living skin with optical coherence microscopy." *Dermatology*. **191**(2): 93-8.
- Schrader, B. (1995). Infrared and Raman spectroscopy, VCH New York.
- Schrader, B., B. Dippel, et al. (1999). "NIR Raman spectroscopy in medicine and biology: results and aspects." *Journal of Molecular Structure*. **480**: 21-32.
- Schwaighofer, B. W., F. X. J. Fruehwald, et al. (1989). "MRI Evaluation of Pigmented Skin Tumors: Preliminary Study." *Investigative Radiology*. **24**(4): 289.
- Scope, A., C. Benvenuto-Andrade, et al. (2007). "In vivo reflectance confocal microscopy imaging of melanocytic skin lesions: Consensus terminology glossary and illustrative images." *Journal of the American Academy of Dermatology*. **57**(4): 644-658.
- Sherar, M. D., M. B. Noss, et al. (1987). "Ultrasound backscatter microscopy images the internal structure of living tumour spheroids." *Nature*. **330**(3): 493-495.
- Smith, D. A., S. Webster, et al. (1995). "Development of a scanning near-field optical probe for localised Raman spectroscopy." *Ultramicroscopy*. **61**(1): 247-252.

- So, P. T. C., C. Y. Dong, et al. (2000). "Two-photon excitation fluorescence microscopy." *Annual Reviews in Biomedical Engineering*. **2**(1): 399-429.
- Soyer, H. P., J. Smolle, et al. (1987). "Early diagnosis of malignant melanoma by surface microscopy." *Lancet*. **2**(8562): 803.
- Steeg, P. S. (2006). "Tumor metastasis: mechanistic insights and clinical challenges." *Nat Med*. **12**(8): 895-904.
- Sterenborg, H., M. Motamedi, et al. (1994). "In vivo fluorescence spectroscopy and imaging of human skin tumours." *Lasers in Medical Science*. **9**(3): 191-201.
- Stone, N., C. Kendall, et al. (2004). "Raman spectroscopy for identification of epithelial cancers." *Faraday Discussions*. **126**: 141-157.
- Strasswimmer, J., M. C. Pierce, et al. (2004). "Polarization-sensitive optical coherence tomography of invasive basal cell carcinoma." *Journal of Biomedical Optics*. **9**: 292.
- Sudha, G. (2004). "Electronic biopsy for skin cancer detection." *Current Science*. **87**(5): 645-649.
- Svanberg, K., I. Wang, et al. (1998). "Clinical multi-colour fluorescence imaging of malignant tumours--initial experience." *Acta Radiol*. **39**(1): 2-9.
- Takada, K., I. Yokohama, et al. (1987). "New measurement system for fault location in optical waveguide devices based on an interferometric technique." *Appl. Opt*. **26**(9): 1603-1606.
- Tfayli, A., O. Piot, et al. (2005). "Discriminating nevus and melanoma on paraffin-embedded skin biopsies using FTIR microspectroscopy." *BBA-General Subjects*. **1724**(3): 262-269.
- Thompson, K. P. (1980). Aberration fields in tilted and decentered optical systems. College of Optical Sciences. Tucson, University of Arizona. **PhD**: 295.
- Tomatis, S., M. Carrara, et al. (2005). "Automated melanoma detection with a novel multispectral imaging system: results of a prospective study." *Physics in Medicine and Biology*. **50**(8): 1675-1687.
- Tomatis, S., R. Marchesini, et al. (1995). "Reflectance imaging spectroscopy: possible aid in the clinical diagnosis of melanoma." *Proceedings of SPIE*. **2387**: 95.
- Tripp, J. M., A. W. Kopf, et al. (2002). "Management of dysplastic nevi: a survey of fellows of the American Academy of Dermatology." *J Am Acad Dermatol*. **46**(5): 674-82.
- Tseng, S. H., A. Grant, et al. (2008). "In vivo determination of skin near-infrared optical properties using diffuse optical spectroscopy." *Journal of Biomedical Optics*. **13**: 014016.

- Turnbull, D. H., B. G. Starkoski, et al. (1995). "A 40-100 MHz B-scan ultrasound backscatter microscope for skin imaging." *Ultrasound Med Biol.* **21**(1): 79-88.
- Turrell, G. and J. Corset (1996). Raman microscopy: developments and applications, Academic Press, London.
- Van Gemert, M. J. C., S. L. Jacques, et al. (1989). "Skin optics." *Biomedical Engineering, IEEE Transactions on.* **36**(12): 1146-1154.
- Vega-Memije, E., N. M. de Larios, et al. (2000). "Cytodiagnosis of cutaneous basal and squamous cell carcinoma." *International Journal of Dermatology.* **39**(2): 116-120.
- Vereecken, P., M. Laporte, et al. (2005). "Evaluation of extensive initial staging procedure in intermediate/high-risk melanoma patients." *Journal of the European Academy of Dermatology and Venereology.* **19**(1): 66-73.
- Wagnieres, G. A., W. M. Star, et al. (1998). "In Vivo Fluorescence Spectroscopy and Imaging for Oncological Applications." *Photochemistry and Photobiology.* **68**(5): 603-632.
- Wallace, V. P., D. C. Crawford, et al. (2000). "Spectrophotometric assessment of pigmented skin lesions: methods and feature selection for evaluation of diagnostic performance." *Phys. Med. Biol.* **45**(3): 735-751.
- Wang, L. V. and S. L. Jacques (1995). "Noninvasive detection of skin cancers by measuring optical properties of tissues." *Proceedings of SPIE, Lasers in Surgery: Advanced Characterization, Therapeutics, and Systems*
- Wang, L. V. and H. Wu (2007). Biomedical optics: principles and imaging, Wiley-Interscience.
- Wang, R. K. and Z. Ma (2006). "A practical approach to eliminate autocorrelation artefacts for volume-rate spectral domain optical coherence tomography." *Physics in Medicine and Biology.* **51**(12): 3231-3240.
- Welford, W. T. (1974). Thin lens aberrations. Aberrations of the symmetrical optical system. New York, USA, Academic Press: 198-199.
- Welzel, J. (2001). "Optical coherence tomography in dermatology: a review." *Review article.* **7**(1): 1-9.
- Wennberg, A. M., F. Gudmundson, et al. (1999). "In vivo Detection of Basal Cell Carcinoma using Imaging Spectroscopy." *Acta Dermato-Venereologica.* **79**(1): 54-61.
- Westphal, V., A. Rollins, et al. (2002). "Correction of geometric and refractive image distortions in optical coherence tomography applying Fermat's principle." *Optics Express.* **10**(9): 397-404.

- Wiesauer, K., M. Pircher, et al. (2005). "En-face scanning optical coherence tomography with ultra-high resolution for material investigation." *Optics Express*. **13**(3): 1015-1024.
- Wilhelm, K. P. (1997). Bioengineering of the Skin: Skin Surface Imaging and Analysis, CRC Press.
- Willis, R. A. (1952). The Spread of Tumors in the Human Body. London, Butterworth.
- Wong, P. T. T., R. K. Wong, et al. (1991). "Infrared spectroscopy of exfoliated human cervical cells: Evidence of extensive structural changes during carcinogenesis." *Proceedings of the National Academy of Sciences of the United States of America*. **88**(24): 10988-10992.
- Wood, B., S. Zhao, et al. (1988). "High resolution imaging of the skin." *Proceedings of the Society of Magnetic Resonance in Medicine*. **1988**(2).
- Woodward, R. M., B. Cole, et al. (2001). "Terahertz pulse imaging of in-vitro basal cell carcinoma samples." *Lasers and Electro-Optics, 2001. CLEO'01. Technical Digest. Summaries of papers presented at the Conference on*: 329-330.
- Woodward, R. M., B. E. Cole, et al. (2002a). "Terahertz pulse imaging in reflection geometry of human skin cancer and skin tissue." *Physics in Medicine and Biology*. **47**(21): 3853-3863.
- Woodward, R. M., V. P. Wallace, et al. (2002b). "Terahertz pulse imaging in reflection geometry of skin tissue using time-domain analysis techniques." *Proceedings of SPIE*. **4625**: 160.
- Workman Jr, J. J. (1999). "Review of Process and Non-invasive Near-infrared and Infrared Spectroscopy." *Appl. Spectrosc. Rev.* **34**: 1-89.
- Wu, S. T. (2007). Personal Communication. Orlando, FL.
- Xie, T., S. Guo, et al. (2006). "GRIN lens rod based probe for endoscopic spectral domain optical coherence tomography with fast dynamic focus tracking." *Optics Express*. **14**(8): 3238-3246.
- Xu, F., H. E. Pudavar, et al. (1999). "Confocal enhanced optical coherence tomography for nondestructive evaluation of paints and coatings." *Optics Letters*. **24**(24): 1808-1810.
- Xue, P. and J. G. Fujimoto (2008). "Ultrahigh resolution optical coherence tomography with femtosecond Ti: sapphire laser and photonic crystal fiber." *Chinese Science Bulletin*. **53**(13): 1963-1966.
- Ya-Xian, Z., T. Suetake, et al. (1999). "Number of cell layers of the stratum corneum in normal skin-relationship to the anatomical location on the body, age, sex and physical parameters." *Archives of Dermatological Research*. **291**(10): 555-559.
- Ye, M. and S. Sato (2002). "Optical properties of liquid crystal lens of any size." *Jpn. J. Appl. Phys.* **41**.

- Youngquist, R. C., S. Carr, et al. (1987). "Optical coherence-domain reflectometry: a new optical evaluation technique." *Opt. Lett.* **12**(3): 158-160.
- Zemtsov, A., R. Lorig, et al. (1989). "Magnetic resonance imaging of cutaneous melanocytic lesions." *J Dermatol Surg Oncol.* **15**(8): 854-8.
- Zeng, H., H. Lui, et al. (1996). "Optical spectroscopy studies of diseased skin: preliminary results." *Proceedings of SPIE.* **2628**: 277.
- Zeng, H., C. MacAulay, et al. (1995a). "Spectroscopic and microscopic characteristics of human skin autofluorescence emission." *Photochem Photobiol.* **61**(6): 639-45.
- Zeng, H., C. MacAulay, et al. (1995b). "Spectroscopic and microscopic characteristics of human skin autofluorescence emission." *Photochemistry and photobiology.* **61**(6): 639-645.
- Zhang, D. Y. (2003). "Fluidic adaptive lens with high focal length tunability." *Applied Physics Letters.* **82**(19): 3171.
- Zhao, J., H. Lui, et al. (2008). "Integrated real-time Raman system for clinical in vivo skin analysis." *Skin Research and Technology*(0).
- Zipfel, W. R., R. M. Williams, et al. (2003). "Nonlinear magic: multiphoton microscopy in the biosciences." *Nature Biotechnology.* **21**(11): 1369-1377.
- Zonios, G., J. Bykowski, et al. (2001). "Skin Melanin, Hemoglobin, and Light Scattering Properties can be Quantitatively Assessed In Vivo Using Diffuse Reflectance Spectroscopy." *Journal of Investigative Dermatology.* **117**(6): 1452-1457.
- Zonios, G., R. Cothren, et al. (1998). "Spectral Pathology." *Annals of the New York Academy of Sciences.* **838**(1 ADVANCES IN OPTICAL BIOPSY AND OPTICAL MAMMOGRAPHYa): 108-115.
- Zonios, G., L. T. Perelman, et al. (1999). "Diffuse reflectance spectroscopy of human adenomatous colon polyps in vivo." *Appl. Opt.* **38**(31): 6628–6637.